Ørjan Pedersen

One-way wave-equation migration for wide-angle propagation in anisotropic media

Thesis for the degree of Philosophiae Doctor

Trondheim, July 2010

Norwegian University of Science and Technology
Faculty of Engineering Science and Technology
Department of Petroleum Engineering and Applied Geophysics

NTNU
Norwegian University of
Science and Technology

NTNU
Norwegian University of Science and Technology

Thesis for the degree of Philosophiae Doctor

Faculty of Engineering Science and Technology
Department of Petroleum Engineering and Applied Geophysics

ISBN 978-82-471-2246-4(printed ver.)
ISBN 978-82-471-2247-1 (electronic ver.)
ISSN 1503-8181

Doctoral theses at NTNU, 2010:140

Printed by NTNU-trykk

Ørjan Pedersen

One-way wave-equation migration for wide-angle propagation in anisotropic media

PhD thesis

Department of Petroleum Engineering and Applied Geophysics
Norwegian University of Science and Technology
Trondheim
Norway

Summary

Seismic depth migration is a major component in the search for hydrocarbons. As new prospects for oil and gas often are found in areas with challenging subsurface structures, more advanced methods to find and evaluate these prospects are needed. One-way wave-equation migration provides an appealing approach to be used to create an image of the subsurface.

The characteristics of wave propagation can be described through the dispersion relation, relating the vertical and horizontal phase-slowness. In the first part of this thesis, simple and accurate phase-slowness approximations valid for wide-angle propagation in a VTI media are derived.

Information from the subsurface might be increased by recording converted wave reflections in addition to pressure waves. The second part of this thesis provides the development of a set of new one-way propagators for imaging steeply dipping and complex structures using converted and pressure waves in a VTI medium.

Reliable amplitude information from one-way methods is useful as hydrocarbon indicators in structural imaging and for migration velocity analysis. In the third part of this thesis, a flux-normalized wavefield decomposition is used as a starting point to develop one-way propagators with improved amplitudes.

In new exploration areas, salt structures are important examples of subsurface complexity. This poses a challenge for one-way migration methods due to large velocity contrasts between salt and the surrounding sediments. A novel approach using one-way migration operators combined with a lateral windowing construction to limit the impact of errors introduced by large velocity contrasts is developed.

Preface

This thesis is submitted in partial fulfillment of the requirements for the degree *philosophiae doctor* (PhD) at the Norwegian University of Science and Technology (NTNU). Professor Bjørn Ursin at the Department of Petroleum and Applied Geophysics, NTNU, has been supervisor.

The research was funded by the Research Council of Norway (NFR) and the Rock Seismic research project (ROSE). The ROSE consortium is based at NTNU with funding from NFR and 23 industry sponsors. The research in ROSE is focused on rock physics and rock mechanics; geophysical reservoir characterization and time-lapse seismic; and seismic imaging and inversion. The thesis work has been carried out at the Department of Petroleum Engineering and Applied Geophysics, NTNU.

Acknowledgements

The advisor through my PhD studies has been professor Bjørn Ursin. I would like to thank him for supervising and encouraging me on this project. His experience and extensive knowledge has been a great inspiration. I thank Alexey Stovas (NTNU) for useful advice during the work of the article in chapter 2. I would like to thank Robert Ferguson (CREWES) for many interesting discussions. A special thank to Sverre Brandsbergh-Dahl (formerly BP America) for inviting me to do an internship with the advanced imaging group in BP, Houston.

Most of my work on this project was carried out at the Department of Petroleum Engineering and Applied Geophysics (IPT). I would like to thank my friends and colleagues at the department for creating a good place to work. In particular, I would like to thank Tor Erik Rabben for help and discussions regarding LaTeX, Matlab, HPC programming and geophysics in general, Thomas Røste for many interesting discussions, Sverre Johnsen, Kenneth Duffaut, Milana Aizenberg, Andreas Evensen, Steinar Nag, Janniche Nordskag, Olve Rasmussen, and Christian Crescente. The final stage of this work was carried out at the Statoil research center in Trondheim. I would like to thank my colleagues for help and advice, in particular Hans-Kristian Helgesen, Are Osen, Stig-Kyrre Foss, Olav Kvamme Leirfall, Ketil Hokstad, Andrew Carter, Børge Arntsen, and Tage Røsten.

I want to thank my parents for all support and encouragement through many years of study. Finally, a special thank to my close friend and partner, Mette Jung Borgersen, for motivation and reminding me that there are other things in life besides work.

Trondheim, July 2010

Ørjan Pedersen

Contents

Summary **III**

Preface **V**

Acknowledgements **VII**

1 Thesis introduction **1**
1.1 Motivation 1
1.1.1 Marine seismic acquisition 2
1.1.2 Seismic imaging and velocity analysis 5
1.2 One-way wave-equation migration for wide-angle propagation in anisotropic media 8
1.2.1 Thesis content 9

2 Wide-angle phase-slowness approximations in VTI media **11**
2.1 Introduction 12
2.2 Taylor-series representations 13
2.3 Continued-fraction approximations 15
2.4 Wide-angle approximations 17
2.5 Converted waves 19
2.6 Discussion 20
2.7 Numerical results 21
2.8 Conclusions 28
2.9 Acknowledgments 29
2.A Horizontal on-axis shear-wave triplication 29

3 One-way wave-equation migration of compressional and converted waves in a VTI medium **35**
3.1 Introduction 36

3.2 Theory . . . 38
3.3 Slowness expressions for qP- and qSV-waves . . . 41
3.4 Simplified slowness expressions for qP-waves . . . 43
3.5 Accuracy of slowness expressions . . . 44
3.6 One-way propagators . . . 48
3.7 Numerical results . . . 49
3.7.1 Impulse responses . . . 49
3.7.2 2D Synthetic data example . . . 52
3.8 3D Real ocean-bottom data example . . . 52
3.9 Conclusions . . . 58
3.10 Acknowledgments . . . 65
3.A Finite-difference corrections for one-way thin-slab propagators . . . 65

4 Flux-normalized wavefield decomposition and migration of marine seismic data 69
4.1 Introduction . . . 70
4.2 Laterally homogeneous medium . . . 71
4.2.1 Amplitude-normalized wavefields . . . 73
4.2.2 Flux-normalized wavefields . . . 74
4.3 One-way wave-equations . . . 76
4.4 Imaging conditions . . . 77
4.5 Heterogeneous medium . . . 80
4.6 Numerical results . . . 82
4.6.1 Imaging in a lateral invariant medium . . . 83
4.6.2 Marine field seismic data example . . . 86
4.7 Conclusions . . . 90
4.8 Acknowledgments . . . 90
4.A The wave-equation angle transforms . . . 90
4.B Approximate transmission and reflection coefficients . . . 96

5 Seismic imaging using lateral adaptive windows 99
5.1 Introduction . . . 99
5.2 One-way wavefield extrapolation . . . 102
5.3 Lateral adaptive windows . . . 103
5.3.1 Velocity treatment . . . 105
5.4 Numerical results . . . 106
5.4.1 Model of vertical interface . . . 106
5.4.2 Imaging the 2D SEG/EAGE A-A' salt model . . . 110
5.4.3 Field data example . . . 112

5.5 Discussion 113
5.6 Conclusions 115
5.7 Acknowledgments 115

References **119**

A Improved wide-angle phase-slowness approximations **131**
A.1 Improved approximations 131
A.2 Numerical example 132

Chapter 1

Thesis introduction

This chapter contains a motivation for this thesis and a brief introduction to the field of seismic imaging. The introduction is not a complete review of the literature on the subject, but gives basic information to the readers not familiar with the subject of seismic imaging. I focus in particular on seismic acquisition and seismic migration. In section 1.2.1, an overview of the individual chapters contained in this thesis is provided.

1.1 Motivation

The increasing demand for oil and gas drives the need for exploration in new areas and for increased recovery in producing fields. New fields are often found in challenging marine areas with complex subsurface structures, such as the Gulf of Mexico, the West-coast of Africa or the Norwegian Sea. Exploration in complex geological areas requires more advanced methods to find and appraise hydrocarbon prospects. As a consequence, this encourages continual research and development of new methods and improvement of existing methods for analyzing the subsurface.

Currently, seismic surveying is the most common method for obtaining information about the subsurface. The objective of seismic surveying is to attain information on subsurface structures and properties for prediction of hydrocarbon prospectivity. This is accomplished by appropriate acquisition of seismic data; velocity analysis and seismic imaging; and finally interpretation.

Alternative methods like electro-magnetic surveying (Ward, 1980) and gravimetric and magnetic measurements (Johnson, 1998) are becoming more widely used. However, these methods are usually used to provide complimentary

constraints on reservoir geometry and characteristics obtained by seismic in combined interpretation in order to reduce risk and optimize recovery of a prospect (Foss et al., 2008; Ellingsrud et al., 2002).

A seismic experiment involves directing an energy source that generates *a seismic wave* which propagates into the Earth's subsurface. A seismic wave can be regarded as a subsurface disturbance, where the properties of the wave propagation are governed by the elastic stiffness and density of the medium. Seismic surveying consists of several seismic experiments.

Applying stress on a medium generates changes in both shape and dimension. A medium with the ability to resist and recover from deformations is referred to as an elastic medium. Force acting upon an elastic medium induces a force which tries to restore the state of equilibrium. This property causes waves to propagate through the medium, depending on its state (Betti, 2007). In a solid medium, both compressional and shear forces propagate, while in ideal liquid and gasses, only compressional forces travel (Wapenaar and Berkhout, 1989).

In general, the physical properties of a rock may vary in the direction which they are measured. This is commonly referred to as anisotropy (Sheriff, 2002), and is often observed in seismic surveying. There are numerous causes of anisotropy (Jones, 2010). There are a number of classes of anisotropy. It is common in seismic surveying to approximate the anisotropy of the Earth by transverse isotropy, which has an axis of cylindrical symmetry. The axis of symmetry can either be vertical or tilted in any direction. For a transverse isotropic medium, the physical properties only depend on the angle between the axis of symmetry and the direction of the measurement. Accounting for anisotropy is important for accurate wave propagation (Larner and Cohen, 1993; Audebert et al., 2006).

1.1.1 Marine seismic acquisition

In marine seismic, the energy source is typically placed in the water, thus the generated wave is a pressure wave (P-wave) since fluids do not support shear waves (S-waves). The wave propagates downward into the subsurface until reaching an interface in the subsurface. These interfaces usually represent boundaries between different geological structures. At such an interface in the subsurface, an incoming P-wave is split into reflected and transmitted P- and S-waves as illustrated in Figure 1.1. The reflected wave will propagate up towards the surface, while the transmitted wave will propagate further down into the subsurface where again reflection and transmission may occur. The partitioning into reflected, transmitted and converted waves is dependent on the earth properties at the interface.

The reflected energy is subsequently recorded; where the amplitude and

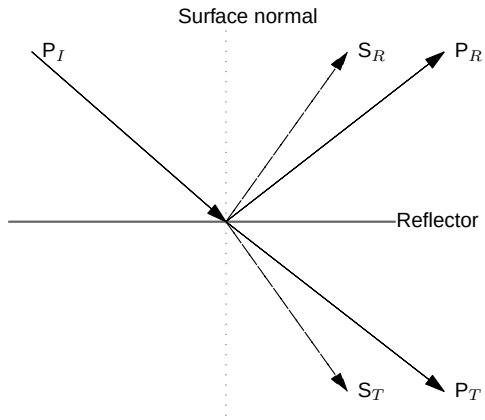

Figure 1.1: An incoming P-wave P_I is reflected as a P-wave P_R and an S-wave S_R; and transmitted as a P-wave P_T and an S-wave S_T .

traveltime of reflected energy is measured. These measurements contain information on the subsurface structures which has been illuminated by the seismic experiment, that is, the part of the subsurface that the measured seismic wave has travelled through.

There are several ways to acquire seismic data. In a marine environment, the most common ways to acquire seismic data are either *towed streamer* or *ocean bottom seismic*. Field data examples in this thesis are either acquired by towed streamer or ocean bottom seismic.

In marine towed streamer acquisition, both the seismic source and hydrophones are deployed in the water a few meters below the sea surface as illustrated in Figure 1.2(a). As a consequence, measurements are P-waves only, and acoustic wave theory is considered a valid assumption. The hydrophones are towed behind a seismic vessel, either along one single line as in two-dimensional (2D) seismic surveying or in densely distributed lines as in three-dimensional (3D) seismic surveying. A wide variety of acquisition configurations are developed in order to increase subsurface illumination to improve data quality (Long, 2010).

In ocean bottom seismic (OBS) acquisition, the seismic source is deployed in the water, while the receivers are placed on the sea floor. See Figure 1.2(b) for a schematic representation of an OBS survey configuration. Each receiver can consist of a four-component measurement (4C) with a hydrophone and a three-component geophone. To record an S-wave, one need to measure at a solid. Since the receivers in an OBS survey are at the sea floor, this allows measurement of both reflected P-wave and reflected S-wave energy. An OBS acquisition is usually more

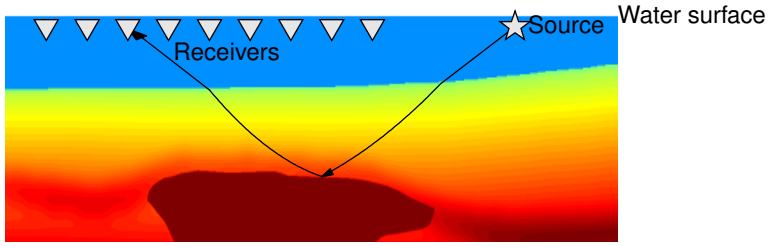

(a) A towed streamer survey.

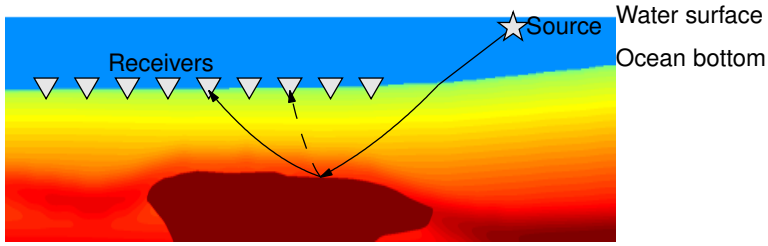

(b) An OBS survey.

Figure 1.2: Schematic representation of (a) a towed streamer and (b) an OBS survey. The solid line represents P-wave mode and the dashed line represents S-wave mode. The colored structures represents a subsurface velocity model. The reflection in this illustration is caused by a salt structure with higher velocity than the surrounding sediments.

costly than towed streamer acquisition due to more challenging operations and time consumption. The increased cost can sometimes be justified by the additional information obtained compared to towed streamer acquisition (Granli et al., 1999). In addition, an OBS survey can provide the benefit of better illumination of the subsurface compared to towed streamer acquisition.

After the data acquisition step, the data is enhanced by removing noise related to the physical acquisition and source signature. Further processing steps often assume that the seismic data contain primary reflections (waves reflected once) only. In addition to primary reflections the recorded seismic data contain *multiples*. Multiples are seismic waves reverberated in the water or between subsurface reflectors (Ikelle and Amundsen, 2005). Multiples originating from subsurface reflectors are normally assumed to be weak while water-layer related multiples can be removed by techniques that predict and subtract the multiples from the data (Abma et al., 2005).

1.1.2 Seismic imaging and velocity analysis

Seismic migration can be regarded as a process where recorded primary reflections are moved to their true position, thus creating a seismic image of the subsurface. Seismic imaging is a crucial component for understanding underground geological structures in the search for hydrocarbons and in reservoir monitoring. Providing accurate subsurface images, help in minimizing risk in exploration and aids in optimizing production of existing fields.

Seismic migration involves propagating wavefields into a representation of the subsurface, where an image is formed. Wavefield propagation requires an estimate of the velocities in the subsurface, and this estimation is essential in order to create an accurate image of the subsurface. Various methods for estimating velocities exist, and in the literature they are usually divided into two strategies depending on the space the strategy works, either in the data space (before migration) or in the image space (after migration). In the data space, modelled data using an initial guess of the velocities are matched to the measured data and used to improve the initial guess, see e.g. Bishop et al. (1985); Pratt (1999); Lambaré (2008). In the image space, utilizing characteristics of migrated images revealing an erroneous model with an initial guess of the velocities provide information for model improvements, see e.g. Sava and Biondi (2004); Shen and Symes (2008).

There are several methods developed to perform seismic migration. These are usually categorized as either *time-* or *depth-migration*. Time migration (Larner et al., 1981) is a technique suitable for areas for which one can assume no, or very small, variation in velocity in the lateral direction (Whitmore et al., 1987). The result from time migration is an image not in depth, but in traveltime; however, it can be converted to depth usually by a time-to-depth stretch. Depth migration is currently the preferred technique. It creates images in physical coordinates, and is suitable in areas where local velocity variations in the lateral direction exist.

Depth migration is usually classified as either *ray methods* or *wave-equation methods*, each class with their own strengths and weaknesses. See e.g. Etgen et al. (2009) for a thorough overview. Ray methods depend on an asymptotic high-frequency approximation of the wave-equation while wave-equation methods solve the wave-equation for a wide range of frequencies. The most common ray-methods are Kirchhoff (Schneider, 1978; Beylkin, 1985) or the more recent beam migration methods (Sun et al., 2000; Hill, 2001). Ray methods are considered to be computational cheap, but not always suitable for imaging complex structures. For example, multipathing due to complex velocity may result in images of the subsurface that are not reliable using ray-methods (Biondi, 2006). Multipathing is handled naturally in wave-equation methods. The frequency content in seismic

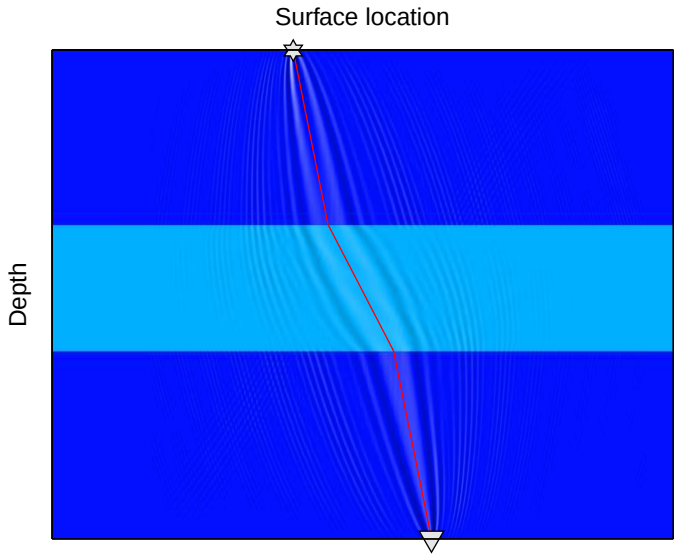

Figure 1.3: Wavepath (in gray-scale) and raypath (in red) between a source at the surface (star) and a point in the subsurface (triangle) in a layered model (blue). The wavepath represent 14 Hz and the raypath represent the high frequency approximation.

data is band-limited. The portion of the subsurface in which a wave travel from a source position to a location in the subsurface is frequency dependent; thus, realistic wavepaths are inadequately estimated by the ray approximation. This is illustrated in Figure 1.3 with a simple example of a layered subsurface providing a comparison of a wavepath and the corresponding raypath.

Wave-equation methods are divided into either *one-way* or *two-way* methods. The most common two-way migration method is *reverse time migration* (RTM) (Whitmore, 1983; Levin, 1984) which directly solves the wave-equation, usually with a finite-difference scheme. RTM is considered to be very accurate, but challenging noise suppression when creating an image and expensive computational implementations, can limit its application in 3D imaging in particular.

There exists a wide variety of one-way migration methods. They build on the solution of an approximation to the wave-equation, the so-called one-way wave-equation. This approach assumes that waves only travel downward from the source and upward from the reflectors. This is in general not physically correct since both wavefields can travel both upward and downward. The one-way approach

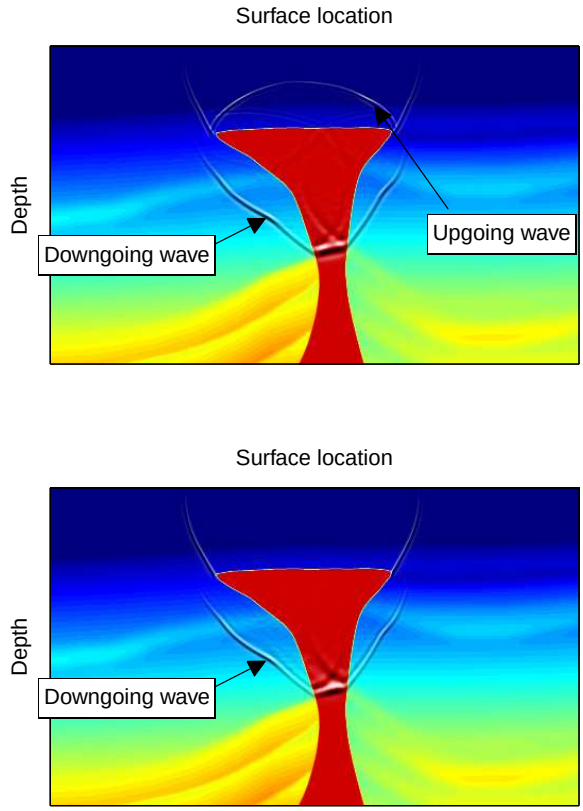

Figure 1.4: Snapshot in time of a downgoing source wavefield in a synthetic model at 2 seconds. The wave-propagation is modelled with a two-way (top) and a one-way (bottom) method. The two-way method allows for the wavefield to be reflected upward while the one-way method does not. The two-way method is a finite-difference scheme, and the one-way method is described in chapter 5.

breaks down for horizontally traveling waves. In addition, smooth lateral velocity variations are assumed and most methods are only kinematically correct. However, a large amount of research is devoted to advancing on drawbacks of one-way methods (Hale et al., 1992; Zhang et al., 2003; Shan and Biondi, 2008).

The solution of the one-way wave-equation is expensive to implement, but efficient and robust approximations make one-way methods computationally cheap, which make them an attractive alternative for 3D depth imaging. In complex areas where multipathing occurs, one-way methods are considered to render images superior to ray-based methods (Operto et al., 2000).

Most one-way methods operate in the frequency domain, where each frequency slice is downward continued within thin depth-slabs in a recursive fashion. One-way methods can be classified into the domain in which they operate. In the space-domain, there are for example implicit methods (Claerbout, 1970) and explicit methods (Holberg, 1988), and in the wavenumber domain, the phase-shift method (Gazdag, 1978). In the mixed space-wavenumber domain, the most well-known methods are phase-shift plus interpolation (Gazdag and Sguazzero, 1984); split-step (Stoffa et al., 1990); extended split-step (Kessinger, 1992); Fourier finite-difference (FFD) (Ristow and Rühl, 1994); and generalized-screen (Wu and Huang, 1992; Rousseau and de Hoop, 2001b).

Figure 1.4 illustrates an example where two-way methods allow for the wavefield to be reflected upward, while the one-way does not. The two-way method describes the physical wave-propagation with reflected and transmitted waves. The one-way method is an approximation to the physical wave-propagation and only describes the downgoing part of the wavefield.

The models used in constructing Figures 1.2(a); 1.2(b); and 1.4 were created by Hemang Shah and are provided courtesy of BP Exploration Operation Company Limited (”BP”).

1.2 One-way wave-equation migration for wide-angle propagation in anisotropic media

There are many options when deciding on which imaging method one should use to create a trustworthy image of the subsurface. One-way methods offer an efficient and robust alternative to two-way methods and a more accurate alternative than ray-based methods when encountering strong velocity contrasts and complex subsurface regions.

There are some challenges for existing one-way methods. These are related to the ability of one-way methods to predict both the kinematics and dynamics in

wave-propagation. A considerable amount of research in the field of geophysics over the previous decades has been dedicated to improve on these challenges.

The main objective of this thesis work is to develop new, and improve on existing, imaging techniques used in one-way wave-equation migration of seismic data. This will enable the possibility to handle more complex subsurfaces and more realistic representations of the subsurface, and hence aid in mitigating risk in hydrocarbon prospect evaluation. Each paper in this thesis contains individual introductions describing its contribution in view of existing methods.

1.2.1 Thesis content

This thesis consists of five chapters including this introduction and an additional appendix. Chapters 2 through 5 can be considered as independent papers with their own abstracts; motivations; introductions; conclusions; and appendixes. Therefore, some of the introductory and background material presented in the different chapters may coincide. In some chapters, additional figures supporting the numerical examples are included compared to the published papers.

The content of the remaining chapters is outlined in the list below:

Chapter 2: An approach for deriving phase-slowness approximations accurate for wide-angles in a VTI medium is introduced. The approach is based upon requiring that the approximated slowness expressions are exact both at the vertical and the horizontal direction, and these approximations are found using Taylor and continued-fraction approximations. The derived approximations can be utilized in phase-shift migration methods and our numerical tests show that these approximations are more accurate for wide-angles than existing approximations. The co-authors of this work are Bjørn Ursin and Alexey Stovas. This work has been presented at the 68th EAGE Conference and Exhibition in Vienna (2006) and at the ROSE meeting in Trondheim in 2005. The paper is published in Geophysics in 2007, volume **72**, pages S177-S185 (Pedersen et al., 2007).

Chapter 3: New one-way wave-equation propagators for compressional and converted waves in a VTI medium are obtained. The propagators are based upon a Fourier finite-difference scheme and new approximations to the vertical slowness as a function of horizontal slowness. Numerical tests show that the derived propagators are valid for wide-angle propagation both for compressional and converted waves in the presence of anisotropy and large velocity contrasts. A three-dimensional field data example from the Volve

field in the Central North Sea shows that the method is applicable to real data. The co-authors of this work are Hans-Kristian Helgesen and Bjørn Ursin. This work has been presented at the ROSE meeting in Trondheim in 2010. The paper is accepted for publication in Geophysics.

Chapter 4: In this chapter, wavefield decomposition and one-way wave-equation propagators for flux-normalized wavefield extrapolation are developed. An unbiased estimate of the reflectivity using the wave-equation angle-transform is formulated. The numerical test shows that the method provides accurate amplitude information for a one-dimensional medium. A comparison to conventional wavefield decompositions using field data from the Nordkapp Basin indicates that using the flux-normalized approach improves amplitude information in laterally invariant media. The co-authors of this work are Bjørn Ursin and Børge Arntsen. This work was partially presented at the ROSE meeting in Trondheim in 2007, and is under preparation for submission to Geophysics.

Chapter 5: In this chapter, a novel method for subsalt imaging using one-way wave-equation extrapolators is presented. The challenge of large velocity contrasts associated with salt provinces in wavefield downward continuation methods is addressed by an adaptive construction of lateral windows. These windows contain salt, sediments or the salt-sediment boundary, and by propagating the wavefield within these windows we limit the impact of the errors associated with large velocity contrasts on the global wavefield. The performance of the method is demonstrated on both synthetic data and a field data example from the South Atlantic. The co-authors of this work are Sverre Brandsbergh-Dahl and Bjørn Ursin. This work has been presented at the 69th EAGE Conference and Exhibition in London (2007) and is published in Geophysics in 2010, volume **75**, pages S73-S79 (Pedersen et al., 2010).

Appendix A: A discussion on improved approximations and implementation of the derived wide-angle phase-slowness approximations presented in chapter 2 is included in Appendix A. The content is published in Geophysics in 2008, volume **73**, pages X1-X2 (Pedersen, 2008).

Chapter 2

Wide-angle phase-slowness approximations in VTI media

Ø. Pedersen[1], B. Ursin[1], A. Stovas[1]

[1] *Department of Petroleum Engineering and Applied Geophysics, NTNU*

Abstract

An anisotropic medium with vertical symmetry axis (VTI) often presents a good model for describing of real rocks. Propagation of quasi-P and quasi-SV-waves in such media requires an expression of the vertical phase slowness, which is a complicated function of the horizontal phase slowness and the medium parameters. For converted-wave phase-shift migration methods, it is desired to have slowness expressions that are simple and accurate at wide angles of propagation. Taylor-series representations of the squared vertical slowness for quasi-P and quasi-SV-waves result in new wide-angle phase-slowness approximations based on truncated series and continued-fraction representations. Slowness approximations that are exact for both vertical propagation and at a horizontal slowness corresponding to horizontally traveling qP waves are derived. The approximation for quasi-SV-waves can be used in phase-shift migration in media where the quasi-SV wavefront contains triplications. These approximations are tested on several models and compared to previously published approximations. The numerical tests suggest that the new continued-fraction approximations are more accurate. They can be used in phase-shift migration algorithms which are more efficient for large angles than the existing approximations.

2.1 Introduction

Phase-shift migration methods are used often in subsurface imaging. The seismic wave-field is extrapolated by applying a phase shift in the frequency-wavenumber domain. The phase-shift operator depends on the frequency and the vertical phase-slowness component of the wavefield (Gazdag, 1978). The vertical slowness generally can be represented as a complicated function of horizontal slowness. Schoenberg and de Hoop (2000) state that, for migration, "it is useful to have an algorithm that is simple (i.e., with the root structure of an isotropic medium) and accurate to compute the vertical slowness as a function of horizontal slowness."

We consider wave propagation in a transversely isotropic medium with a vertical symmetry axis (VTI medium). For quasi-P (qP) and quasi-SV (qSV) waves, the medium is characterized by four Thomsen (1986) parameters, where the dispersion relations for the qP- and qSV-waves (Aki and Richards, 1980) express squared vertical slowness as a function of horizontal slowness. These expressions contain a square root that we avoid by replacing it with a rational approximation.

Fowler (2003) presents an overview over various dispersion-relation approximations in VTI media. His overview includes three-parameter dispersion relation approximations from Alkhalifah (1998, 2000a), Stopin (2000), Dellinger et al. (1993), Harlan (1995), and Tsvankin and Thomsen (1994). Han and Wu (2005) use the dispersion relation approximation from Alkhalifah (1998, equation 5) to develop a one-way screen propagator for qP-waves in VTI media. Farra (2001) obtains explicit analytic formulas of approximate square phase velocities for VTI symmetries. Approximate dispersion relations in VTI media are also discussed in Schoenberg and de Hoop (2000), with rational approximations for squared slowness functions. They also give a wide-angle approximation of the squared qP slowness that is exact for vertically and horizontally traveling waves.

Here, we derive several approximations for the qP and qSV squared slowness which are more accurate for wide angles than the existing approximations, with Taylor-series representations of the exact expressions as a starting point. For approximations valid for wide angles, the Taylor-series representations are manipulated algebraically to ensure they are exact for both vertical and horizontal propagation. All of these Taylor series are used to derive continued-fraction approximations by matching the coefficients in the power series. Simplified three-parameter expressions for qP-waves are found using the quasi-acoustic (Alkhalifah, 1998; Fowler, 2003) approximation. For qSV-waves, simplified expressions are found by eliminating anisotropy parameters of orders higher than

one or using the close relation between the exact qP and qSV phase-slowness expressions.

For the migration of $qP - qSV$ reflected waves (C-waves), the horizontal slowness must be less than the slowness for horizontally traveling qP-waves to avoid evanescent waves. For this case we develop new approximations for the vertical slowness of qSV-waves that are exact for both a horizontal slowness of zero (i.e., vertical propagation) and a horizontal slowness corresponding to horizontally traveling qP-waves.

For qSV-waves, there may exist triplications in the group velocity function. (Musgrave, 1970; Thomsen and Dellinger, 2003; Tygel et al., 2007). For a horizontal on-axis triplication, the vertical slowness is a multivalued function of horizontal slowness, as discussed in Appendix 2.A. In that case, these approximations cannot be used. However, the approximation for qSV slowness proposed for C-waves may still be used because it is intended for horizontal slownesses of less than the values for which a horizontal on-axis triplication occurs. We compare the accuracy of the various approximations for five different VTI media.

2.2 Taylor-series representations

Let ρ denote the density and let c_{ij} denote the stiffness coefficients of the medium. Then the vertical qP phase velocity is given by

$$\alpha_0 = \sqrt{\frac{c_{33}}{\rho}}, \tag{2.1}$$

and the vertical qSV phase velocity is given by

$$\beta_0 = \sqrt{\frac{c_{44}}{\rho}}. \tag{2.2}$$

Further, the Thomsen (1986) parameters ε and δ are defined in terms of the stiffness coefficients by

$$\varepsilon = \frac{c_{11} - c_{33}}{2c_{33}}, \tag{2.3}$$

and

$$\delta = \frac{(c_{13} + c_{44})^2 - (c_{33} - c_{44})^2}{2c_{44}\,(c_{33} - c_{44})}. \tag{2.4}$$

In our derivations, it will be convenient to use the parameters

$$\zeta \;=\; \varepsilon - \delta, \tag{2.5}$$

and

$$\sigma = \gamma_0^2 \zeta \tag{2.6}$$

$$= \left(\frac{\alpha_0}{\beta_0}\right)^2 (\varepsilon - \delta)\,, \tag{2.7}$$

where γ_0 denotes the ratio between the vertical qP and the vertical qSV velocities. The parameter σ was introduced by Tsvankin and Thomsen (1994) and the parameter ζ is similar to $\eta = (\varepsilon - \delta)/(1 + 2\delta)$ (Alkhalifah, 1998) in the sense that $\zeta \approx \eta$ when $\delta \ll 1/2$.

The dispersion relation relates the vertical and the horizontal slowness. This relation can be expressed in terms of the Thomsen parameters ε and δ as well as the vertical qP and the vertical qSV phase velocities. It can be solved for the squared vertical slowness q^2 as a function of the horizontal slowness p, both for the qP- and qSV-wave modes. To get the vertical wavenumber k_z, the vertical slowness q can be written as

$$q = k_z/\omega, \tag{2.8}$$

and the horizontal slowness p can be written

$$p = k_x/\omega. \tag{2.9}$$

Let

$$\begin{aligned} q_{\alpha_0}^2 &= \frac{1}{\alpha_0^2} - p^2, \\ q_{\beta_0}^2 &= \frac{1}{\beta_0^2} - p^2, \end{aligned} \tag{2.10}$$

where p denotes the horizontal slowness. From the dispersion relation, the squared vertical slowness for qP- and qSV-waves in a VTI medium can be expressed by (Stovas and Ursin, 2003; Ursin and Stovas, 2006)

$$q_{\alpha,\beta}^2 = \frac{1}{2}\Bigg[q_{\alpha_0}^2 + q_{\beta_0}^2 - 2p^2\,(\sigma + \delta) \mp \sqrt{\left(q_{\beta_0}^2 - q_{\alpha_0}^2\right)^2 - 4\frac{p^2}{\alpha_0^2}\left(\gamma_0^2 - 1\right)(\sigma - \delta) + 4p^4\left(2\frac{(\gamma_0^2 - 1)}{\gamma_0^2}\sigma + (\sigma + \delta)^2\right)}\Bigg]. \tag{2.11}$$

If there is no horizontal on-axis shear-wave triplication, the negative sign in front of the radical corresponds to the qP slowness and the positive sign corresponds to the qSV slowness. In case of a horizontal on-axis shear-wave triplication, q_β is multivalued for some values of p. (See Appendix 2.A.)

Expanding the square root in equation 2.11 in a Taylor series, the squared slowness for qP-waves is

$$q_\alpha^2 = \frac{1}{\alpha_0^2}\left(1 - \sum_{j=0}^{\infty} a_j \left(p\alpha_0\right)^{2j+2}\right), \tag{2.12}$$

with

$$\begin{aligned} a_0 &= 1 + 2\delta, \\ a_1 &= \frac{2\sigma}{\gamma_0^2}\left(1 + \frac{2\gamma_0^2\delta}{\gamma_0^2 - 1}\right), \\ a_2 &= \frac{-4\sigma}{\gamma_0^2\left(\gamma_0^2 - 1\right)}\left(\delta - \sigma\right)\left(1 + \frac{2\gamma_0^2\delta}{\gamma_0^2 - 1}\right). \end{aligned} \tag{2.13}$$

Higher-order coefficients of the square root expansion are given in Ursin and Stovas (2006, equation B-9). From the exact expressions of q_α^2 and q_β^2 in equation 2.11, we get the relation

$$q_\alpha^2 + q_\beta^2 = q_{\alpha_0}^2 + q_{\beta_0}^2 - 2p^2\left(\sigma + \delta\right). \tag{2.14}$$

Using equation 2.12 in 2.14 we find that the squared slowness for qSV-waves can be represented by

$$q_\beta^2 = \frac{1}{\beta_0^2}\left(1 - \sum_{j=0}^{\infty} c_j \left(p\beta_0\right)^{2j+2}\right), \tag{2.15}$$

where

$$\begin{aligned} c_0 &= 1 + 2\sigma, \\ c_j &= -a_j\gamma_0^{2j}, \qquad j = 1, 2, \ldots. \end{aligned} \tag{2.16}$$

2.3 Continued-fraction approximations

A continued-fraction approximation (see, e.g., pp. 163-167 of Press et al. (1992)) of the vertical squared qP slowness in equation 2.12, which matches the Taylor

approximation up to $(p\alpha_0)^6$, is

$$q_\alpha^2 = \frac{1}{\alpha_0^2}\left(1 - a_0\left(p\alpha_0\right)^2 - \frac{a_1\left(p\alpha_0\right)^4}{1-\left(a_2/a_1\right)\left(p\alpha_0\right)^2}\right), \tag{2.17}$$

where the coefficients a_j are given in equations 2.13 and where

$$\frac{a_2}{a_1} \;=\; \frac{-2\left(\delta-\sigma\right)}{\gamma_0^2-1}. \tag{2.18}$$

In the quasi-acoustic approximation (Alkhalifah, 1998), we assume $\gamma_0^2 \gg 1$, and simplify the coefficient a_1 and the ratio between the coefficients a_2 and a_1 to respectively, $a_1 \approx 2\zeta\left(1+2\delta\right)$ and $a_2/a_1 \approx 2\zeta$. Substituting these simplified coefficients into equation 2.17 yields a simplified continued-fraction approximation for the squared qP slowness, given by

$$q_\alpha^2 = \frac{1}{\alpha_0^2}\left(\frac{1-\left(1+2\varepsilon\right)\left(p\alpha_0\right)^2}{1-2\zeta\left(p\alpha_0\right)^2}\right). \tag{2.19}$$

This expression is equivalent to the dispersion-relation approximation from Alkhalifah (1998), his equation 5. For horizontally traveling waves we have $q_\alpha = 0$ and $p^2 = \alpha_h^{-2}$, where

$$\alpha_h = \alpha_0\sqrt{1+2\varepsilon}. \tag{2.20}$$

Thus the simplified qP continued-fraction approximation of the squared qP slowness in equation 2.19 is exact for both horizontally and vertically traveling waves.

By a similar approach, a continued-fraction approximation of the qSV squared slowness given in equation 2.15, matching the Taylor approximation up to $(p\beta_0)^6$, results in

$$q_\beta^2 = \frac{1}{\beta_0^2}\left(1 - c_0\left(p\beta_0\right)^2 - \frac{c_1\left(p\beta_0\right)^4}{1-\left(c_2/c_1\right)\left(p\beta_0\right)^2}\right) \tag{2.21}$$

where the coefficients c_j are given in equation 2.16 and

$$\frac{c_2}{c_1} \;=\; \frac{a_2}{a_1}\gamma_0^2. \tag{2.22}$$

We approximate the coefficient $c_1 = -a_1\gamma_0^2$ and c_2/c_1, using the same approximations we used for a_1 and a_2/a_1, and ignore products of anisotropy

parameters. Inserting the simplified coefficients into equation 2.21, we obtain a simplified continued-fraction approximation for the qSV squared slowness given by

$$q_\beta^2 = \frac{1}{\beta_0^2}\left(1 - (1+2\sigma)\,(p\beta_0)^2 + \frac{2\sigma\,(p\beta_0)^4}{1-2\sigma\,(p\beta_0)^2}\right). \tag{2.23}$$

Just like the Taylor series approximations, the continued-fraction approximations in equations 2.17 and 2.21 depend on all four parameters α_0, β_0, ε and δ. The simplified expression for qP waves in equation 2.19, however, depends on only three parameters, α_0, ε and ζ, while the simplified expression for qSV-waves in equation 2.23 depends on only two parameters, β_0 and σ.

2.4 Wide-angle approximations

The next approximations of the squared vertical-slowness expressions are exact in both vertical and horizontal direction of propagation. We denote these approximations as the wide-angle approximations. They are found using the fact that when $p^2 = 1/v_h^2$, the vertical slowness is zero, where v_h is the horizontal phase velocity, for each wave mode. For qP-waves, we factor a term $(1-(\alpha_h/\alpha_0)^2(p\alpha_0)^2)$ from the Taylor approximation in equation 2.12 and subsequently find the corresponding continued-fraction approximation accurate up to order $(p\alpha_0)^6$. Factoring this term yields the following representation of the squared vertical qP slowness:

$$q_\alpha^2 = \frac{1}{\alpha_0^2}\left(1 - \left(\frac{\alpha_h}{\alpha_0}\right)^2 (p\alpha_0)^2\right)\left(1 - \sum_{j=0}^{\infty} b_j\,(p\alpha_0)^{2j+2}\right), \tag{2.24}$$

where

$$\begin{aligned} b_0 &= a_0 - \left(\frac{\alpha_h}{\alpha_0}\right)^2 = -2\zeta, \\ b_j &= a_j + \left(\frac{\alpha_h}{\alpha_0}\right)^2 b_{j-1}, \qquad j = 1,2,\ldots \end{aligned} \tag{2.25}$$

(Cf. equation 27 of Schoenberg and de Hoop (2000).) A continued-fraction approximation of the wide-angle squared slowness representation in equation 2.24

is given by

$$q_\alpha^2 = \frac{1}{\alpha_0^2}\left(1-\left(\frac{\alpha_h}{\alpha_0}\right)^2(p\alpha_0)^2\right)\left(1-b_0\,(p\alpha_0)^2-\frac{b_1\,(p\alpha_0)^4}{1-(b_2/b_1)\,(p\alpha_0)^2}\right). \tag{2.26}$$

where the coefficients b_j are given in equations 2.25 and where

$$\frac{b_2}{b_1} \;=\; \frac{a_2}{b_1}+(1+2\varepsilon)\,. \tag{2.27}$$

Simplifying the coefficients in equation 2.27 using the quasi-acoustic approximation gives the same result as the simplified continued-fraction approximation of equation 2.19.

A similar wide-angle representation of the squared qSV vertical slowness is found by factoring a term $(1-(p\beta_0)^2)$ from equation 2.15. For such waves, $\beta_h = \beta_0$; this gives

$$q_\beta^2 = \frac{1}{\beta_0^2}\left(1-(p\beta_0)^2\right)\left(1-\sum_{j=0}^{\infty} d_j\,(p\beta_0)^{2j+2}\right), \tag{2.28}$$

where

$$\begin{aligned} &d_0 = 2\sigma, \\ &d_j = c_j + d_{j-1}, \qquad j=1,2,\ldots \end{aligned} \tag{2.29}$$

The corresponding wide-angle continued-fraction approximation for the squared qSV slowness in equation 2.28 is then given by

$$q_\beta^2 = \frac{1}{\beta_0^2}\left(1-(p\beta_0)^2\right)\left(1-d_0\,(p\beta_0)^2-\frac{d_1\,(p\beta_0)^4}{1-(d_2/d_1)\,(p\beta_0)^2}\right). \tag{2.30}$$

where the coefficients d_j are given in equation 2.29 and where

$$\frac{d_2}{d_1} \;=\; \frac{c_2}{d_1}+1. \tag{2.31}$$

Using the same approach as in the previous section, the simplified wide-angle continued-fraction approximation of the qSV squared slowness component is given by

$$q_\beta^2 = \frac{1}{\beta_0^2}\left(1-(p\beta_0)^2\right)\frac{1-2\,(\sigma-\delta)\,(p\beta_0)^2}{1+2\delta\,(p\beta_0)^2}, \tag{2.32}$$

providing a three-parameter representation of the squared qSV slowness. Hence, we have obtained a continued-fraction approximation that is exact at both vertical and horizontal directions of propagation at the cost of one extra parameter, i.e. δ (cf. equation 2.23).

2.5 Converted waves

We now consider wide-angle incident qP-waves. For the migration of converted waves, we are interested in the reflected qSV-wave for values of $p \leq 1/\alpha_h$. When $p > 1/\alpha_h$, the incident wave is beyond critical. Since evanescent qP-waves are not used in migration, we will ignore the range of horizontal slowness values $p > 1/\alpha_h$. To approximate the squared qSV curve with a best fit in the interval $0 \leq p \leq 1/\alpha_h$, we suggest approximating the squared qSV slowness in such a way that it is exact for vertical propagation and at $p = 1/\alpha_h$. With a similar approach as for the wide-angle approximations, we represent the qSV squared slowness by

$$\begin{aligned} q_\beta^2(p) =& \frac{1}{\beta_0^2}\left(1-(1+2\varepsilon)\,\gamma_0^2\,(p\beta_0)^2\right) \\ & \times\left(\left(1-\beta_0^2 q_{\beta,\alpha_h}^2\right)-\sum_{j=0}^{\infty} e_j\,(p\beta_0)^{2j+2}\right)+q_{\beta,\alpha_h}^2 \end{aligned}$$

where

$$q_{\beta,\alpha_h}^2 = \frac{1}{\alpha_0^2}+\frac{1}{\beta_0^2}-\frac{2}{\alpha_h^2}\,(1+\sigma+\delta)\,, \tag{2.33}$$

with

$$\begin{aligned} e_0 &= c_0-\left(1-\beta_0^2 q_{\beta,\alpha_h}^2\right)(1+2\varepsilon)\,\gamma_0^2 \\ &= 2\zeta, \\ e_j &= c_j+\gamma_0^2\,(1+2\varepsilon)\,e_{j-1}, \qquad j=1,2,\ldots \end{aligned} \tag{2.34}$$

Truncating the series in equation 2.33 will provide an approximation that is exact at both $p = 0$ and $p = 1/\alpha_h$. We denote this approximation as the C-wave wide-angle approximation. Instead of truncating the series, we can find the C-wave wide-angle continued -fraction expression. The resulting approximation is given

by

$$\begin{aligned} q_\beta^2(p) =& \frac{1}{\beta_0^2}\left(1-(1+2\varepsilon)\,\gamma_0^2\,(p\beta_0)^2\right) \\ &\times\left(1-\beta_0^2 q_{\beta,\alpha_h}^2-e_0\,(p\beta_0)^2-\frac{e_1\,(p\beta_0)^4}{1-(e_2/e_1)\,(p\beta_0)^2}\right)+q_{\beta,\alpha_h}^2, \end{aligned} \tag{2.35}$$

where the coefficients e_j are given in equation 2.34 and

$$\frac{e_2}{e_1}=\frac{(\delta-\sigma)}{\gamma_0^2\,(\varepsilon-\sigma)}\left(1+\frac{2\gamma_0^2\delta}{\gamma_0^2-1}\right)+\gamma_0^2\,(1+2\varepsilon)\,. \tag{2.36}$$

We stress that the expressions in equation 2.33 and 2.35 are only to be used for $0 \le p \le 1/\alpha_h$.

2.6 Discussion

In the Taylor-series expansions of the squared qP and qSV slowness, equations 2.12 and 2.15, respectively, the qSV coefficients are the qP coefficients multiplied by the factor γ_0^2, which may be large. When we compare these expansions, we note that for weak anisotropy, i.e. $(\varepsilon,\delta) \ll 1$, the coefficients a_0, a_1, and a_2 in the qP expression are only small compared to the coefficients c_0, c_1, and c_2 in the qSV expressions. The Taylor series for the qSV slowness thus converges more slowly than that for the qP slowness (Ursin and Stovas, 2006).

Continued-fraction approximations of the squared slowness can introduce artificial poles in the squared slowness expressions determined by the parameters. This occurs when the denominator approaches zero. For some parameter values, these poles can exist in the propagating domain, so the expressions are valid only for values of p away from these poles. After calculating the rational expression, one can check for zeros in the denominator. If a pole exists in the propagating domain, one can instead use the corresponding Taylor approximation from which the continued-fraction approximation was derived.

For the wide-angle approximations, the deviation from the exact expressions tend to be larger for intermediate values of the horizontal slowness component compared to, for example, the Taylor-series approximations, (cf. Figures 2.3 & 2.4). This is because we have constructed the wide-angle expressions such that they are exact at horizontal propagation.

Approximation	qP	qSV
Taylor	equation 2.12	equation 2.15
Continued fraction	equation 2.17	equation 2.21
Simplified continued fraction	equation 2.19	equation 2.23
Wide-angle Taylor	equation 2.24	equation 2.28
Wide-angle continued fraction	equation 2.26	equation 2.30
Simplified wide-angle continued fraction	equation 2.19	equation 2.32
C-wave wide-angle	—	equation 2.33
C-wave wide-angle continued fraction	—	equation 2.35

Table 2.1: The squared slowness approximations.

Parameters	α_0[km/s]	β_0[km/s]	ε	δ	σ
Model 1	2.0	1.0	0.10	0.05	0.20
Model 2	2.0	1.0	0.10	0.15	-0.20
Model 3	2.0	1.0	-0.05	0.05	-0.40
Model 4	3.1	1.5	0.26	-0.05	1.32
Model 5	2.0	1.0	-0.10	0.05	-0.60

Table 2.2: Parameters of the models used to computate the phase slowness approximations.

2.7 Numerical results

The derived equations for the squared slowness approximations are all listed in Table 2.1. To test the accuracy of the different approximations, we use five different VTI models. The model parameters are given in Table 2.2. In model 1, $\sigma > 0$, while $\sigma < 0$ in models 2 and 3.

Model 4 is the Greenhorn shale (Jones and Wang, 1981), which has an off-axis shear-wave triplication. In model 5, we have on-axis shear-wave triplications on both the vertical and horizontal axes, as discussed in Appendix 2.A. For phase-shift methods, one can prescribe an acceptable error Δq induced by the slowness approximation by limiting the corresponding phase error to be less than $\pi/4$. Hence, requiring that $\Delta q < 1/(8f\Delta z)$, where f denotes frequency and Δz is distance, would give an acceptable phase error. For example, by assuming a frequency of 60 Hz and a distance of 2000 m would imply that Δq should be less than 10^{-3} ms/m.

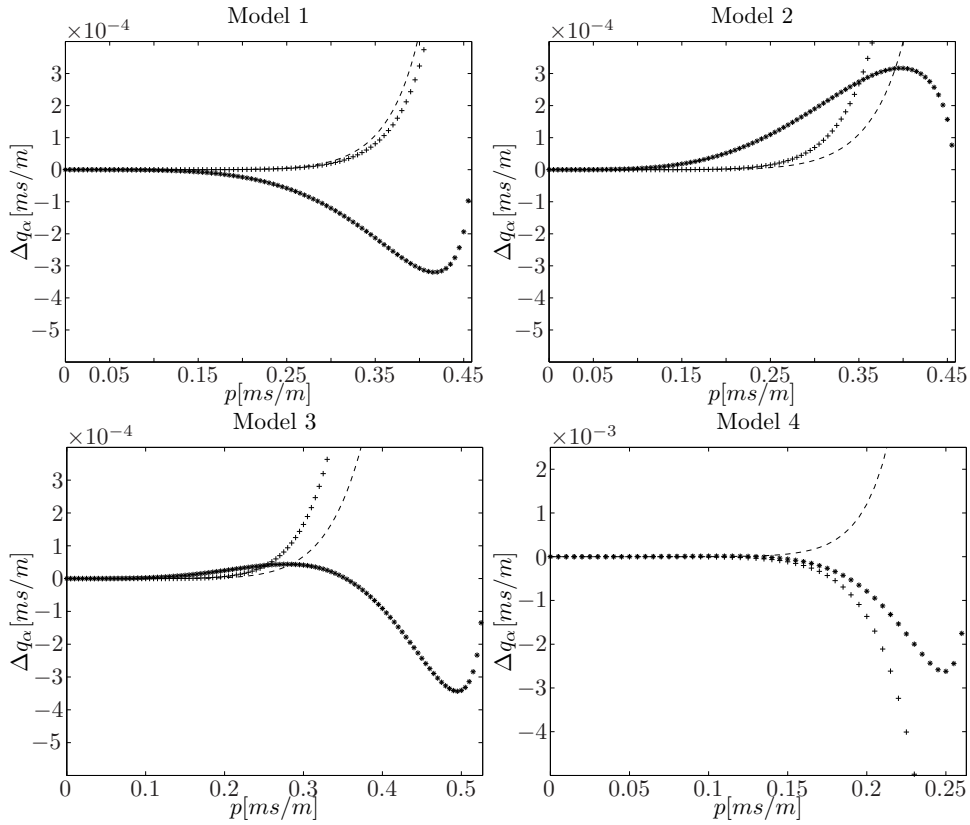

Figure 2.1: Comparison of the difference Δq_α between the exact qP and approximated qP slowness curves: the continued-fraction approximation with dashed line; the simplified continued-fraction approximation with asterisk; and the truncated Taylor expansion with crossed line.

To evaluate the approximations, we compute the exact and approximate expressions for qP and qSV slowness and plot the difference Δq as a function of p. For the Taylor approximations used in our comparison, we truncate, in all figures, the series in equations 2.12 and 2.15 at a_2 and c_2 for the qP and qSV approximations, respectively. For the wide-angle approximations used in our comparison, we truncate the series in equations 2.24 and 2.28 at b_2 and d_2 for the qP and qSVapproximations, respectively.

In Figure 2.1, we plot the difference between the exact qP slowness (equation 2.11) and the continued-fraction approximation (equation 2.17), the simplified

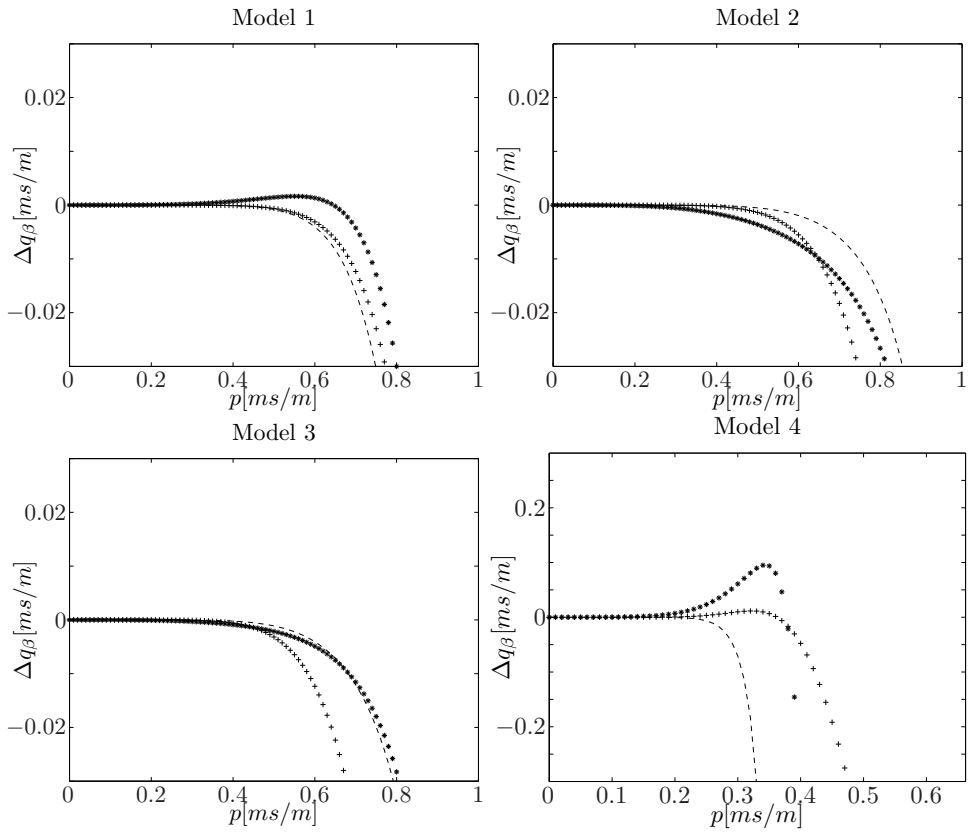

Figure 2.2: Comparison of the difference Δq_β between the exact qSV and approximated qSV slowness curves: the continued-fraction approximation with dashed line; the simplified continued-fraction approximation with asterisk; and the truncated Taylor expansion with crossed line.

continued-fraction approximation (equation 2.19), and the Taylor approximation (equation 2.12). Figure 2.2 is as Figure 2.1 but now for qSV waves; i.e., we used equations 2.21 and 2.23 for the continued-fraction approximation and its simplified equation, respectively, and equation 2.15 for the truncated Taylor series.

For all models both for qP- and qSV- waves, we see that when we approach wide angles, both the Taylor and continued-fraction approximations diverge rapidly away from the exact slowness. This indicates we should use these approximations only for small angles. The difference between the exact qSV slowness and the simplified qSV continued-fraction approximation is comparable

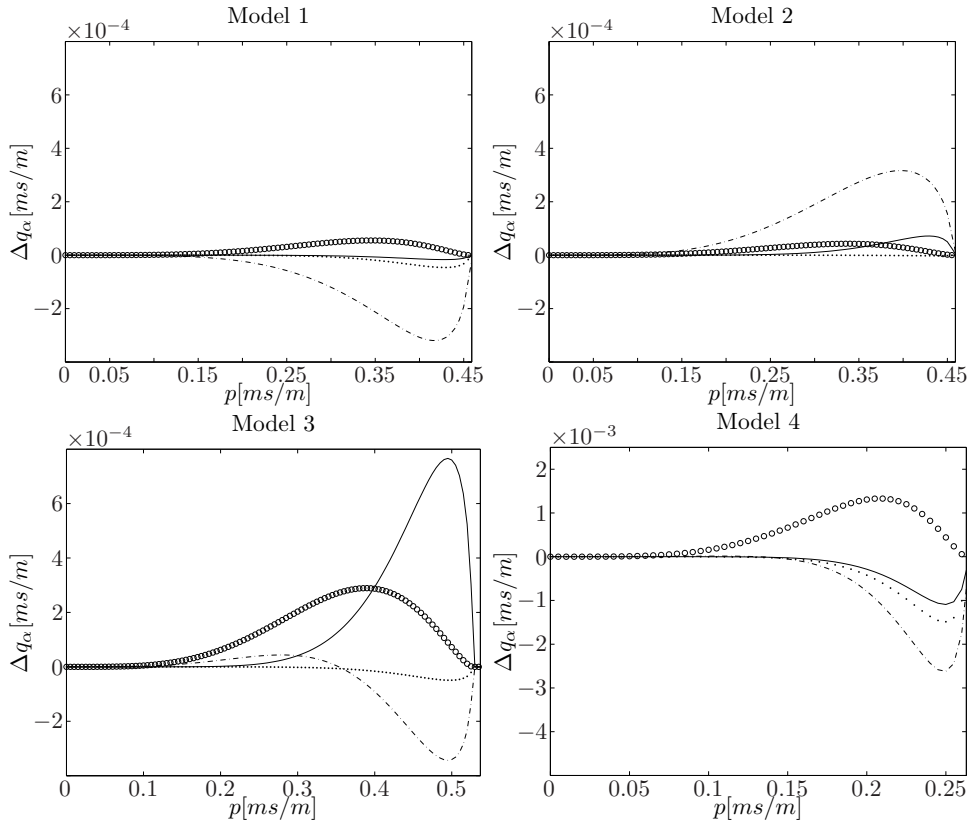

Figure 2.3: Comparison of the difference Δq_α between the exact qP and approximated qP slowness curves: the wide-angle approximation with solid line; the wide-angle continued-fraction approximation with dotted line; the simplified wide-angle continued-fraction approximation with dash-dotted line; and Schoenberg & deHoop's rational approximations with circles.

to the difference between the exact qSV slowness and the continuous fraction and Taylor approximations. We note that the simplified continued-fraction expressions of the qP slowness is exact for horizontal propagation; it thus can be used for wide angles.

Next, in Figure 2.3, we plot the difference between the exact qP slowness and wide-angle approximation (equation 2.24), the wide-angle continued-fraction approximation (equation 2.26), and the simplified wide-angle continued-fraction approximation (equation 2.19). We also include the difference from the explicit

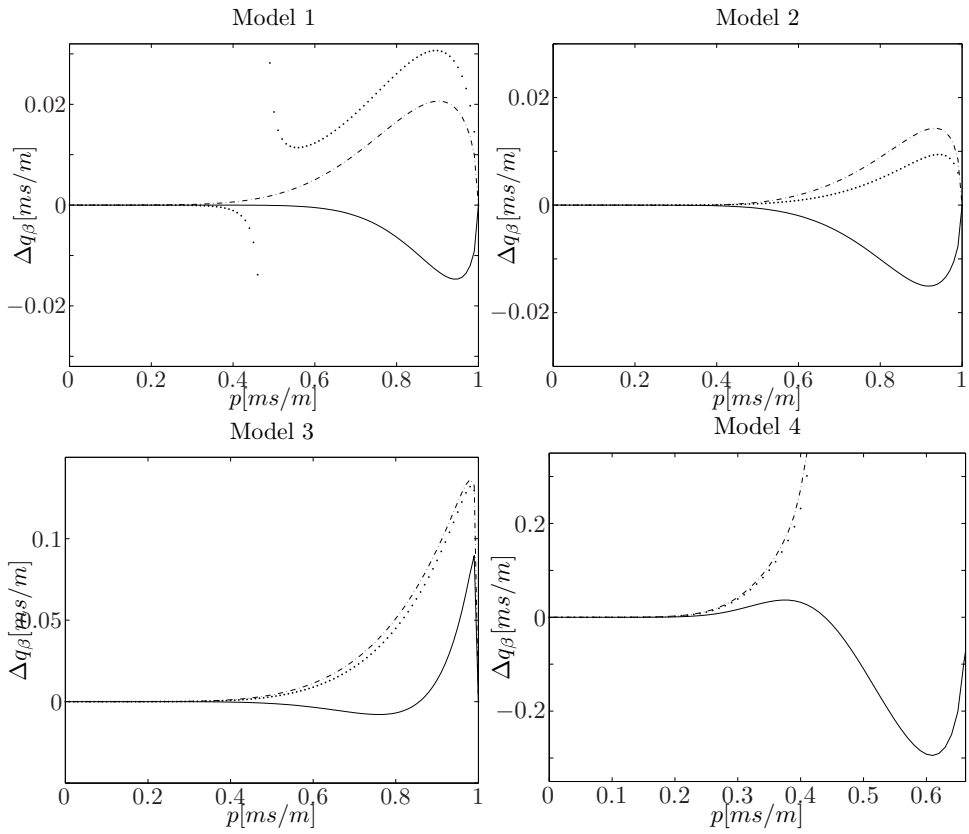

Figure 2.4: Comparison of the difference Δq_β between the exact qSV and approximated qSV slowness curves: the wide-angle approximation with solid line; the wide-angle continued-fraction approximation with dotted line; and the simplified wide-angle continued-fraction approximation with dash-dotted line.

qP approximation from Schoenberg and de Hoop (2000) (their equation 43). Their approximation contains four parameters, just like our wide-angle approximation (equation 20) and its continued-fraction approximation (equation 22). Figure 2.4 shows the difference between the qSV slowness and the wide-angle approximation (equation 2.28), the wide-angle continued-fraction approximation (equation 2.30), and the simplified wide-angle continued-fraction approximation (equation 2.32). Note that Model 1 gives a pole for the wide-angle continued-fraction approximation of qSV slowness. In Model 4, the squared wide-angle continued-fraction approximations become negative for large values of p, and we only plot the positive

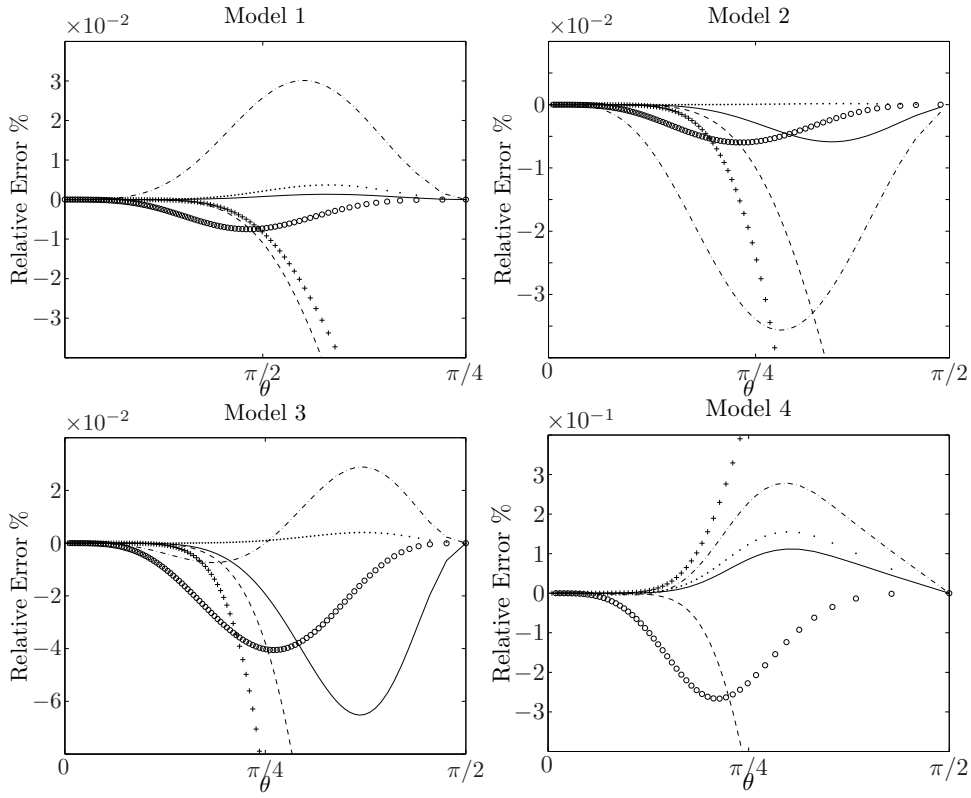

Figure 2.5: Comparison of the relative error in percent between the exact qP and approximated qP phase-velocities corresponding to the approximated slowness expressions: the continued-fraction approximation with dashed line; the truncated Taylor expansion with crossed line; the wide-angle approximation with solid line; the simplified wide-angle continued fraction with dash-dotted line; the wide-angle continued-fraction approximation with dotted line; and Schoenberg & deHoop's rational approximations with circles.

part.

In Figure 2.5 we plot the relative error in percent between the exact and approximated qP phase-velocity expressions corresponding to the derived slowness expressions as a function of phase angle θ. The phase angle θ is found through the relation $\tan\theta = p/q$, whereas the phase velocities $V(\theta) = 1/\sqrt{(p^2+q^2)}$. We find the values of the approximated phase velocities on the support points of the exact phase velocities through linear interpolation. Figure 2.6

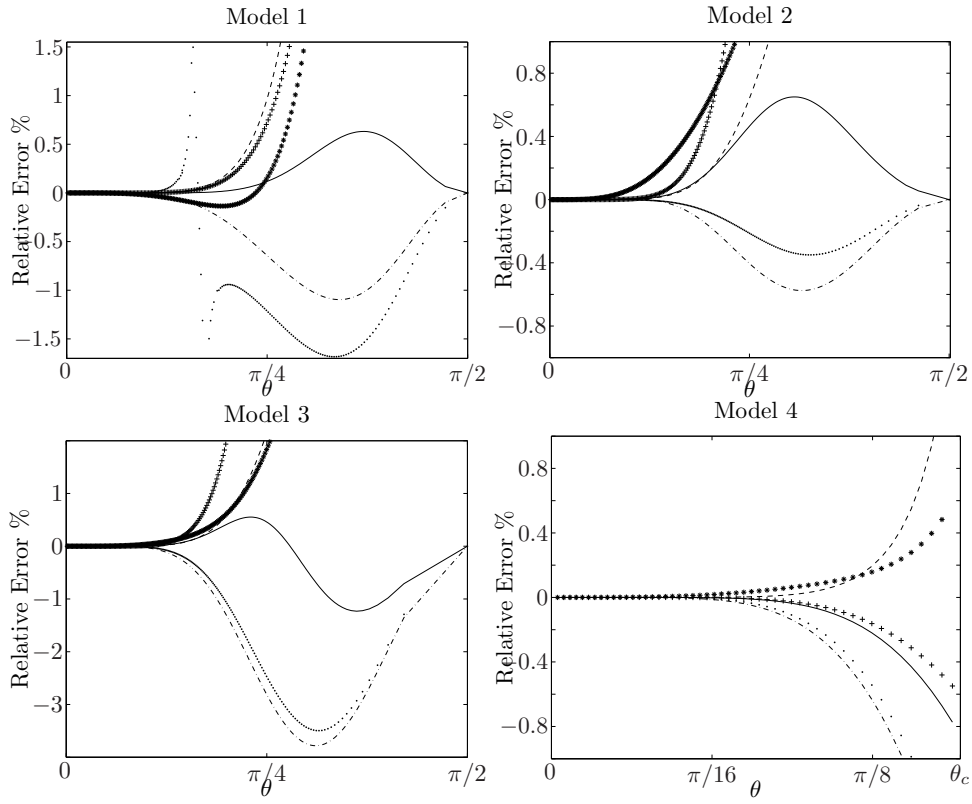

Figure 2.6: Comparison of the relative error in percent between the exact qSV and approximated qSV phase-velocities corresponding to the approximated slowness expressions: the continued-fraction approximation with dashed line; the simplified continued-fraction approximation with asterisk; the truncated Taylor expansion with crossed line; the wide-angle approximation with solid line; the wide-angle continued-fraction approximation with dotted line; and the simplified wide-angle continued-fraction approximation with dash-dotted line.

is as Figure 2.5, but for qSV waves. For model 4, we plot the phase velocities up to the angle that corresponds to the critical qP slowness, denoted θ_c.

Because we have on-axis shear-wave triplications in Model 5, the wide-angle qSV expressions are not valid. However, the qSV C-wave wide-angle expressions are valid for pre-critical qP values. In Figure 2.7 we plot Δq for the qP and qSV approximations, in addition to the corresponding relative error in the phase velocities.

We plot Δq_β for $0 \leq p \leq p_*$, where p_* denotes critical qP vertical slowness. The accuracy of the approximated qSV slowness for converted waves using the truncated Taylor series (equation 2.33) and the continued-fraction approximation (equation 2.35) are illustrated in Figure 2.8 only for the interval $0 \leq \theta \leq \theta_c$ where these approximations are valid. We note that this approximation is accurate for wide angles with an overall smaller error compared with the other qSV slowness approximations we have derived.

In summary, the wide-angle approximations are most accurate for the qP slowness in models 1 and 4, whereas the wide-angle continued-fraction approximation gives the best fit for the qP slowness in models 2 and 3. For qSV slowness, the wide-angle approximations provides the best approximation in models 1, 3 and 4 while the wide-angle continued-fraction approximation is best in Model 2. Both qSV C-wave wide-angle slowness approximations for converted waves on $0 \leq p \leq 1/\alpha_h$ provide accurate approximations on the interval $0 \leq p \leq 1/\alpha_h$.

2.8 Conclusions

We have derived simple and accurate wide-angle approximations for qP and qSV slowness in VTI media. The suggested approximations use four parameters, but using a quasi-acoustic approximation yields two- or three-parameter simplified approximations. The simplified continued-fraction approximation of the qP slowness is equivalent to the dispersion-relation approximation from Alkhalifah (1998).

The wide-angle approximation and its continued fraction equivalent for qP-waves provides the most accurate approximations for all models studied and are more accurate that the existing approximations of Schoenberg and de Hoop (2000). These approximations can be used for wavefield extrapolation in the content of migration. For $qP - qSV$-wave extrapolation, we need four parameters: three for qP extrapolation and one more for qSV extrapolation. We aim to use our approximations for $qP - qSV$ migration, so we suggest using the wide-angle continued-fraction expression (equation 2.26) for qP-waves and the C-wave wide-angle expression (equation 2.33) for qSV-waves because the qSV reflection angle is always smaller than the qP incident angle.

2.9 Acknowledgments

This research received financial support from the Norwegian Research Council via the ROSE project. We thank Joe Dellinger, Bertram Nolte, Steven Arcone, and the anonymous reviewers from *Geophysics* for numerous constructive remarks and suggestions that helped improve this paper.

2.A Horizontal on-axis shear-wave triplication

We show how a horizontal on-axis shear-wave triplication implies that the vertical qSV slowness curve is multivalued for some values of the horizontal slowness component p.

We rewrite equation 2.11 as

$$q_{\pm}^2(p) = \frac{1}{2}\left(q_{\alpha_0}^2 + q_{\beta_0}^2 - 2p^2\left(\sigma+\delta\right) \pm \sqrt{S\left(p\right)}\right), \tag{2.A-1}$$

with

$$\begin{aligned} S\left(p\right) = \left(q_{\beta_0}^2 - q_{\alpha_0}^2\right)^2 - 4\frac{p^2}{\alpha_0^2}\left(\gamma_0^2 - 1\right)\left(\sigma - \delta\right) \\ + 4p^4\left(2\frac{\left(\gamma_0^2-1\right)}{\gamma_0^2}\sigma + \left(\sigma+\delta\right)^2\right). \end{aligned} \tag{2.A-2}$$

First, we note that $q_-^2\left(p\right) = 0$ for

$$p = \frac{1}{\alpha_h}, \tag{2.A-3}$$

where α_h is given in equation 2.20, so that $q_-^2\left(p\right)$ represents the qP-wave for $0 \leq p \leq 1/\alpha_h$. As a consequence, $q_+^2\left(p\right)$ represents the qSV-wave for $0 < p < 1/\alpha_h$.

For a horizontally traveling qSV-wave, the horizontal slowness is $p = 1/\beta_0$ and

$$q_{\pm}^2\left(\frac{1}{\beta_0}\right) = \frac{1}{2}\left(F \pm \left|F\right|\right), \tag{2.A-4}$$

where

$$F = \frac{1 - \gamma_0^2(1 + 2\delta + 2\sigma)}{\alpha_0^2}. \tag{2.A-5}$$

For

$$\sigma \geq -1/2 - \delta + 1/(2\gamma_0^2) \tag{2.A-6}$$

we have $F \leq 0$ and thus $q_+^2(1/\beta_0) = 0$. Further, we have $q_-^2(1/\beta_0) < 0$; hence q^2 for qSV waves is single valued because we ignore evanescent waves. Therefore, there is no horizontal on-axis triplication in this case and $q_+^2(p)$ represents the qSV-wave for $0 \leq p \leq 1/\beta_0$. However, in the case

$$\sigma < -1/2 - \delta + 1/(2\gamma_0^2) \tag{2.A-7}$$

we have $F > 0$, so that $q_-^2(1/\beta_0) = 0$ and $q_+^2(1/\beta_0) > 0$. This is the case of a horizontal on-axis triplication (Musgrave, 1970; Thomsen and Dellinger, 2003); it implies a multivalued (real) vertical slowness. In the case of a horizontal on-axis triplication, letting p_* (with $p_* > 1/\beta_0$) denote the horizontal slowness p for which $S(p_*) = 0$, it follows from 2.A-1 that

$$q_+^2(p_*) = q_-^2(p_*). \tag{2.A-8}$$

The squared qSV slowness curve is then given by

$$q_\beta^2(p) = \begin{cases} q_+^2(p), & 0 \leq p \leq p_*, \\ q_-^2(p), & 1/\beta_0 \leq p \leq p_*. \end{cases} \tag{2.A-9}$$

Because $q_\pm(p_*) > 0$, q_β is multivalued for $1/\beta_0 \leq p \leq p_*$. For $1/\beta_0 \leq p \leq p_*$, the lower part of the squared slowness curve goes from $q_-^2(1/\beta_0) = 0$ to the value at $p = p_*$, which is equal to $q_+^2(p_*)$ because $S(p_*) = 0$.

As an example, we consider the VTI medium 5 in Table 2.2 with $\sigma = -0.6 < -1/2 - \delta + 1/(2\gamma_0^2) = -0.5188$, thus having a horizontal on-axis shear-wave triplication. In Figure 2.9, we plot the squared slowness $q_\pm^2$ for this model. The slowness curves for the qP- and qSV-waves are plotted in Figure 2.10, where the horizontal on-axis triplication of the qSV-wave is evident from the concave shape of the slowness surface near the horizontal axis.

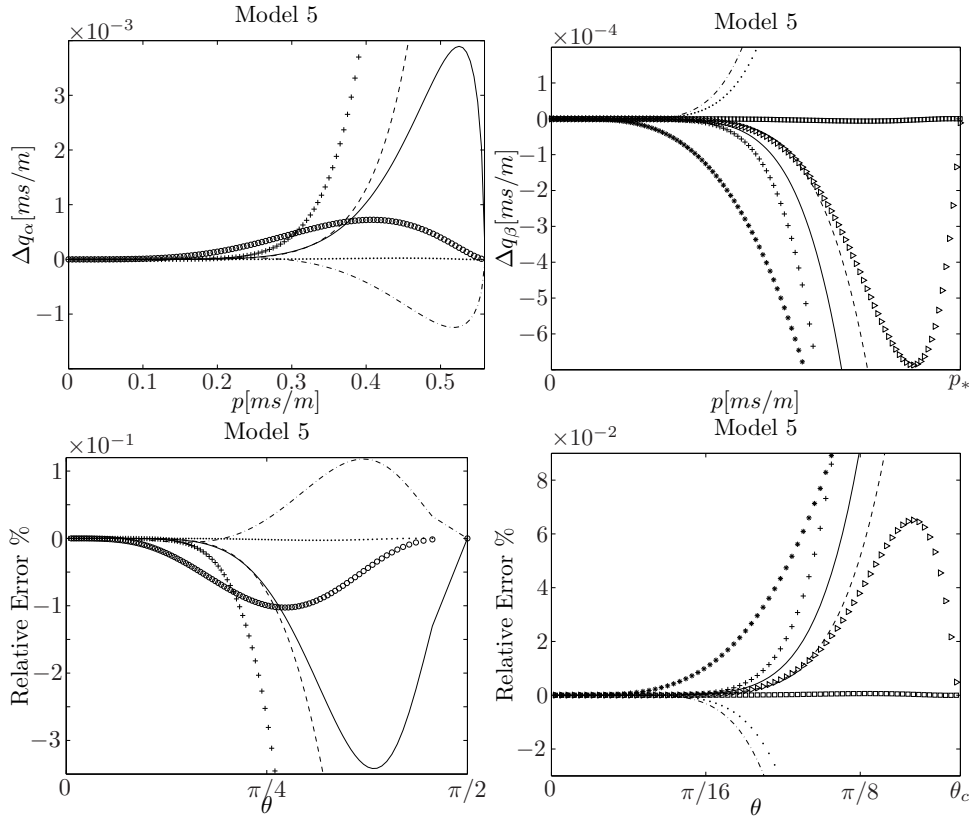

Figure 2.7: Comparison of the difference Δq (top) between exact and approximated qP (left) and qSV (right) slowness curves, and the error in corresponding phase-velocities (bottom): the continued fraction approximation with dashed line; the simplified continued-fraction approximation with asterisk; the truncated Taylor expansion with crossed line; the wide-angle approximation with solid line; the wide-angle continued-fraction approximation with dotted line; the simplified wide-angle continued-fraction with dash-dotted line; Schoenberg & deHoop's rational approximation with circles; the C-wave wide-angle approximation with squared line; and the C-wave wide-angle continued-fraction approximation with triangles.

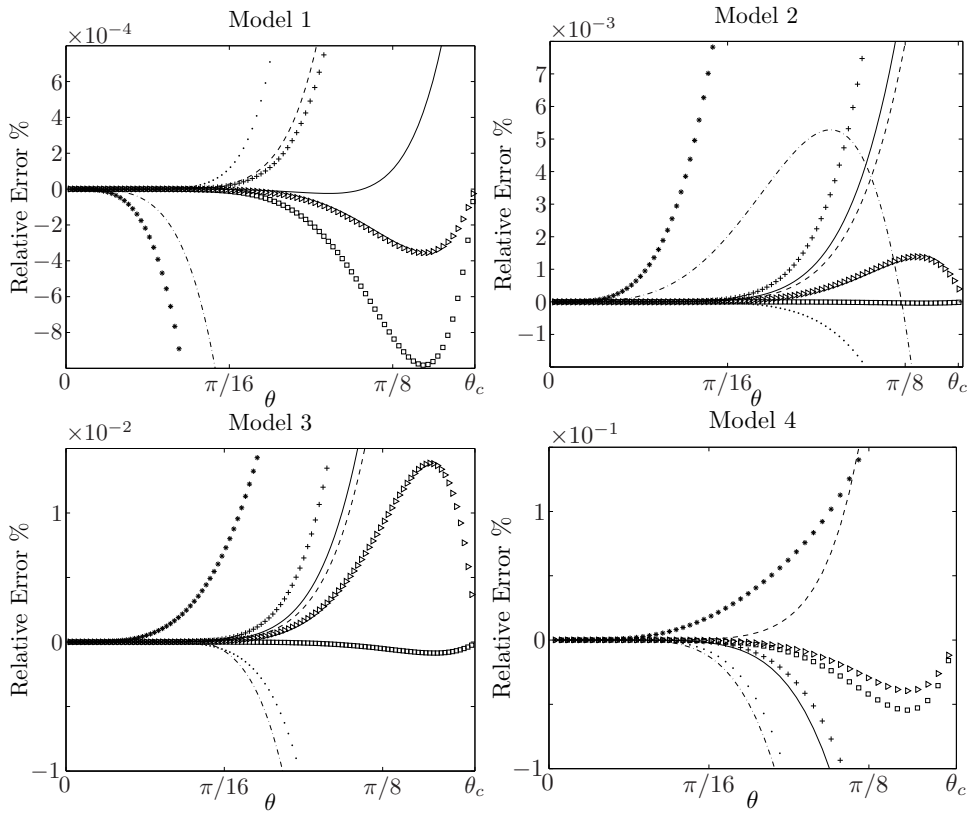

Figure 2.8: The relative error in percent between the exact qSV and approximated qSV phase-velocities corresponding to the approximated slowness expressions: the continued-fraction approximation with dashed line; the simplified continued-fraction approximation with asterisk; the truncated Taylor expansion with crossed line; the wide-angle approximation with solid line; the wide-angle continued-fraction approximation with dotted line; the simplified wide-angle continued-fraction approximation with dash-dotted line; the C-wave wide-angle approximation with squared line; and the C-wave wide-angle continued-fraction approximation with triangles.

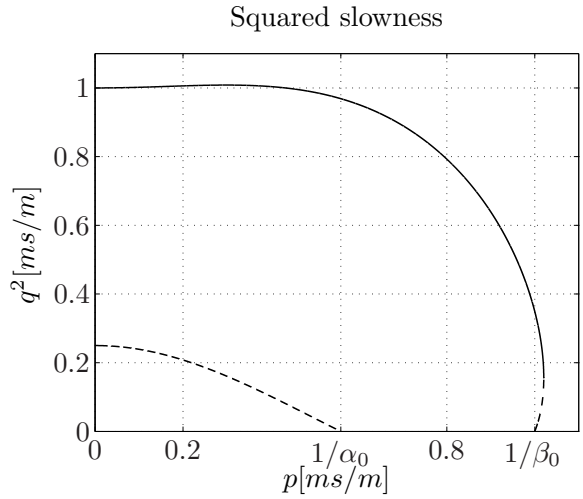

Figure 2.9: The squared slowness curves for on-axis shear-wave triplications. The solid line is q_+^2 and the dashed line is q_-^2, both from equation 2.A-1.

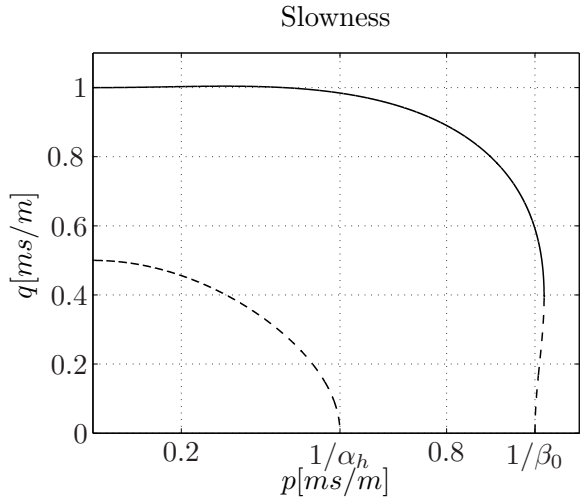

Figure 2.10: The slowness curves for on-axis shear-wave triplications. The solid line is q_+ and the dashed line is q_-, both from equation 2.A-1.

Chapter 3

One-way wave-equation migration of compressional and converted waves in a VTI medium

Ørjan Pedersen [1] and Bjørn Ursin[1] and Hans-Kristian Helgesen[2]

[1] *Norwegian University of Science and Technology, Department of Petroleum Engineering and Applied Geophysics*
[2] *StatoilHydro ASA*

In seismic reflection surveying, by recording both pressure and shear-wave reflections, one can increase the amount of information obtained about the subsurface than by recording pressure waves alone. Geologic structures which are not visible by using conventional pressure-data may possibly be imaged using shear waves, thus mitigating the risk in oil and gas exploration and production. Horizontally layered sedimentary rocks exhibit anisotropy that can be approximated by an effective transverse isotropic medium with a vertical axis of symmetry. Taking into account a vertically transverse isotropic Earth, we derive phase-slowness expressions for quasi-P and quasi-SV waves which are used in a one-way wave-equation migration scheme. We derive simplified slowness-expressions which are useful for processing of conventional pressure data. Numerical examples demonstrate that the slowness approximations are valid for wide-angle propagation, and the resulting one-way propagators are validated on a series of synthetic tests and applied on a field ocean-bottom seismic dataset. The results show that the method accurately images both compressional and converted waves in OBS data over a vertically transverse isotropic medium.

3.1 Introduction

In seismic reflection surveying, by deploying both hydrophones and geophones at the seafloor as in e.g. ocean-bottom seismic (OBS) surveying, it is possible to record both pressure and shear-wave reflections from the subsurface. By combining both pressure and shear-wave reflections, one can increase the amount of information about the subsurface than obtained with pressure waves alone (Hokstad, 2000). A dominant part of the seismic energy recorded on the horizontal geophone components is energy that has experienced conversion from pressure waves to shear waves at subsurface reflectors. Converted shear-wave data can possibly be used to image subsurface reflectors which are weak using pressure data alone, especially in gas-charged formations (Granli et al., 1999; MacLeod et al., 1999; Barkved et al., 2004), hence reducing the risk in hydrocarbon exploration and production. Shear-wave information may also help improve reservoir characterization by providing further constraints on rock properties, lithology, and fracture density and orientation.

The Earth is anisotropic in nature and in particular sedimentary rocks exhibit anisotropy. These sedimentary rocks may often be described as being transverse isotropic with a symmetry axis perpendicular to the bedding plane.

A homogeneous medium which is fractured may also be described as being transverse isotropic, now with a symmetry axis perpendicular to the fractures. A transversely isotropic media with a vertical symmetry axis (VTI) often presents a good model for the description of real rocks. The characteristics of wave-propagation in a VTI medium can be described by the dispersion relation, relating the vertical and horizontal phase-slowness. Seismic waves, and shear waves in particular, are sensitive to anisotropy.

There are several migration methods used in subsurface imaging. Depending on their underlying assumptions, these methods can usually be classified as either Kirchhoff (Schneider, 1978; Sun et al., 2000) or wavefield extrapolation (Bleistein, 1987; Gazdag, 1978; Stolt, 1978) methods. Kirchhoff methods explicitly introduce a high-frequency approximation of the wave-equation. In areas with complex geology where multi-pathing occurs, Kirchhoff methods may not provide reliable subsurface images (Biondi, 2006). In wavefield extrapolation methods, multi-pathing is handled in a natural way. Two-way wave extrapolation methods, provide an accurate description of wave propagation, however, the computational cost and challenges in noise when creating subsurface images can become a limitation. One-way wavefield extrapolation methods are routinely used in 3D depth migration of seismic data. Since one-way methods separate the wavefields into up- and downgoing wavefield constituents, they are not valid for horizontally traveling wavefield components. Because of their efficient computer implementations and robustness, one-way methods have become increasingly popular and a wide variety of methods has been introduced (Gazdag, 1978; Stolt, 1978; Gazdag and Sguazzero, 1984; Stoffa et al., 1990; Wu and Huang, 1992; Ristow and Rühl, 1994).

Utilizing an isotropic propagator for migration in a VTI medium may lead to position errors of subsurface structures (Larner and Cohen, 1993; Alkhalifah and Larner, 1994; Vestrum et al., 1999). In a VTI medium with no lateral variations where all medium parameters are known, the dispersion relation can be used directly in phase-shift migration methods (Gazdag, 1978; Alkhalifah, 2000b), and provides an accurate description of the kinematics of wave-propagation. If we allow the medium to contain small lateral variations, a split-step Fourier approach (Stoffa et al., 1990) accounts for the zero-order lateral perturbations in the medium parameters. To be able to exploit the phase-shift approach efficiently with a fast Fourier transform, and in addition provide an accurate description of wave-propagation in an isotropic laterally varying media, the scalar generalized-screen (Wu and Huang, 1992; Rousseau and de Hoop, 2001a) or Fourier finite-difference (FFD) method (Ristow and Rühl, 1994) can be used.

The isotropic generalized-screen approach was extended to VTI media by Rousseau and de Hoop (2001b). A simplified dispersion relation for qP waves was developed by Alkhalifah (1998, 2000a). Based on this dispersion relation, Han and Wu (2005) develop a one-way propagator using a screen approximation with a finite difference correction term. Xie and Wu (2005) present a multicomponent prestack depth migration method utilizing the elastic screen method. Nolte (2005) describes a technique for converted-wave (C-wave) migration in anisotropic media with VTI symmetry using FFD methods through least-squares fitting of finite difference coefficients to an anisotropic dispersion relation.

We derive one-way propagators for compressional and converted-waves through a Fourier finite-difference approach based on a representation of the (squared) vertical slowness as a function of horizontal slowness. We provide a simplified vertical-slowness approximation involving fewer parameters which can be used in processing of compressional waves where not all medium parameters are available. The accuracy of the derived one-way propagators is demonstrated in 2D on synthetic data and in 3D on OBS field data from the Volve field in the central North sea.

3.2 Theory

We consider a VTI medium which is described by its stiffness coefficients in the Voigt notation c_{ij}. For a VTI medium the only non-zero stiffness coefficients are (Thomsen, 1986)

$$\begin{bmatrix} c_{11} & c_{11}-2c_{66} & c_{13} & & & \\ c_{11}-2c_{66} & c_{11} & c_{13} & & & \\ c_{13} & c_{13} & c_{33} & & & \\ & & & c_{44} & & \\ & & & & c_{44} & \\ & & & & & c_{66} \end{bmatrix}. \tag{3.1}$$

In terms of density and stiffness coefficients, the vertical qP velocity is given by

$$\alpha_0 = \sqrt{\frac{c_{33}}{\rho}}, \tag{3.2}$$

and the vertical quasi-SV (qSV) velocity is given by

$$\beta_0 = \sqrt{\frac{c_{44}}{\rho}}, \tag{3.3}$$

where ρ denotes the density of the medium. The Thomsen (1986) parameters ε and δ are defined in terms of the stiffness coefficients by

$$\begin{aligned} \varepsilon &= \frac{c_{11} - c_{33}}{2c_{33}}, \\ \delta &= \frac{(c_{13} + c_{44})^2 - (c_{33} - c_{44})^2}{2c_{44}\,(c_{33} - c_{44})}, \end{aligned} \tag{3.4}$$

and allows us to describe a VTI medium by the parameters α_0, β_0, δ and ε. For notational convenience, we introduce the parameters

$$\begin{aligned} \gamma_0 &= \frac{\alpha_0}{\beta_0}, \\ \zeta &= \varepsilon - \delta, \\ \sigma &= \gamma_0^2 \zeta, \\ \chi &= 1 + 2\delta. \end{aligned} \tag{3.5}$$

The dispersion relation relates the vertical and the horizontal slowness and can be found by inserting the stiffness coefficients in matrix 3.1 into the Christoffel equation (see for example Červenỳ (2001)). This relation can be expressed in terms of the Thomsen parameters ε, δ and the vertical qP and the vertical qSV phase velocities α_0 and β_0. It can be solved for the squared vertical slowness q^2 as a function of horizontal-slowness p, both for qP- and qSV-wave modes.

From the dispersion relation, the squared vertical slowness for qP- and qSV-waves in a VTI medium can be expressed by (Stovas and Ursin, 2003; Ursin and Stovas, 2006)

$$\begin{aligned} q_{\alpha,\beta}^2 = &\frac{1}{2}\left(q_{\alpha_0}^2 + q_{\beta_0}^2 - 2p^2\,(\sigma + \delta)\right) \\ &\mp \frac{1}{2}\Bigg[\left(q_{\beta_0}^2 - q_{\alpha_0}^2\right)^2 - 4\frac{p^2}{\alpha_0^2}\left(\gamma_0^2 - 1\right)(\sigma - \delta) \\ &+ 4p^4\left(2\frac{(\gamma_0^2 - 1)}{\gamma_0^2}\sigma + (\sigma + \delta)^2\right)\Bigg]^{\frac{1}{2}}, \end{aligned} \tag{3.6}$$

where $q_{\alpha_0}^2 = 1/\alpha_0^2 - p^2$ and $q_{\beta_0}^2 = 1/\beta_0^2 - p^2$. With no horizontal on-axis shear-wave triplication (Musgrave, 1970; Thomsen and Dellinger, 2003), the negative sign in front of the radical corresponds to the qP slowness and the positive sign corresponds to the qSV slowness. In case of a horizontal on-axis shear-wave triplication, q_β is multi-valued for some values of p (Pedersen et al., 2007). This

means that q_β^2 has a concave shape near the horizontal axis, that is, when p is close to $1/\beta_0$, and is described by both the positive and negative sign in front of the radical. To get the vertical wave-number k_z, the vertical slowness q can be written as $q = k_z/\omega$, while the horizontal-slowness p can be written $p = k_x/\omega$ where k_x is the lateral wave-number.

For simplicity in our derivations, we assume that we consider a 2D VTI medium where we can describe the parameters α_0 and β_0, and the anisotropy parameters ε and δ, as functions of both depth z and spatial position x. An extension to 3D is straight forward. The medium is divided into thin depth-slabs of thickness Δz, where the parameters are assumed constant in depth within each slab and the lateral medium variations are smooth. Given a wavefield $\Psi(z,:)$ at some depth z, the solution of the one-way wave-equation provides the thin-slab propagator (Claerbout, 1985)

$$\Psi(z+\Delta z,:) = \mathrm{e}^{\pm \mathrm{i}\Delta z \omega q(p,x)}\Psi(z,:), \tag{3.7}$$

where the superscript sign corresponds to backward(-) and forward(+) propagation. Extrapolating the wavefield using equation 3.7 is expensive (Holberg, 1988). More efficient one-way propagators can be constructed by an approximation of the thin-slab propagator given in equation 3.7.

We will focus on an approximation of the thin-slab propagator similar to the FFD approach, as described by Ristow and Rühl (1994), where the propagator is separated into a phase-shift propagator in a background medium and a spatial finite-difference correction accounting for the varying model components.

By introducing a constant background medium for each slab in a VTI medium, described by the parameters α_0^0, β_0^0, ε^0, and δ^0, we can represent the vertical slowness as

$$q_{\alpha,\beta}(p,x) = q^0_{\alpha,\beta}(p) + \Delta q_{\alpha,\beta}(p,x), \tag{3.8}$$

where $q^0_{\alpha,\beta}(p)$ denotes the vertical slowness in the background medium and $\Delta q_{\alpha,\beta}(p,x)$ denotes the phase-correcting term. Within a depth slab, each background medium parameter can be chosen as the minimum within each slab.

The wavefield is globally propagated in the background medium in vertical slowness domain using $q^0_{\alpha,\beta}(p)$, and locally corrected for the vertical-slowness perturbations with an approximation of the phase-correcting term $\Delta q_{\alpha,\beta}(p,x)$ through a finite-difference scheme in space. The vertical slowness is independent of lateral position in the background medium, hence we can accurately propagate the wavefield in the background medium utilizing a phase-shift operator using the exact expression in equation 3.6.

When we consider the phase-correcting term, we notice that it is a non-linear function of both lateral position x and horizontal-slowness p, hence we need to decouple the spatial and horizontal-slowness dependency. Thus, for the phase-correcting term, we represent the vertical-slowness on the following form:

$$q_{\alpha,\beta} = \sum_{j\geq 0} k_j^{\alpha,\beta}(x)\, l_j^{\alpha,\beta}(p)\,. \tag{3.9}$$

Following the FFD approach (Ristow and Rühl, 1994) we truncate the series expansion in equation 3.9. These expressions will provide a vertical-slowness approximation that can be used in constructing one-way propagators in an FFD approach after cascading by a continued-fraction approximation.

3.3 Slowness expressions for qP- and qSV-waves

By a series representation of the square-root term in equation 3.6, the squared qP slowness can be written as

$$q_\alpha^2 = \frac{1}{\alpha_0^2}\left(1 - \sum_{j\geq 0} a_j\,(p\alpha_0)^{2j+2}\right) \tag{3.10}$$

with

$$\begin{aligned} a_0 &= \chi, \\ a_1 &= \frac{2\sigma}{\gamma_0^2}\left(1 + \frac{2\gamma_0^2\delta}{\gamma_0^2 - 1}\right), \\ a_2 &= \frac{-4\sigma}{\gamma_0^2\left(\gamma_0^2 - 1\right)}(\delta - \sigma)\left(1 + \frac{2\gamma_0^2\delta}{\gamma_0^2 - 1}\right). \end{aligned} \tag{3.11}$$

The higher-order coefficients of the square-root expansion can be found in Ursin and Stovas (2006, equation B-9). To express the vertical slowness for qP-waves on polynomial form as given in equation 3.9 (and hence being able to separate the spatial and wave-number dependencies), we take the square-root of equation 3.10.

By a Taylor expansion of the square root of equation 3.10 around $p = 0$ we obtain

$$q_\alpha = \frac{1}{\alpha_0}\left(1 - \sum_{j\geq 0} \tilde{a}_j\,(p\alpha_0)^{2j+2}\right) \tag{3.12}$$

where the first three coefficients $\tilde{a}_j$ in terms of a_j are

$$\begin{aligned}\tilde{a}_0 &= \frac{1}{2}a_0,\\ \tilde{a}_1 &= \frac{1}{2}a_1 + \frac{1}{8}a_0^2,\\ \tilde{a}_2 &= \frac{1}{2}a_2 + \frac{1}{4}a_0a_1 + \frac{1}{16}a_0^3,\end{aligned} \tag{3.13}$$

thus q_α is on desired form as represented in equation 3.9.

For qSV-waves, we find a series expansion of the squared vertical slowness as:

$$q_\beta^2 = \frac{1}{\beta_0^2}\left(1 - \sum_{j\geq 0} c_j \left(p\beta_0\right)^{2j+2}\right) \tag{3.14}$$

where

$$\begin{aligned}c_0 &= 1 + 2\sigma,\\ c_j &= -a_j\gamma_0^{2j}, \qquad j \geq 1.\end{aligned} \tag{3.15}$$

By a similar approach as for the slowness approximation of qP-waves, we find a slowness approximation for qSV-waves given by

$$q_\beta = \frac{1}{\beta_0}\left(1 - \sum_{j\geq 0} \tilde{c}_j \left(p\beta_0\right)^{2j+2}\right) \tag{3.16}$$

where the first three coefficients $\tilde{c}_j$ in terms of c_j are

$$\begin{aligned}\tilde{c}_0 =& \frac{1}{2}c_0,\\ \tilde{c}_1 =& \frac{1}{2}c_1 + \frac{1}{8}c_0^2,\\ \tilde{c}_2 =& \frac{1}{2}c_2 + \frac{1}{4}c_0c_1 + \frac{1}{16}c_0^3.\end{aligned} \tag{3.17}$$

The representation of the qP- and qSV-slowness can now be cascaded by continued-fraction approximations. By cascading the expression in 3.12, we find that the qP slowness can be approximated by

$$q_\alpha = \frac{1}{\alpha_0}\left(1 + \kappa_2^\alpha p^2 + \frac{\kappa_1^\alpha p^2}{1 - \kappa_0^\alpha p^2}\right), \tag{3.18}$$

where

$$\begin{aligned}\kappa_0^{\alpha} =& \frac{\tilde{a}_2}{\tilde{a}_1}\alpha_0,\\ \kappa_1^{\alpha} =& \frac{\tilde{a}_1^2}{\tilde{a}_2}\alpha_0^2,\\ \kappa_2^{\alpha} =& \left(\tilde{a}_0 - \frac{\tilde{a}_1^2}{\tilde{a}_2}\right)\alpha_0.\end{aligned} \tag{3.19}$$

Similar for the qSV-waves, by cascading the slowness approximation for qSV-waves in equation 3.16, we find

$$q_{\beta} = \frac{1}{\beta_0}\left(1 + \kappa_2^{\beta}p^2 + \frac{\kappa_1^{\beta}p^2}{1 - \kappa_0^{\beta}p^2}\right), \tag{3.20}$$

where

$$\begin{aligned}\kappa_0^{\beta} =& \frac{\tilde{c}_2}{\tilde{c}_1}\beta_0,\\ \kappa_1^{\beta} =& \frac{\tilde{c}_1^2}{\tilde{c}_2}\beta_0^2,\\ \kappa_2^{\beta} =& \left(\tilde{c}_0 - \frac{\tilde{c}_1^2}{\tilde{c}_2}\right)\beta_0.\end{aligned} \tag{3.21}$$

3.4 Simplified slowness expressions for qP-waves

For conventional towed streamer data, only qP-waves are recorded. In this case it is convenient to consider simplified expressions of the vertical slowness for qP-waves where the qSV-wave velocity is disregarded, i.e. a quasi-acoustic approximation (Alkhalifah, 1998). In the quasi-acoustic approximation, we assume that $\gamma_0^2 \gg 1$, and a simplified slowness expression for qP waves can be provided by (Alkhalifah, 1998; Pedersen et al., 2007)

$$q_{\alpha}^{s} = \frac{1}{\alpha_0}\sqrt{\frac{1 - (1+2\varepsilon)(p\alpha_0)^2}{1 - 2\zeta(p\alpha_0)^2}}, \tag{3.22}$$

where the superscript s denotes a quasi-acoustic approximation. Equation 3.22 can be found by a continuous-fraction approximation that matches the Taylor expansion of q_{α}^2 given in equation 3.10 up to $(p\alpha)^6$ and setting $\gamma_0^2 \gg 1$.

From the quasi-acoustic approximation and equations 3.11, we find

$$\begin{aligned} a_0^s &= \chi, \\ a_1^s &= 2\chi\zeta, \\ a_2^s &= 4\zeta^2\chi, \end{aligned} \tag{3.23}$$

and the Taylor-expanded vertical-slowness can be approximated by the truncated series

$$q_\alpha^s = \frac{1}{\alpha_0}\left(1 - \sum_{j=0}^{2} a_j^s (p\alpha_0)^{2j+2}\right). \tag{3.24}$$

By substituting the simplified parameters a_j^s into equations 3.19 we find

$$\begin{aligned} \kappa_0^{\alpha,s} =& \frac{2\zeta^2 + \frac{1}{2}\zeta\chi + \frac{1}{16}\chi^2}{\zeta + \frac{1}{8}\chi}\alpha_0, \\ \kappa_1^{\alpha,s} =& \frac{\zeta^2\chi^2 + \frac{1}{4}\zeta\chi^3 + \frac{1}{64}}{2\zeta^2\chi + \frac{1}{2}\zeta\chi^2 + \frac{1}{16}\chi^3}\alpha_0^2, \\ \kappa_2^{\alpha,s} =& \left(\frac{1}{2}\chi - \frac{\zeta^2\chi^2 + \frac{1}{4}\zeta\chi^3 + \frac{1}{64}}{2\zeta^2\chi + \frac{1}{2}\zeta\chi^2 + \frac{1}{16}\chi^3}\right)\alpha_0. \end{aligned} \tag{3.25}$$

Thus, a simplified cascaded qP-slowness expression can be found by inserting the simplified coefficients $\kappa_i^{\alpha,s}$ into equation 3.18, that is

$$q_\alpha^s = \frac{1}{\alpha_0}\left(1 + \kappa_2^{\alpha,s}p^2 + \frac{\kappa_1^{\alpha,s}p^2}{1 - \kappa_0^{\alpha,s}p^2}\right). \tag{3.26}$$

3.5 Accuracy of slowness expressions

We compare the accuracy of the Taylor-expanded slowness expressions in equations 3.12 and 3.16 and the cascaded slowness expressions in equations 3.18 and 3.20 for qP and qSV waves, respectively. The performance of the slowness approximations is illustrated using two models, where the Taylor-expanded series are truncated at $j = 2$. We also show the accuracy of the quasi-acoustic qP slowness expression given by equation 3.24 on polynomial form and equation 3.26 on cascaded form.

The medium parameters in model 1 is defined by $\alpha_0 = 2.00$ km/s, $\beta_0 = 1.00$ km/s, $\varepsilon = 0.10$ and $\delta = 0.05$ and the medium parameters in model 2 is

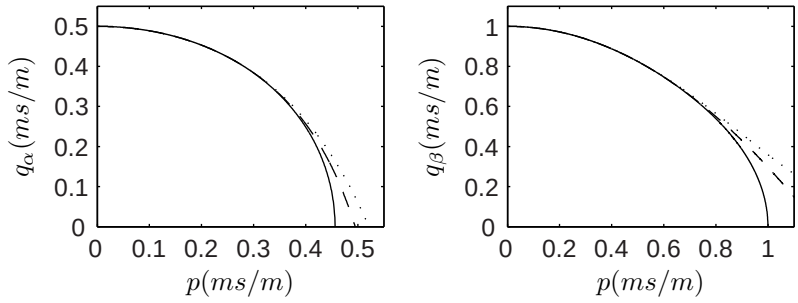

Figure 3.1: Slowness surfaces for $\alpha_0 = 2.0$ km/s, $\beta_0 = 1.0$ km/s, $\varepsilon = 0.10$ and $\delta = 0.05$. (a) The exact qP slowness curve in solid line; the Taylor-expanded qP slowness curve in dotted line; and the cascaded qP slowness curve in dashed line. (b) The exact qSV slowness curve in solid line; the Taylor-expanded qSV slowness curve in dotted line; and the cascaded qSV slowness curve in dashed line.

defined by $\alpha_0 = 2.00$ km/s, $\beta_0 = 1.00$ km/s, $\varepsilon = 0.10$ and $\delta = 0.15$. In Figures 3.1(a) and 3.1(b) we plot the derived slowness curves for qP- and qSV-waves in model 1, respectively. The qP approximations is accurate up to about $p = 0.4$ [ms/m] and the qSV approximations up to about $p = 0.7$ [ms/m]. For both wavemodes, the cascaded approximation is more accurate than the Taylor-expanded approximation. Similar results are observed for model 2, as illustrated in Figures 3.2(a) and 3.2(b).

The derived quasi-acoustic slowness curves for model 1 and 2 are shown in Figures 3.3(a) and 3.3(b). The accuracy of the quasi-acoustic approximations are similar to that of the $qP - qP$ approximations.

To quantify the accuracy, it is usefull to show the relative error of the group-velocity as a function of group-angle corresponding to the exact and approximated dispersion relations. For example Berryman (1979) provides a description of how the group-velocity and group-angle can be found.

Figure 3.4 shows the relative error in group-velocity as a function of group-angle for model 1, where the dashed and solid line corresponds to the Taylor-expanded and the cascaded approximation, respectively. Figure 3.4(a) shows the qP and Figure 3.4(b) shows the qSV approximations. If one allows the relative error to be less than 1 $\%$, the cascaded qP and qSV approximations are valid up to about 60° in model 1. In model 2, the cascaded qP approximation has less than 1 $\%$ relative error up to about 70° while the cascaded qSV approximation is

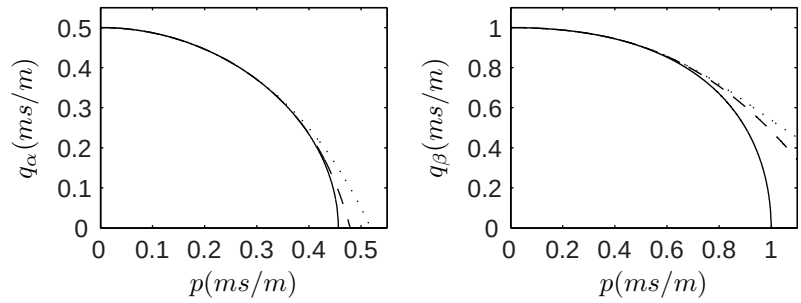

(a) (b)

Figure 3.2: Slowness surfaces for $\alpha_0 = 2.0$ km/s, $\beta_0 = 1.0$ km/s, $\varepsilon = 0.10$ and $\delta = 0.15$. (a) The exact qP slowness curve in solid line; the Taylor-expanded qP slowness curve in dotted line; and the cascaded qP slowness curve in dashed line. (b) The exact qSV slowness curve in solid line; the Taylor-expanded qSV slowness curve in dotted line; and the cascaded qSV slowness curve in dashed line.

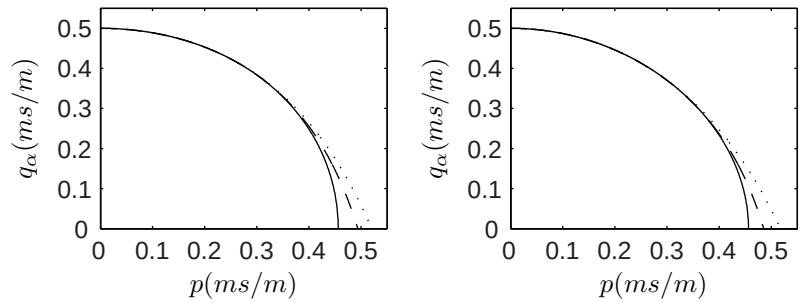

(a) (b)

Figure 3.3: (a) Slowness surfaces for $\alpha_0 = 2.0$ km/s, $\beta_0 = 1.0$ km/s, $\varepsilon = 0.10$ and $\delta = 0.05$. (b) Slowness surfaces for $\alpha_0 = 2.0$ km/s, $\beta_0 = 1.0$ km/s, $\varepsilon = 0.10$ and $\delta = 0.15$. The exact qP slowness curve in solid line; the quasi-acoustic Taylor-expanded qP slowness curve in dotted line; and the quasi-acoustic cascaded qP slowness curve in dashed line.

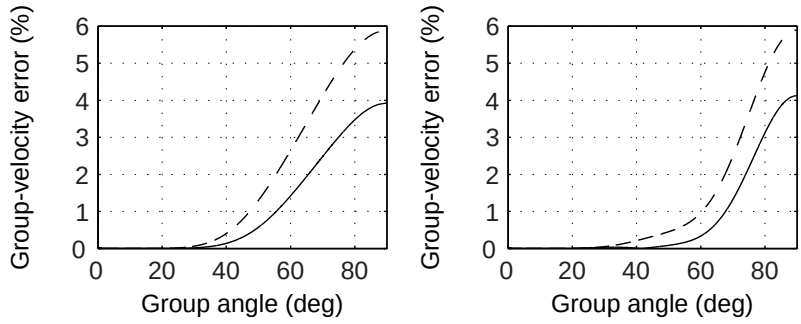

(a) (b)

Figure 3.4: Relative group-velocity error as a function of group-angle for $\alpha_0 = 2.0$ km/s, $\beta_0 = 1.0$ km/s, $\varepsilon = 0.10$ and $\delta = 0.05$. The Taylor-expanded group-velocity in dashed line and the cascaded group velocity in solid line corresponding to (a) the qP and (b) the qSV slowness approximations.

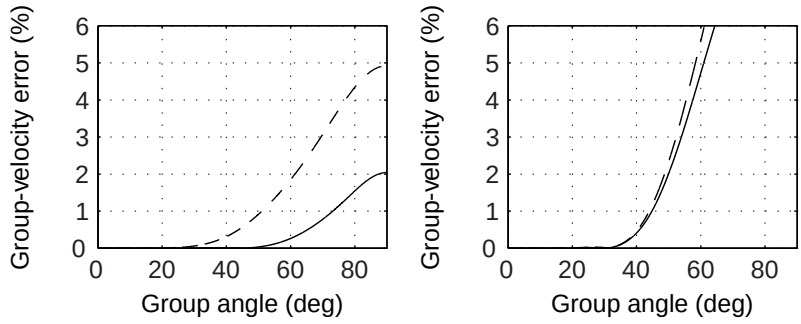

(a) (b)

Figure 3.5: Relative group-velocity error as a function of group-angle for $\alpha_0 = 2.0$ km/s, $\beta_0 = 1.0$ km/s, $\varepsilon = 0.10$ and $\delta = 0.15$. The Taylor-expanded group-velocity in dashed line and the cascaded group velocity in solid line corresponding to (a) the qP and (b) the qSV slowness approximations.

valid up to about 40° and is shown in Figure 3.5. The group-velocity errors for the quasi-acoustic approximations are shown in Figure 3.6(a) and 3.6(b) for model 1 and model 2, respectively. The results are similar to the qP approximations.

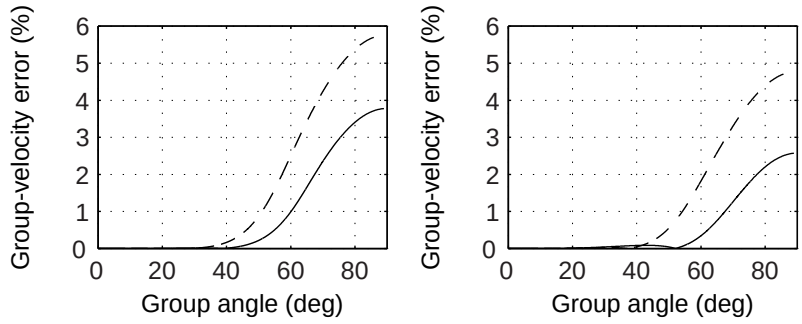

(a) (b)

Figure 3.6: Group-velocity error as a function of group-angle for the quasi-acoustic approximations. The Taylor-expanded group-velocity in dashed line and the cascaded group velocity in solid line for (a) $\alpha_0 = 2.0$ km/s, $\beta_0 = 1.0$ km/s, $\varepsilon = 0.10$ and $\delta = 0.05$ and (b) $\alpha_0 = 2.0$ km/s, $\beta_0 = 1.0$ km/s, $\varepsilon = 0.10$ and $\delta = 0.15$

3.6 One-way propagators

Introducing a laterally invariant background medium allows us to define a vertical slowness perturbation Δq_α using equation 3.12. Further, by cascading Δq_α by a continued fraction approximation, we find from equation 3.7 that the resulting one-way propagator for qP-waves can be represented by

$$e^{i\omega\Delta z q_\alpha(p,x)} \approx e^{i\omega\Delta z q^0_\alpha(p)} e^{i\omega\Delta z \Delta q_\alpha(p,x)}. \tag{3.27}$$

In a similar fashion, we find that the qSV propagator can be represented by

$$e^{i\omega\Delta z q_\beta(p,x)} \approx e^{i\omega\Delta z q^0_\beta(p)} e^{i\omega\Delta z \Delta q_\beta(p,x)}. \tag{3.28}$$

See the Appendix for a detailed derivation of Δq_α and Δq_β.

For each frequency, the phase-shift in the background medium is applied to the wavefield in slowness domain, while the phase-correcting term handling the vertical-slowness perturbation is applied in space domain by a finite-difference approach in a similar fashion as described by Ristow and Rühl (1994).

In an OBS experiment with a downgoing pressure source field (D^{qP}) in a fluid and by recording pressure and particle velocity at the seafloor, we can find the upgoing pressure wavefield (U^{qP}) and the upgoing shear wavefield (U^{qSV}) at the sea floor by wavefield decomposition (Amundsen and Reitan, 1995; Osen et al., 1996).

For pre-stack migration, a C-wave subsurface image, denoted $I^{qP,qSV}$, can be constructed using the following imaging condition

$$I^{qP,qSV}(z,:) = \sum_k \sum_\omega U_k^{qSV}(z,:) D_k^{qP}(z,:)^* \tag{3.29}$$

and a $qP - qP$ subsurface image, denoted $I^{qP,qP}$, can be constructed using the following imaging condition

$$I^{qP,qP}(z,:) = \sum_k \sum_\omega U_k^{qP}(z,:) D_k^{qP}(z,:)^*, \tag{3.30}$$

where the superscript $*$ denotes complex conjugate (Claerbout, 1971) and

$$\begin{aligned} D^{qP}(z+\Delta z,:) =& \mathrm{e}^{\mathrm{i}\omega \Delta z q_\alpha(p,x)} D^{qP}(z,:) \\ U^{qP}(z+\Delta z,:) =& \mathrm{e}^{-\mathrm{i}\omega \Delta z q_\alpha(p,x)} U^{qP}(z,:) \\ U^{qSV}(z+\Delta z,:) =& \mathrm{e}^{-\mathrm{i}\omega \Delta z q_\beta(p,x)} U^{qSV}(z,:). \end{aligned} \tag{3.31}$$

The subscript k denotes shot number for common-shot migration and receiver number for common-receiver migration.

3.7 Numerical results

In this section we use the derived migration schemes to produce impulse responses for both compressional and converted waves. These tests are usefull for illustrating the capabilities to image steep-dips with the proposed scheme in media with lateral medium perturbations. Further, we test the ability of the derived migration scheme to handle a complex subsurface with a relative high degree of medium perturbations on a 2D synthetic data example.

3.7.1 Impulse responses

To demonstrate the accuracy of the derived one-way propagators, we first produce a series of impulse response tests. The impulse response test involves migrating a single input seismic trace in a given medium. The input trace contains a single spike located at time 2.0 s.

First,we consider a medium given by $\alpha_0 = 2000.0$ m/s, $\beta_0 = 1000.0$ m/s, $\delta = 0.0$ and $\varepsilon = 0.1$. By introducing a background medium given by $\alpha_0^0 = 1000.0$ m/s, $\beta_0^0 = 750.0$ m/s, $\delta^0 = 0.0$ and $\varepsilon^0 = 0.1$ we can illustrate the ability of

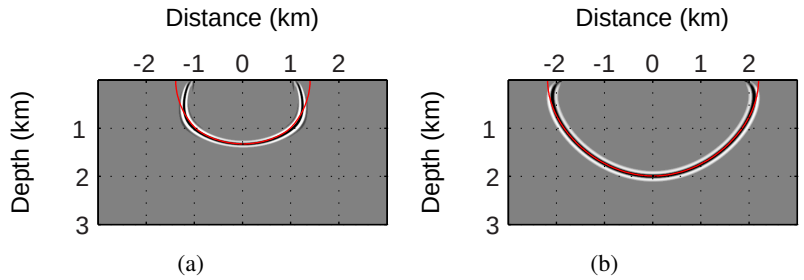

Figure 3.7: Impulse responses of $qP - qSV$ (a) and $qP - qP$ (b) waves with analytically computed impulse response overlaid. The medium is given by $\alpha_0 = 2000.0$ m/s; $\beta_0 = 1000.0$ m/s; $\delta = 0.0$; and $\varepsilon = 0.1$ with a background medium given by $\alpha_0^0 = 1000.0$ m/s; $\beta_0^0 = 750.0$ m/s; $\delta^0 = 0.0$; and $\varepsilon^0 = 0.1$

the derived one-way propagators to handle the resulting lateral medium variations. The impulse response for the C-wave migration is shown in Figure 3.7(a). By inspection, we see that the proposed one-way propagators in this example are accurate up to about 50°. For larger angles the error introduced by the medium perturbations cause the impulse response to be mis-positioned. This is mainly due to the inaccuracy of the qSV slowness approximation for large angles, which diverges from the exact qSV slowness.

The impulse response for the $qP - qP$ migration is shown in Figure 3.7(b). We see that the proposed propagator is accurate up to about 70°.

In our next example, we change the anisotropy parameters such that $\delta = 0.05$ and $\varepsilon = 0.10$ with and $\delta^0 = 0.05$ and $\varepsilon^0 = 0.10$. The impulse responses are shown in Figure 3.8. The accuracy of the C-wave and $qP - qP$ migration is similar for both wavemodes as in the previous example. Further, we change the anisotropy parameters such that $\delta = 0.05$ and $\varepsilon = 0.25$ with and $\delta^0 = 0.05$ and $\varepsilon^0 = 0.25$. The impulse responses are shown in Figure 3.9. The $qP - qP$ impulse response is reasonably accurate as the previous examples. The C-wave impulse response shows that the C-wave migration is accurate up to about 45°. For angles above 45°, the wavefront is mis-positioned.

In general, the accuracy of the derived one-way propagators for high dips depends on the variation of the medium properties. That is, for high dips the propagators are more accurate for small medium variations than for larger medium variations.

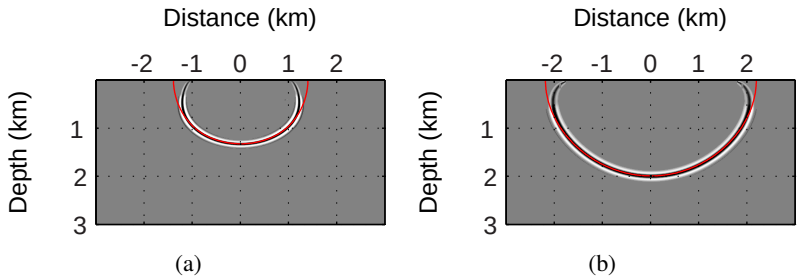

Figure 3.8: Impulse responses of $qP - qSV$ (a) and $qP - qP$ (b) waves with analytically computed impulse response overlaid. The medium is given by $\alpha_0 = 2000.0$ m/s; $\beta_0 = 1000.0$ m/s; $\delta = 0.05$; and $\varepsilon = 0.1$ with a background medium given by $\alpha_0^0 = 1000.0$ m/s; $\beta_0^0 = 750.0$ m/s; $\delta^0 = 0.05$; and $\varepsilon^0 = 0.1$

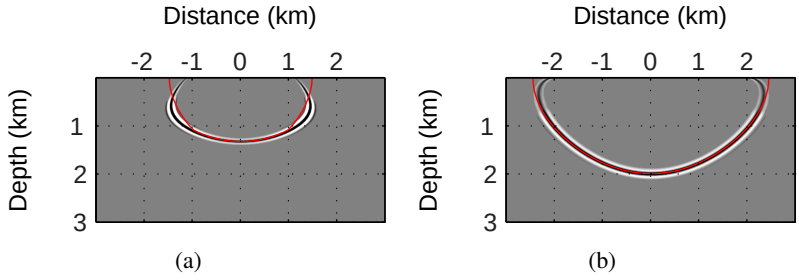

Figure 3.9: Impulse responses of $qP - qSV$ (a) and $qP - qP$ (b) waves with analytically computed impulse response overlaid. The medium is given by $\alpha_0 = 2000.0$ m/s; $\beta_0 = 1000.0$ m/s; $\delta = 0.05$; and $\varepsilon = 0.25$ with a background medium given by $\alpha_0^0 = 1000.0$ m/s; $\beta_0^0 = 750.0$ m/s; $\delta^0 = 0.05$; and $\varepsilon^0 = 0.25$

3.7.2 2D Synthetic data example

Next, the accuracy of the kinematics of the proposed one-way propagators is demonstrated on a 2D synthetic dataset.

A synthetic common-shot dataset was produced using a Born-Kirchhoff-Helmholtz modelling scheme (Ursin and Tygel, 1997; Sollid and Ursin, 2003) both for $qP - qP$ and $qP - qSV$ waves. The dataset model parameters are shown in Figure 3.10. The model consists of 5 reflecting interfaces and the response from the sea-floor is not modelled. The sources are located at the sea surface, while the receiver cable is located at the seafloor at depth 100 m. Each shot contains 161 receivers with separated by 20 m, and the shots are distributed with a distance of 20 m. Figure 3.11 depict selected shot-gathers which are input to migration.

The migrated sections are shown in Figure 3.12, where Figure 3.12(a) depicts the migrated $qP - qP$ data and Figure 3.12(b) depicts the migrated $qP - qSV$ data. Above the sea-floor, $\beta_0 = \delta = \varepsilon = 0$, thus the downgoing source pressure wavefield U^{qP} is propagated using an isotropic phase-shift down to the sea-floor. From the results, we see that both the C-wave and $qP - qP$-wave migration provide accurate results. The difference between the migrated sections is not very distinct, and the reflector interpretation would most likely coincide for both sections. We notice that the migrated $qP - qSV$ image has higher resolution than the migrated $qP - qP$ image since the shear-wave velocities are slower than the pressure velocities.

3.8 3D Real ocean-bottom data example

We apply the derived one-way propagators on a 3D field OBS dataset. The OBS dataset was acquired in 2002 in the central North Sea over the Volve field. The field is located in the Sleipner area in the southern part of the Viking Graben.

A subset of the entire 3D survey was extracted for input to a common-receiver migration scheme. A 2D section of the derived model parameters (Szydlik et al., 2007) are shown in Figure 3.14, where Figure 3.14(a) shows the vertical qP-wave velocity; Figure 3.14(b) shows the vertical qSV-wave velocity; Figure 3.14(c) shows the Thomsen parameter δ; and Figure 3.14(d) shows the Thomsen parameter ε. The model parameters correspond to inline 68 in the subset of the survey. In Figure 3.15, the model parameters for crossline 232 is shown. The extracted dataset contains 12 cables of 6 km length, each with 240 receivers. The shots are separated by 50-by-50 m. In Figure 3.16, selected shot-gathers are shown, where Figure 3.16(a) shows a $qP - qP$ gather and Figure 3.16(b) shows a $qP - qSV$

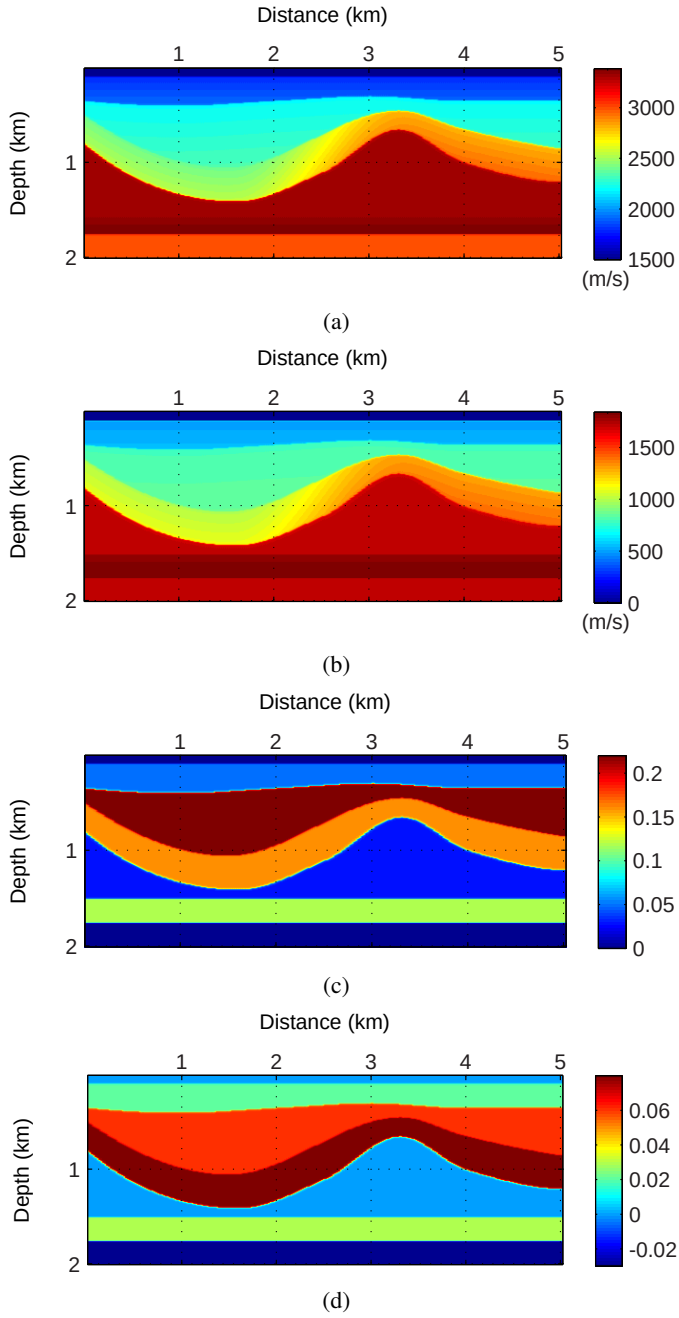

Figure 3.10: Model parameters for the synthetic data example. (a) Vertical qP-wave velocity α_0; (b) vertical qSV-wave velocity β_0; (c) Thomsen parameter ε; and (d) Thomsen parameter δ.

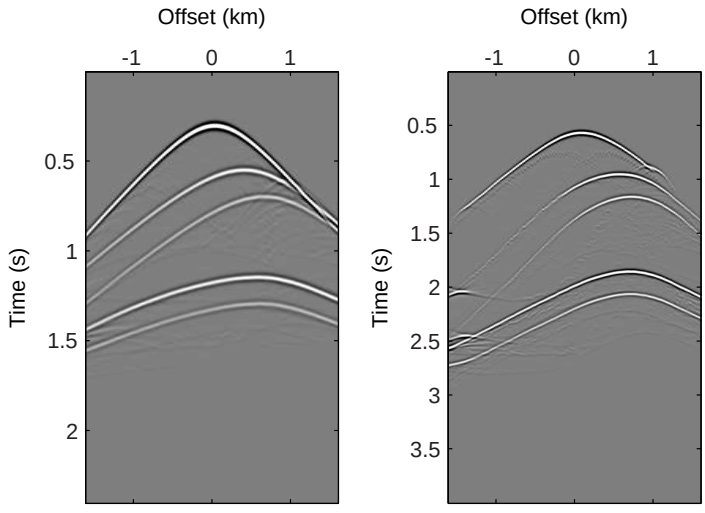

Figure 3.11: Selected synthetic shot-gathers - for a source at surface location 2500 m - which are input to migration. (a) $qP - qP$ shot gather and (b) $qP - qSV$ shot gather.

gather. The data is migrated in a common-receiver migration scheme.

From the stacked migrated datasets I^{qP-qP} and I^{qP-qSV} we extract two sections; one along (inline 68) and one across (crossline 232) the OBS cables indicated by the dashed lines in Figure 3.13. The sections I^{qP-qP} and I^{qP-qSV} for inline 68 are shown in Figures 3.17 and 3.18, respectively. The sections I^{qP-qP} and I^{qP-qSV} for crossline 232 are shown in Figures 3.19 and 3.20, respectively. A side-by-side comparison of I^{qP-qP} and I^{qP-qSV} for inline 68 is shown in Figure 3.21 and for crossline 232 in Figure 3.22. No post-processing has been applied after imaging except a gain in depth for displaying purposes.

In general, the migrated images I^{qP-qP} and I^{qP-qSV} show good structural focusing. The two images correlate well in depth. We notice that the migrated I^{qP-qP} image show better reflector continuity in the deeper part than the migrated I^{qP-qSV} image and thereby seems to be better focused. Some differences are found between the distinction of some of the reflectors in the deeper part below about 3 km. These differences are most probably due to differences in the reflectivity for the converted waves.

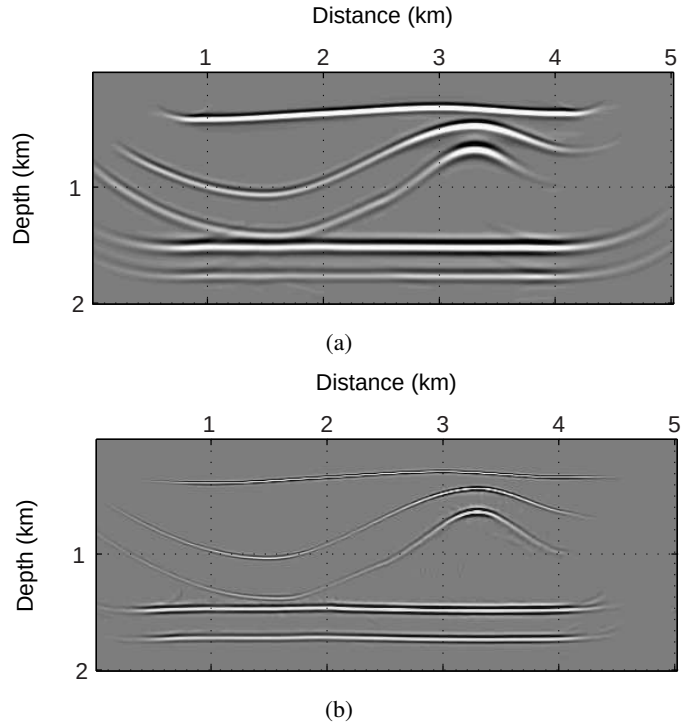

Figure 3.12: Migrated section of the synthetic data example. (a) $qP - qP$-stack and (b) $qP - qSV$-stack.

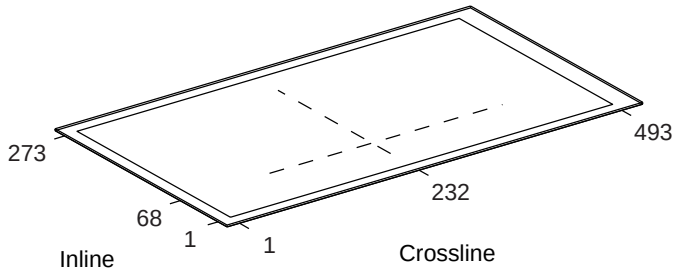

Figure 3.13: Representation of the coverage used in migration of the 3D field data example. Extracted I^{qP-qP} and I^{qP-qSV} sections are indicated by dashed lines and displayed in Figures 3.17; 3.18; 3.19; and 3.20.

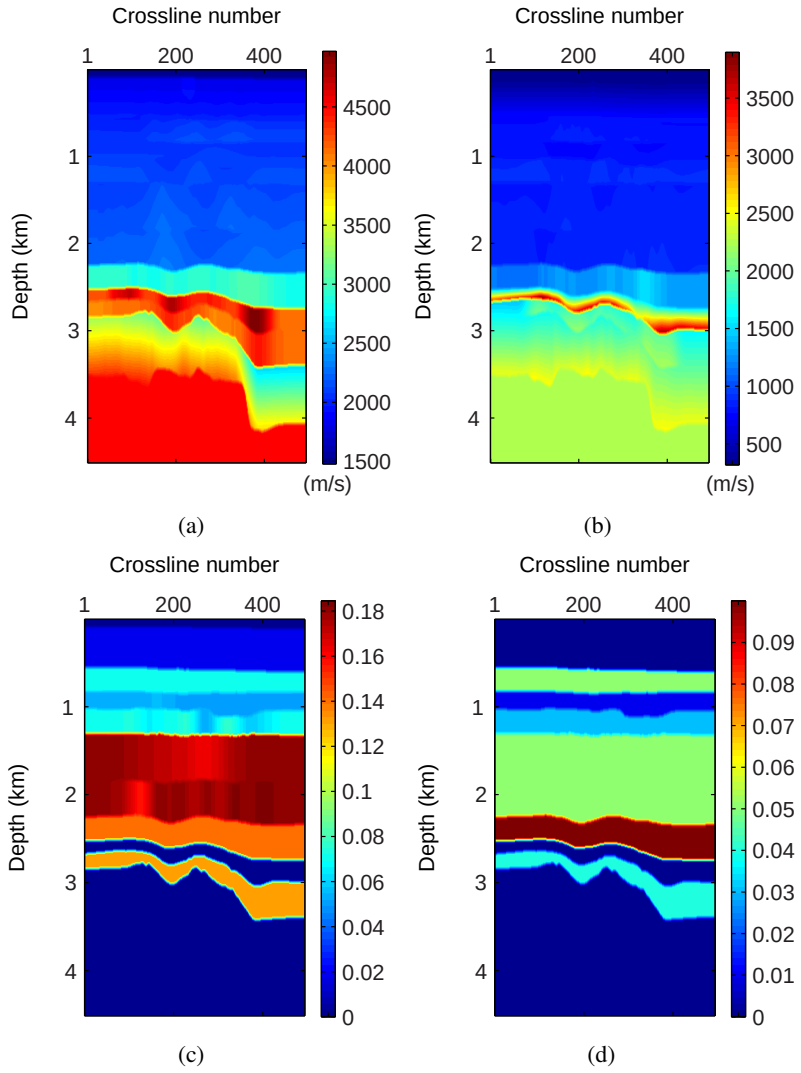

Figure 3.14: Model parameters for the real data example from offshore Norway at inline 68. (a) Vertical qP-wave velocity α_0; (b) vertical qSV-wave velocity β_0; (c) Thomsen parameter ε; and (d) Thomsen parameter δ.

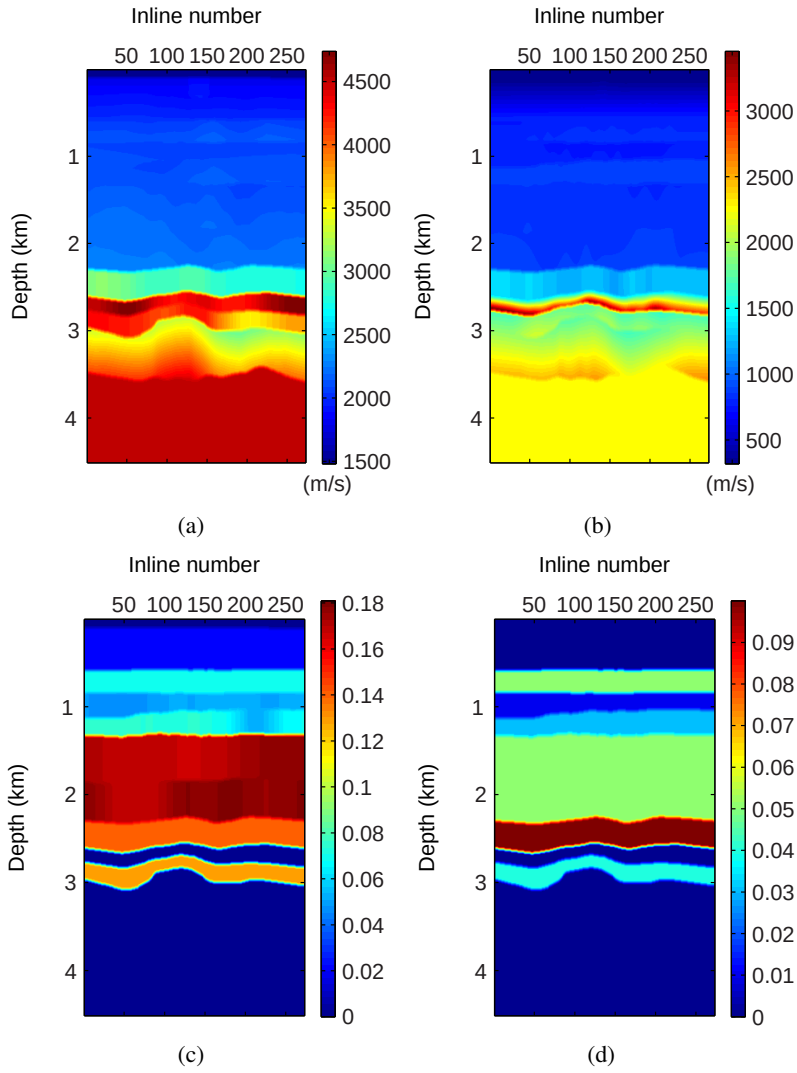

Figure 3.15: Model parameters for the real data example from offshore Norway at crossline 232. (a) Vertical qP-wave velocity α_0; (b) vertical qSV-wave velocity β_0; (c) Thomsen parameter ε; and (d) Thomsen parameter δ.

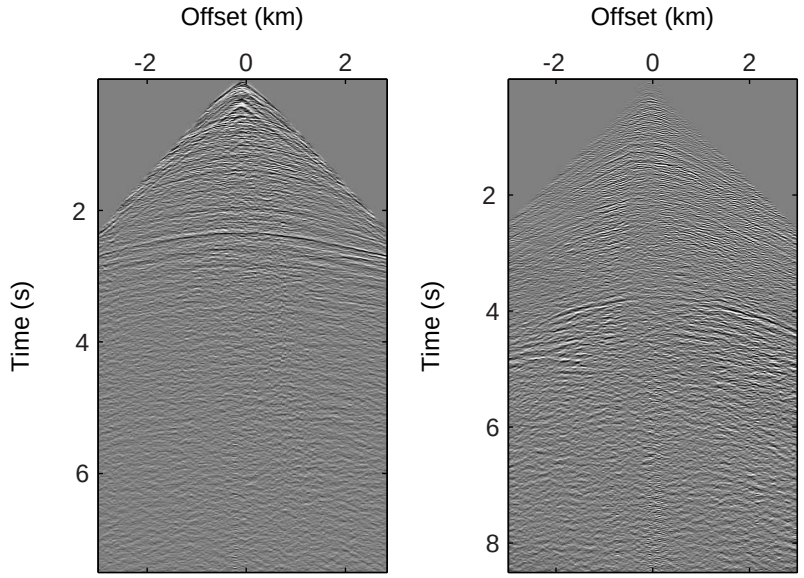

Figure 3.16: Selected shot gathers which are sorted into common-receiver gathers and input to migration for the real data example from offshore Norway. (a) Derived $qP - qP$ shot-gathers and (b) derived $qP - qSV$ shot-gather.

3.9 Conclusions

We have developed a pre-stack migration scheme for compressional and converted waves using one-way propagators. The method builds on an FFD depth extrapolation scheme for which we derive approximations of the vertical qP and qSV slowness as a function of horizontal slowness p. We also derive a qP approximation by using the quasi-acoustic approximation, which can be used in conventional processing where the shear-wave velocity is not known. We notice that the quasi-acoustic approximations provides similar accuracy as the qP approximations. This is expected, since the impact of β_0 on a propagating qP wave is small.

By analyzing the group-velocity as a function of group-angle corresponding to the derived approximations, we show that the approximations used in the compressional and C-wave depth-extrapolation scheme are accurate for high angles using small anisotropy parameters and weak non-hyperbolicity.

Impulse responses demonstrate the accuracy of the derived propagators

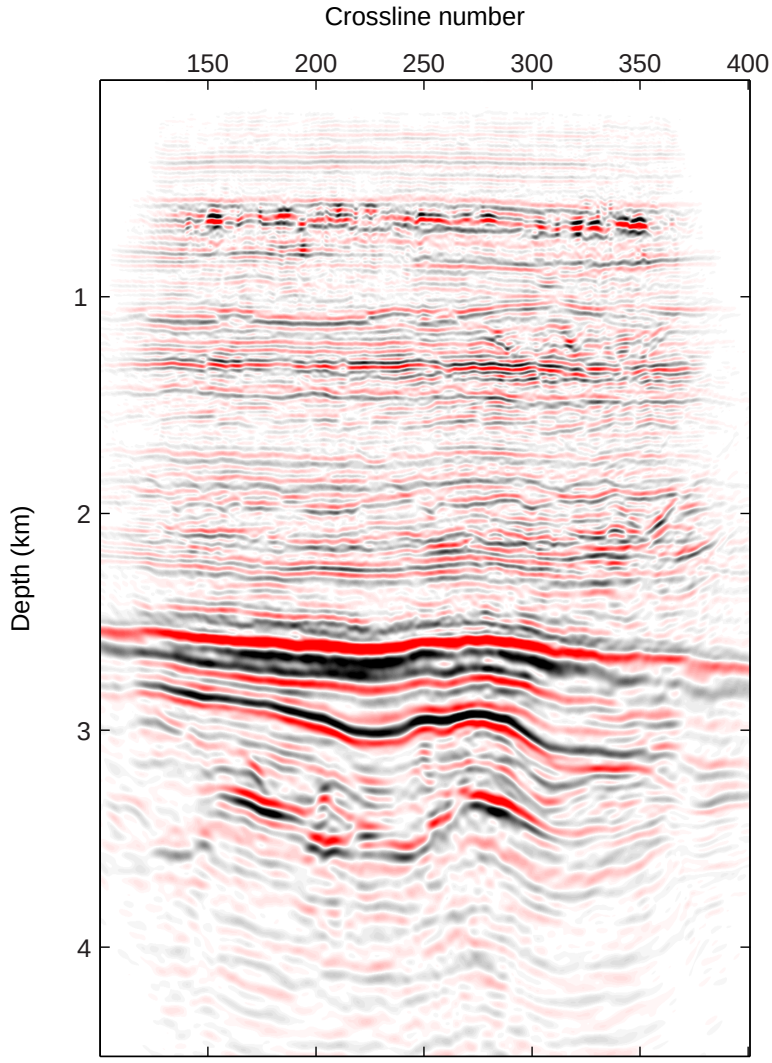

Figure 3.17: Migrated $qP - qP$ section from inline 68 of the real data example from offshore Norway.

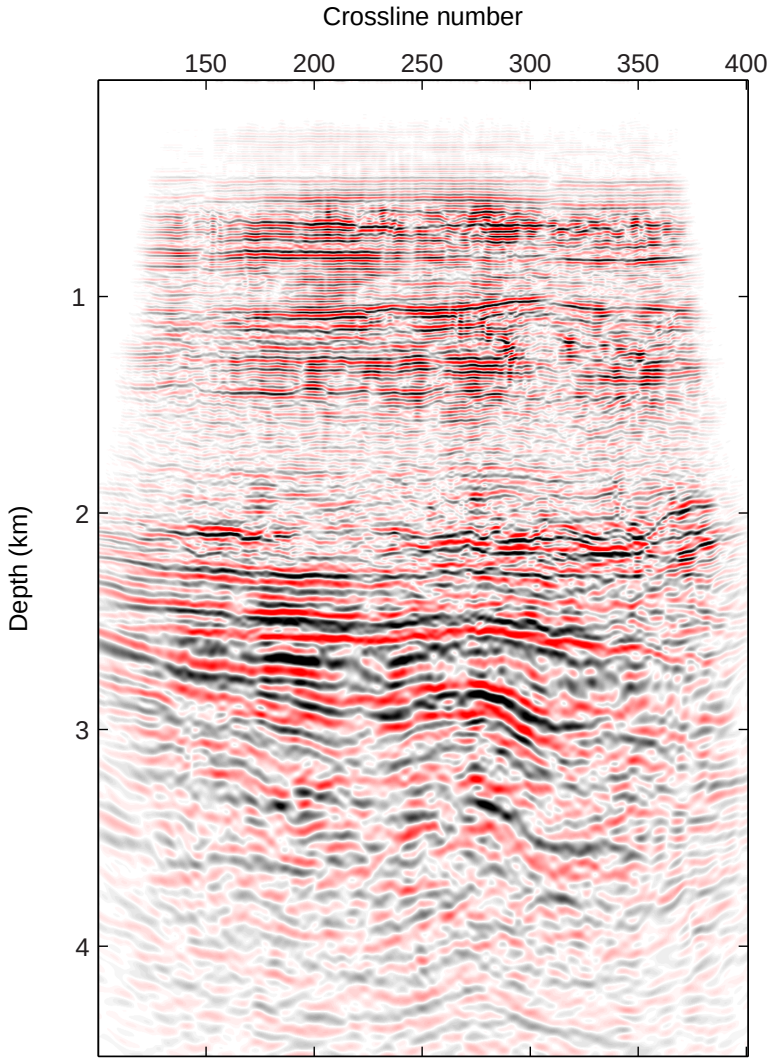

Figure 3.18: Migrated $qP - qSV$ section from inline 68 of the real data example from offshore Norway.

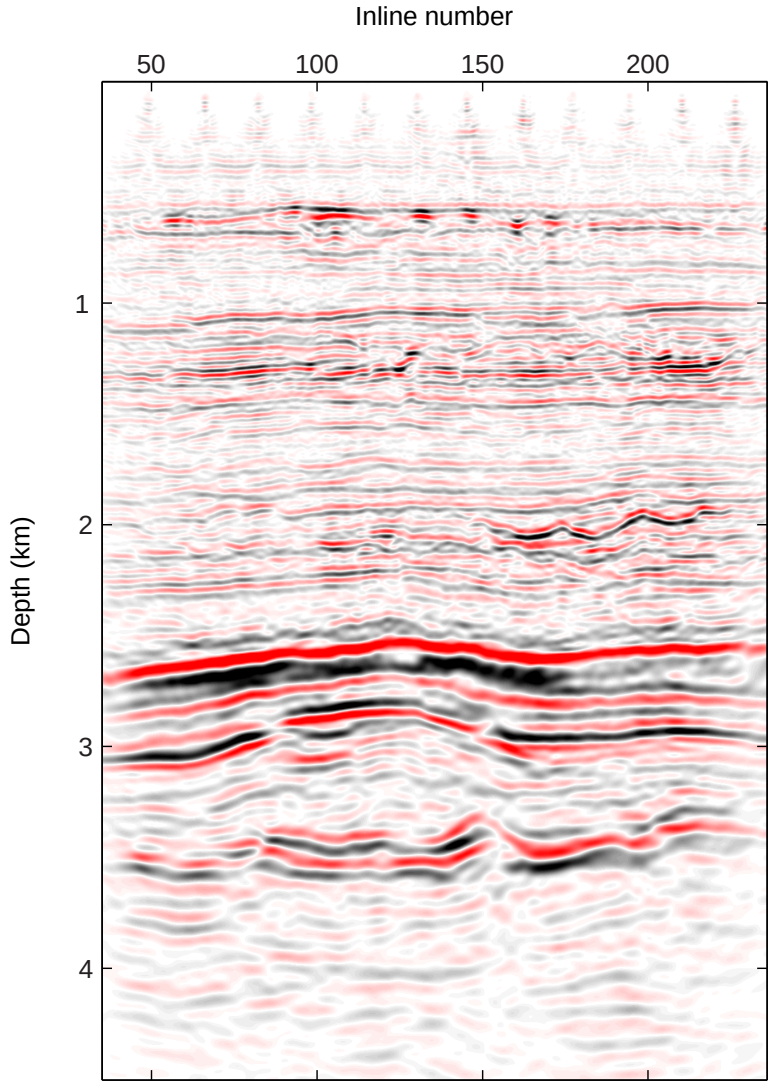

Figure 3.19: Migrated $qP-qP$ section from crossline 232 of the real data example from offshore Norway.

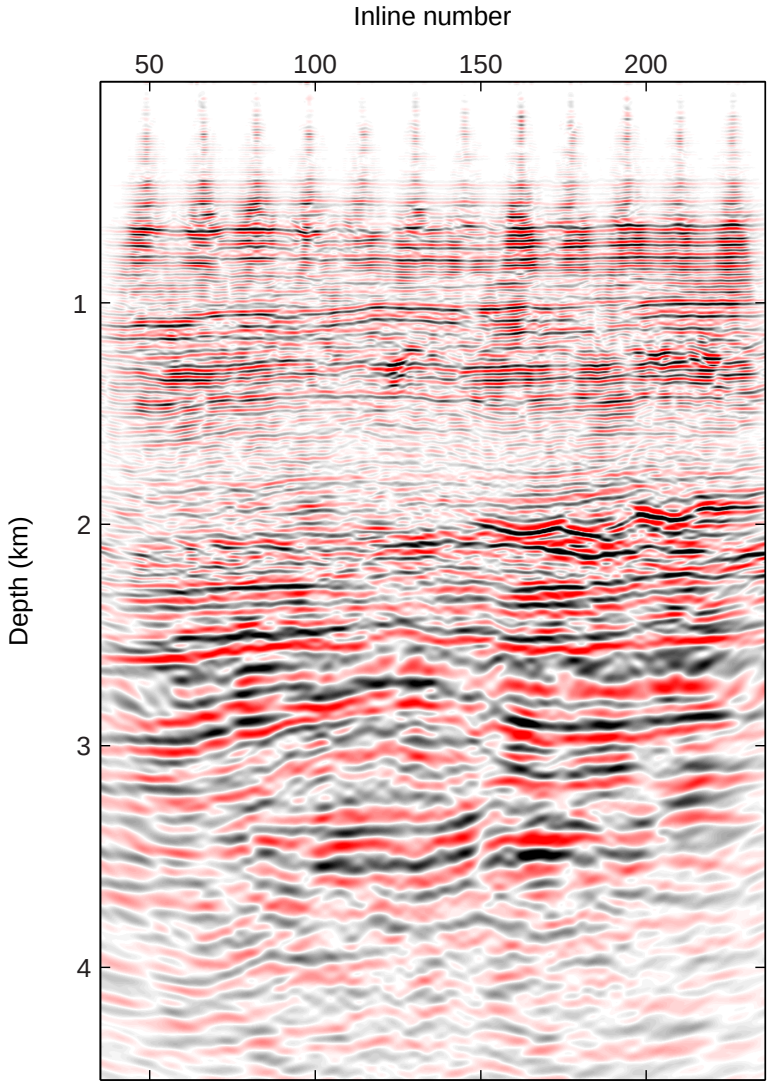

Figure 3.20: Migrated $qP - qSV$ section from crossline 232 of the real data example from offshore Norway.

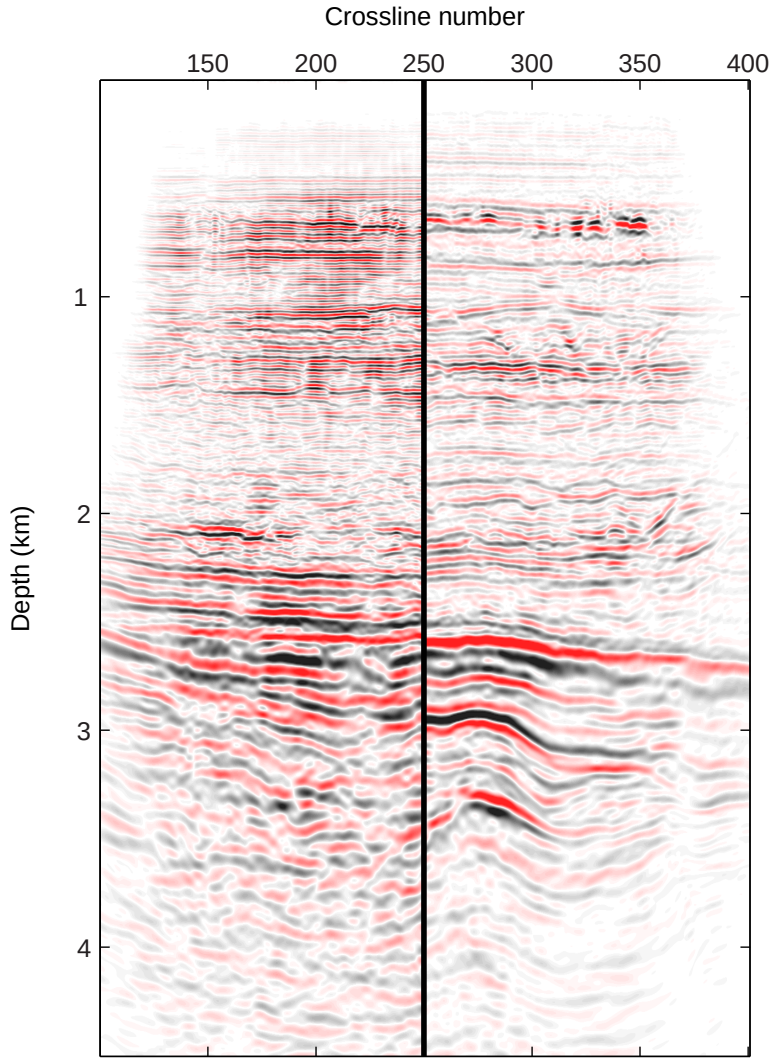

Figure 3.21: Comparison of migrated sections from inline 68 of the real data example from offshore Norway.

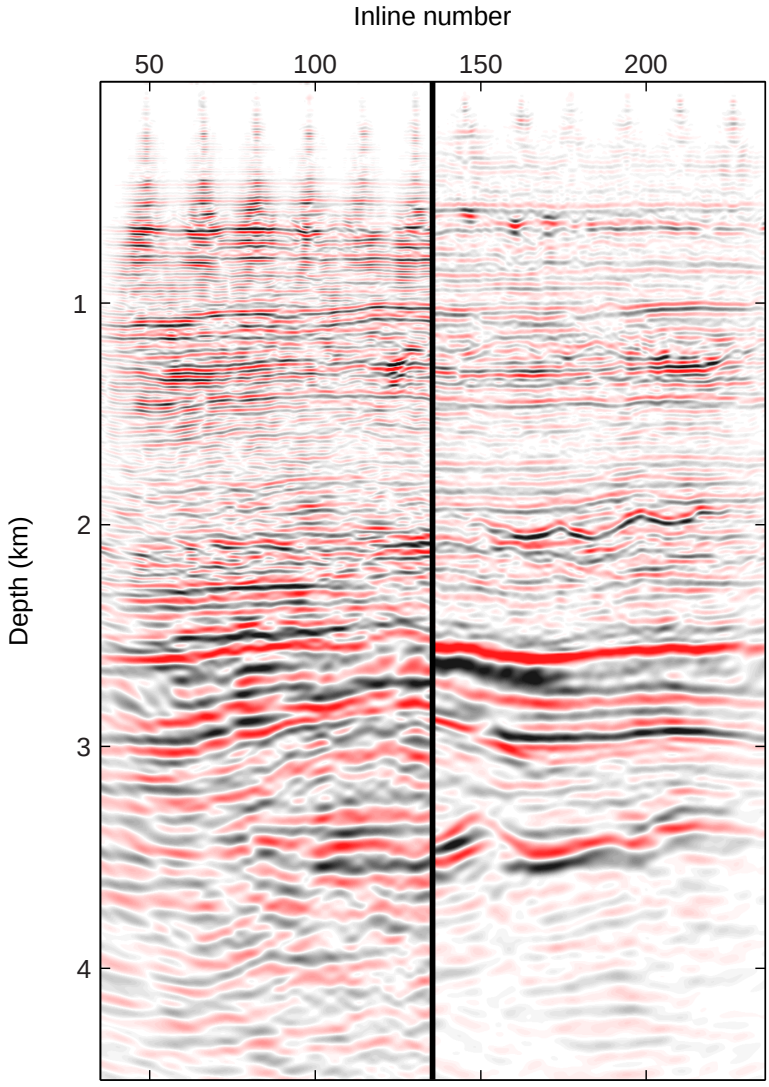

Figure 3.22: Comparison of migrated sections from crossline 232 of the real data example from offshore Norway.

through good dip response and accurate kinematic behavior for weak anisotropy. We show that for higher values of the non-hyperbolicity parameter $(\varepsilon-\delta)/(1+2\delta)$, the accuracy of the compressional propagators are still valid for high angles of propagation, while the C-wave propagators become more inaccurate for higher angles.

The 2D synthetic data example illustrates the methods ability to handle models with a realistic degree of laterally varying medium parameters. The data example also shows consistency between the compressional and C-wave images. The 3D field data example shows that the method is applicable to real data. Even thought the compressional and C-wave images show differences in focusing and structural definitions, we also see good correlation in depth in the images.

3.10 Acknowledgments

This research was supported by the Norwegian Research Council via the ROSE project. We would like to thank Statoil ASA for permission to publish and providing the field dataset. Ørjan Pedersen would like to thank Joachim Mispel for help preparing the field data. Bjørn Ursin has received financial support from Statoil ASA through the VISTA project. Finally, we thank the associate editor Yike Liu, Bertram Nolte and three anonymous reviewers at *Geophysics* for their help in improving this paper.

3.A Finite-difference corrections for one-way thin-slab propagators

Using equation 3.12, we can represent the phase-correcting term Δq_α as

$$\begin{aligned}\Delta q_\alpha &= q_\alpha - q_\alpha^0 \\ &= \frac{1}{\alpha_0}(1-r) - \sum_{j\geq 0}\left(\tilde{a}_j - \tilde{a}_j^0 r^{2j+2}\right)(\alpha_0 p)^{2j+2}\end{aligned} \tag{3.A-1}$$

where

$$r = \alpha_0^0/\alpha_0 \tag{3.A-2}$$

and $\tilde{a}_j^0$ are the coefficients in equations 3.13 defined by the background medium. By cascading Δq_α as given in equation 3.18, we find that

$$\Delta q_\alpha \approx \frac{1}{\alpha_0}(1-r) + \Delta\kappa_2^\alpha p^2 + \frac{\Delta\kappa_1^\alpha p^2}{1-\Delta\kappa_0^\alpha p^2}, \tag{3.A-3}$$

where

$$\begin{aligned}\Delta\kappa_0^\alpha =& \frac{\Delta s_1^2}{\Delta s_2}\alpha_0 \\ \Delta\kappa_1^\alpha =& \frac{\Delta s_2}{\Delta s_1}\alpha_0 \\ \Delta\kappa_2^\alpha =& \left(\Delta s_0 - \frac{\Delta s_1^2}{\Delta s_2}\right)\alpha_0\end{aligned} \tag{3.A-4}$$

and

$$\begin{aligned}\Delta s_0 =& \tilde{a}_0 - \tilde{a}_0^0 r \\ \Delta s_1 =& \tilde{a}_1 - \tilde{a}_1^0 r^3 \\ \Delta s_2 =& \tilde{a}_2 - \tilde{a}_2^0 r^5.\end{aligned} \tag{3.A-5}$$

Similarly, from equation 3.16 we find

$$\begin{aligned}\Delta q_\beta &= q_\beta - q_\beta^0 \\ &= \frac{1}{\beta_0}(1-t) - \sum_{j\geq 0}\left(\tilde{c}_j - \tilde{c}_j^0 t^{2j+2}\right)(\beta_0 p)^{2j+2}\end{aligned} \tag{3.A-6}$$

where

$$t = \beta_0^0/\beta_0 \tag{3.A-7}$$

and $\tilde{c}_j^0$ are the coefficients in equations 3.17 defined by the background medium. By cascading Δq_β as given in equation 3.20, we find that

$$\Delta q_\beta \approx \frac{1}{\beta_0}(1-t) + \Delta\kappa_2^\beta p^2 + \frac{\Delta\kappa_1^\beta p^2}{1-\Delta\kappa_0^\beta p^2}, \tag{3.A-8}$$

where

$$\begin{aligned}\Delta\kappa_0^\beta =& \frac{\Delta u_1^2}{\Delta u_2}\beta_0 \\ \Delta\kappa_1^\beta =& \frac{\Delta u_2}{\Delta u_1}\beta_0^2 \\ \Delta\kappa_2^\beta =& \left(\Delta u_0 - \frac{\Delta u_1^2}{\Delta u_2}\right)\beta_0\end{aligned} \tag{3.A-9}$$

and

$$\begin{aligned}\Delta u_0 =& \tilde{u}_0 - \tilde{u}_0^0 t \\ \Delta u_1 =& \tilde{u}_1 - \tilde{u}_1^0 t^3 \\ \Delta u_2 =& \tilde{u}_2 - \tilde{u}_2^0 t^5.\end{aligned} \tag{3.A-10}$$

Finally, we notice that in the isotropic case, $\zeta = \sigma = 0$ and $\chi = 1$, thus $a_0 = 1$ and $a_1 = a_2 = 0$, hence,

$$\begin{aligned}\tilde{a}_0 &= \frac{1}{2}, \\ \tilde{a}_1 &= \frac{1}{8}, \\ \tilde{a}_2 &= \frac{1}{16}.\end{aligned} \tag{3.A-11}$$

This gives

$$\begin{aligned}\Delta s_0 &= \frac{1}{2}(1-r), \\ \Delta s_1 &= \frac{1}{8}(1-r^3), \\ \Delta s_2 &= \frac{1}{16}(1-r^5).\end{aligned} \tag{3.A-12}$$

Further,

$$\begin{aligned}\Delta\kappa_0^\alpha &= \frac{1}{4}\frac{(1-r^3)^2}{1-r^5}\alpha_0, \\ \Delta\kappa_1^\alpha &= \frac{1}{2}\frac{1-r^5}{1-r^3}\alpha_0^2, \\ \Delta\kappa_2^\alpha &= \left(\frac{1}{2}(1-r) - \frac{1}{4}\frac{(1-r^3)^2}{1-r^5}\right)\alpha_0,\end{aligned} \tag{3.A-13}$$

which is equivalent to the isotropic third-order FFD approximation derived by Ristow and Rühl (1994, their equation A-22).

Chapter 4

Flux-normalized wavefield decomposition and migration of marine seismic data

Ø. Pedersen[1], B. Ursin[1], B. Arntsen[1]

[1]*Department of Petroleum Engineering and Applied Geophysics, NTNU*

Separation of wavefields into directional components can be accomplished by an eigenvalue decomposition of the accompanying system matrix. In conventional pressure-normalized wavefield decomposition, the resulting directional decomposed differential equations contain an interaction between directional components, and depend on the reflectivity function. Usually, the interaction between directional components is disregarded, and by accounting for the reflectivity function, amplitude information is improved. By directional wavefield decomposition using flux-normalized eigenvalue decomposition, it is possible to simplify the resulting system differential equations. Disregarding directional component interaction in the flux-normalized approach provides wavefield separation independent on reflectivity function, and amplitude information is preserved. As a result, reflectivity images with improved amplitude information can be beneficial as indicators of hydrocarbon or in wave-equation migration velocity analysis.

4.1 Introduction

Accurate wavefield traveltimes and amplitudes can be described using two-way wave-equation techniques like finite-difference or finite-element methods. However, these methods can often be significantly more computationally expensive compared to one-way methods. The computational cost in modelling wavefield extrapolation using full wave-equation methods can become a limitation for three-dimensional applications in particular. Ray methods based upon asymptotic theory provide effective alternatives to full wave-equation methods; however, their high-frequency approximations restrict their use in complex subsurface geometry. One-way wavefield methods based upon a paraxial approximation of the wave-equation provide a both computationally cheap and robust alternative approach for solving the wave-equation. With wavefield propagators based on one-way methods, one can increase the speed of computations by several orders of magnitude compared to full wavefield methods.

Representation of a wavefield using the one-way wave-equation permits separation of the wavefield into up- and downgoing constituents. This separation is not valid for near-horizontal propagating waves. Schemes for splitting the wave-equation into up- and downgoing parts and seismic mapping of reflectors are discussed by Claerbout (1971, 1970); however, only the traveltimes are handled correctly.

Several authors have investigated various methods for amplitude correction to one-way wave-equations. Zhang et al. (2003, 2005, 2007) addresses true-amplitude implementation of one-way wave-equations in common-shot migration by modifying the one-way wave-equation. This is accomplished by introducing an auxiliary function that corrects the leading order transport equation for the full wave-equation. Ray theory applied to the modified one-way equations yield up- and downgoing eikonal equations with amplitudes satisfying the transport equation. With full wave-form solutions substituted with corresponding ray-theoretical approximations provides true-amplitude in the sense that the imaging formulas reduce to a Kirchhoff common-shot inversion expression.

Kiyashchenko et al. (2005) develop improved estimation of amplitudes using a multi-one-way approach. It is developed from an iterative solution of the factorized two-way wave-equation with a right-hand side incorporating the medium heterogeneities. It allows for both vertical and horizontal velocity variations and it is demonstrated that the multi-one-way scheme reduce errors in amplitude estimates compared to conventional one-way propagators.

Cao and Wu (2008) reformulate the solution of the one-way wave-equation

in smoothly varying one-dimensional media based on energy-flux conservations. By introducing transparent boundary conditions and transparent propagators, their formulation is extended to a general heterogeneous media in the local angle domain utilizing beamlet methods.

By decomposing the wavefield into up- and downgoing waves with an eigenvalue decomposition using symmetry properties of the accompanying system matrix, one can derive simplified equations for computing the wavefield propagators. This directional decomposition is consistent with a flux-normalization of the wavefield (Ursin, 1983). Further, by neglecting coupling terms between the up- and downgoing waves, the resulting system matrix can be used as a starting point to derive paraxial approximations of the original wave-equation. They can also be used to derive WKBJ approximations of various orders (Bremmer, 1951; van Stralen et al., 1998).

In this paper, we derive initial conditions and one-way propagators for flux-normalized wavefield extrapolation in 1D media and show how this provides accurate amplitude information. We formulate an unbiased estimate of the reflectivity using the wave-equation angle transform. Further, we propose an extension to a general heterogeneous media by defining a laterally invariant background media in which the flux-normalization and an approximation to the transmission loss is performed. We account for the medium perturbations in the downward propagation using Fourier finite-difference methods (Ristow and Rühl, 1994).

We apply both conventional pressure-normalized and the derived flux-normalized wavefield decomposition and propagation to a field data example from offshore Norway. Using this example, we compare and quantify the estimated reflectivity differences.

4.2 Laterally homogeneous medium

We consider acoustic waves travelling in a three-dimensional medium where the principal direction of propagation is taken along the x_3 axis (or "depth"), and the transverse axes are (x_1, x_2). The acoustic medium parameters are assumed to be functions of depth x_3 only. Let c denote the propagation velocity; $\mathbf{v} = (v_1, v_2, v_3)$ the displacement velocity vector; p the pressure; and ρ the density of the medium. With no external volume force acting on the medium, the acoustic wavefield satisfies the constitutive relation given by (Pierce, 1981) (equation 1-5.3)

$$-\nabla p = \rho \partial_t \mathbf{v}, \tag{4.1}$$

and the equation of motion given by

$$\frac{1}{c^2}\partial_t p + \rho \nabla \cdot \mathbf{v} = 0, \tag{4.2}$$

where $\nabla = (\partial_1, \partial_2, \partial_3)$ and ∂_t denotes the partial derivative with respect to time t.

We define the Fourier transform with respect to time t and the transverse spatial directions (x_1, x_2) as

$$P(\omega, k_1, k_2, x_3) = \iiint_{-\infty}^{\infty} p(t, x_1, x_2, x_3)\, \mathrm{e}^{\mathrm{i}(\omega t - k_1 x_1 - k_2 x_2)} \mathrm{d}x_1 \mathrm{d}x_2 \mathrm{d}t, \tag{4.3}$$

with the inverse transform with respect to circular frequency ω and the transverse wave-numbers (k_1, k_2) as

$$p(t, x_1, x_2, x_3) = \frac{1}{(2\pi)^3} \iiint_{-\infty}^{\infty} P(\omega, k_1, k_2, x_3)\, \mathrm{e}^{\mathrm{i}(-\omega t + k_1 x_1 + k_2 x_2)} \mathrm{d}k_1 \mathrm{d}k_2 \mathrm{d}\omega. \tag{4.4}$$

Applying the Fourier transform to equations 4.1 and 4.2, the resulting reduced linear acoustic system of equations in a horizontally homogeneous fluid yield the matrix differential equation

$$\partial_3 \mathbf{b} = \mathrm{i}\omega \mathbf{A} \mathbf{b}, \tag{4.5}$$

where the system matrix $\mathbf{A}$ is given by

$$\mathbf{A} = \begin{bmatrix} 0 & \rho \\ \frac{1}{\rho}\left(\frac{1}{c^2} - \frac{k_1^2 + k_2^2}{\omega^2}\right) & 0 \end{bmatrix}, \tag{4.6}$$

and the field vector $\mathbf{b}$ by

$$\mathbf{b} = \begin{bmatrix} P \\ V_3 \end{bmatrix}, \tag{4.7}$$

where P is the Fourier transformation of p and V_3 is the Fourier transformation of v_3 with respect to t, x_1 and x_2.

The measured field vector $\mathbf{b} = [P, V_3]^T$ can be separated into up- and downgoing waves, denoted U and D, respectively. This separation is accomplished by applying an inverse eigenvector matrix of $\mathbf{A}$, denoted $\mathbf{L^{-1}}$, on $\mathbf{b}$. We define the transformed field vector containing the directional decomposed wavefield by

$$\mathbf{w} = \begin{bmatrix} U \\ D \end{bmatrix} = \mathbf{L}^{-1}\, \mathbf{b}. \tag{4.8}$$

Moreover, upon substitution of $\mathbf{w}$, the matrix differential equation 4.5 transforms to

$$\partial_3 \mathbf{w} = \left(\mathrm{i}\omega \mathbf{\Lambda} - \mathbf{L}^{-1} \partial_3 \mathbf{L} \right) \mathbf{w}, \tag{4.9}$$

where an eigenvalue decomposition of $\mathbf{A}$ provides the diagonal eigenvalue matrix $\mathbf{\Lambda} = \mathbf{L}^{-1} \mathbf{A}\, \mathbf{L}$.

The vertical wave-number k_3 is

$$k_3 = \begin{cases} \sqrt{\left(\frac{\omega}{c}\right)^2 - \left(k_1^2 + k_2^2\right)}, & \text{if } \sqrt{k_1^2 + k_2^2} \leq |\frac{\omega}{c}| \\ \mathrm{i}\sqrt{k_1^2 + k_2^2 - (\frac{\omega}{c})^2}, & \text{if } \sqrt{k_1^2 + k_2^2} > |\frac{\omega}{c}| \end{cases}. \tag{4.10}$$

We consider a plane wave with wavenumber $\mathbf{k} = (k_1, k_2, k_3)^T$ and direction $\mathbf{m} = (\sin\theta\cos\phi, \sin\theta\sin\phi, \cos\theta)^T$ where θ is dip angle and ϕ is azimuth. We have

$$\mathbf{k} = \frac{\mathbf{m}\omega}{c} = \omega \mathbf{p}, \tag{4.11}$$

where $\mathbf{p}$ is the slowness vector. In our further development, it is convenient to introduce the impedance Z:

$$Z = \frac{\rho\omega}{k_3} = \frac{\rho}{p_3} = \frac{\rho c}{\cos\theta}. \tag{4.12}$$

4.2.1 Amplitude-normalized wavefields

In the conventional pressure-normalized wavefield separation approach, one choose the eigenvector matrix of $\mathbf{A}$ as (Claerbout, 1976; Ursin, 1984, 1987)

$$\mathbf{L} = \begin{bmatrix} 1 & 1 \\ -\frac{1}{Z} & \frac{1}{Z} \end{bmatrix}. \tag{4.13}$$

This leads to the inverse eigenvector matrix

$$\mathbf{L}^{-1} = \frac{1}{2} \begin{bmatrix} 1 & -Z \\ 1 & Z \end{bmatrix}. \tag{4.14}$$

With the eigenvector matrix defined in equation 4.13, the matrix differential equation 4.9 becomes

$$\partial_3 \mathbf{w} = \mathrm{i}\omega \begin{bmatrix} -p_3 & 0 \\ 0 & p_3 \end{bmatrix} \mathbf{w} - \gamma\left(x_3\right) \begin{bmatrix} -1 & 1 \\ 1 & -1 \end{bmatrix} \mathbf{w}, \tag{4.15}$$

where

$$\gamma\left(x_3\right) = \frac{1}{2}\partial_3 \log Z\left(x_3\right) \tag{4.16}$$

is the reflectivity function. Using equation 4.12 it can be expressed as

$$\gamma(x_3) = \frac{1}{2}\left[\frac{1}{\rho}\frac{\partial \rho}{\partial x_3} + \frac{1}{\cos^2\theta}\frac{1}{c}\frac{\partial c}{\partial x_3}\right]. \tag{4.17}$$

The wavefield decomposition described in equation 4.15 is referred to as being pressure-normalized in the sense that the pressure field equals the sum of the up- and downgoing wavefield.

We consider a stack of inhomogeneous layers where ρ and c are continuous functions of x_3 within each layer. At an interface between two layers, the boundary condition requires that the wave vector $\mathbf{b}$ shall be continuous. For an interface at $x_3 = x_{3_k}$ we must have $L_+\mathbf{w}_+ = L_-\mathbf{w}_-$ where $L_- = L(x_{3_{k-}})$ is evaluated above the interface, and $L_+ = L(x_{3_{k+}})$ is evaluated beneath the interface (the x_3-axis is pointing vertically downwards). We therefore have

$$\mathbf{w}_+ = L_+^{-1}L_-\mathbf{w}_-. \tag{4.18}$$

Equation 4.13 and 4.14 give

$$L_+^{-1}L_- = \frac{1}{2}\begin{bmatrix} 1+\frac{Z_+}{Z_-} & 1-\frac{Z_+}{Z_-} \\ 1-\frac{Z_+}{Z_-} & 1+\frac{Z_+}{Z_-} \end{bmatrix}. \tag{4.19}$$

This can be written as (Ursin, 1983, equation 33):

$$L_+^{-1}L_- = \frac{1}{2}\begin{bmatrix} T_u^{-1} & R_uT_u^{-1} \\ R_uT_u^{-1} & T_u^{-1} \end{bmatrix}, \tag{4.20}$$

where T_u and R_u are the transmission and reflection coefficients for an upward travelling incident wave at the interface.

4.2.2 Flux-normalized wavefields

We now derive an alternative directional decomposition by a flux-normalization of the wavefield. The main advantage of flux-normalizing the wavefield is that we obtain simpler expression of the corresponding directional decomposed matrix differential equation, as compared to the pressure-normalized approach. Disregarding the interaction between directional components yields a matrix differential equation independent of the reflectivity function.

In order obtain a flux-normalized system of equations, we choose the eigenvector matrix of $\mathbf{A}$ as (Ursin, 1983; Wapenaar, 1998)

$$\tilde{\mathbf{L}} = \frac{1}{\sqrt{2}} \begin{bmatrix} \sqrt{Z} & \sqrt{Z} \\ -\frac{1}{\sqrt{Z}} & \frac{1}{\sqrt{Z}} \end{bmatrix}, \tag{4.21}$$

and thus the inverse eigenvector matrix becomes

$$\tilde{\mathbf{L}}^{-1} = \frac{1}{\sqrt{2}} \begin{bmatrix} \frac{1}{\sqrt{Z}} & -\sqrt{Z} \\ \frac{1}{\sqrt{Z}} & \sqrt{Z} \end{bmatrix}. \tag{4.22}$$

This provides a flux-normalized representation of the wavefield

$$\tilde{\mathbf{w}} = \tilde{\mathbf{L}}^{-1}\, \mathbf{b}, \tag{4.23}$$

where $\tilde{\mathbf{w}} = (\tilde{U}, \tilde{D})^T$, and where $\tilde{U}$ and $\tilde{D}$ denote the flux-normalized directional components of the wavefield. The wavefield is referred to as flux-normalized in the sense that the energy flux in the x_3-direction is propagation invariant (Ursin, 1983; Wapenaar, 1998).

Both the pressure-normalized and the flux-normalized decomposition break down for near horizontally travelling waves since the lateral wave-number k_3 approaches 0 in the horizontal direction.

Combining equations 4.21 and 4.23 with equation 4.9 yield the transformed matrix differential equation

$$\partial_3 \tilde{\mathbf{w}} = \mathrm{i}\omega \begin{bmatrix} -p_3 & 0 \\ 0 & p_3 \end{bmatrix} \tilde{\mathbf{w}} - \gamma\,(x_3) \begin{bmatrix} 0 & 1 \\ 1 & 0 \end{bmatrix} \tilde{\mathbf{w}}. \tag{4.24}$$

Comparing the flux-normalized system of equations in equation 4.24 with the conventional pressure-normalized system of equations in equation 4.15, we see that in equation 4.24 only the off-diagonal terms (depending on the reflectivity function $\gamma(x_3)$) are present. Further, by neglecting interaction between the flux-normalized directional decomposed components, the flux-normalized matrix differential equation becomes independent of the reflectivity function $\gamma(x_3)$. Finally, we note that

$$\begin{aligned} \tilde{\mathbf{w}}(\omega, k_1, k_2, x_3) &= \sqrt{\frac{2}{Z}}\mathbf{w}(\omega, k_1, k_2, x_3) \\ &= \sqrt{\frac{2k_3}{\rho\omega}}\mathbf{w}(\omega, k_1, k_2, x_3). \end{aligned} \tag{4.25}$$

At an interface between two smoothly varying media we have $\tilde{\mathbf{w}}_+ = \tilde{L}_+^{-1}\tilde{L}_-\tilde{\mathbf{w}}_-$ with

$$\tilde{L}_+^{-1}\tilde{L}_- = \begin{bmatrix} \tilde{T}_u^{-1} & R_u\tilde{T}_u^{-1} \\ R_u\tilde{T}_u^{-1} & \tilde{T}_u^{-1} \end{bmatrix} \tag{4.26}$$

Here,

$$\tilde{T}_u^{-1} = \sqrt{\frac{Z_-}{Z_+}}T_u^{-1} = \frac{Z_+ + Z_-}{2\sqrt{Z_+Z_-}} = \frac{1}{2}\left\{\sqrt{\frac{Z_+}{Z_-}} + \sqrt{\frac{Z_-}{Z_+}}\right\}, \tag{4.27}$$

where Z_- denotes the impedance at the bottom of the previous thin layer and Z_+ denotes the impedance at the top of the next layer.

Zhang et al. (2005) in their equations 27 and 28 use the scaling $\tilde{\mathbf{w}} = \sqrt{k_3}\mathbf{w}$ so they are not using flux-normalized variables. With their scaling, the transformed matrix differential equation will only be of the form of equation 4.24 for a medium with constant density.

4.3 One-way wave-equations

We shall obtain one-way equations for the up- and downgoing waves by neglecting the interaction terms in equations 4.15 and 4.20. This gives the zero-order WKBJ approximation (Clayton and Stolt, 1981; Ursin, 1984) obeying the equations

$$\frac{\partial}{\partial x_3}\begin{bmatrix} U \\ D \end{bmatrix} = \begin{bmatrix} -\mathrm{i}k_3 + \gamma & 0 \\ 0 & \mathrm{i}k_3 + \gamma \end{bmatrix}\begin{bmatrix} U \\ D \end{bmatrix} \tag{4.28}$$

with interface conditions

$$\begin{bmatrix} U \\ D \end{bmatrix}_+ = T_u^{-1}\begin{bmatrix} U \\ D \end{bmatrix}_- . \tag{4.29}$$

In a region with smoothly varying parameters, the equation

$$\frac{\partial D}{\partial x_3} = (\mathrm{i}k_3 + \gamma)\, D \tag{4.30}$$

with $D(x_3^0)$ given, has the solution

$$\begin{aligned} D(x_3) =& D(x_3^0)\exp\left[\int_{x_3^0}^{x_3}(\mathrm{i}k_3(\zeta) + \gamma(\zeta))\,\mathrm{d}\zeta\right] \\ =& D(x_3^0)\sqrt{\frac{Z(x_3)}{Z(x_3^0)}}\exp\left[\int_{x_3^0}^{x_3}(\mathrm{i}k_3(\zeta))\,\mathrm{d}\zeta\right]. \end{aligned} \tag{4.31}$$

The solution to equations 4.28 and 4.29 in the zero-order WKB approximation becomes

$$D(x_3) = D(x_3^0)T(x_3)\exp\left[\mathrm{i}\int_{x_3^0}^{x_3} k_3(\zeta)\mathrm{d}\zeta\right] \tag{4.32}$$

and

$$U(x_3) = U(x_3^0)T(x_3)\exp\left[-\mathrm{i}\int_{x_3^0}^{x_3} k_3(\zeta)\mathrm{d}\zeta\right]. \tag{4.33}$$

The factor

$$\begin{aligned} T(x_3) &= \sqrt{\frac{Z(x_3)}{Z(x_3^0)}} \prod_{0<x_{3_k}<x_3} T_u^{-1}(x_{3_k}) \sqrt{\frac{Z(x_{3_{k-}})}{Z(x_{3_{k+}})}} \\ &= \sqrt{\frac{Z(x_3)}{Z(x_3^0)}} \prod_{0<x_{3_k}<x_3} \tilde{T}_u^{-1}(x_{3_k}) \end{aligned} \tag{4.34}$$

is due to the interfaces between the inhomogeneous layers.

For the flux-normalized up- and downgoing waves we obtain from equations 4.32 to 4.34 using equation 4.25:

$$\tilde{D}(x_3) = \tilde{D}(x_{3_0}) \prod_{0<x_{3_k}<x_3} \tilde{T}_u^{-1}(x_{3_k}) \exp\left[\int_{x_3^0}^{x_3} \mathrm{i}k_3(\zeta)\mathrm{d}\zeta\right] \tag{4.35}$$

and

$$\tilde{U}(x_3) = \tilde{U}(x_3^0) \prod_{0<x_{3_k}<x_3} \tilde{T}_u^{-1}(x_{3_k}) \exp\left[-\int_{x_3^0}^{x_3} \mathrm{i}k_3(\zeta)\mathrm{d}\zeta\right]. \tag{4.36}$$

These equations could, of course, also have been obtained directly by neglecting the interaction terms in equation 4.24 and 4.26.

4.4 Imaging conditions

In order to investigate the amplitude versus angle (AVA) or amplitude versus slowness (AVP) behavior of imaging with the different wavefield separation methods, we shall consider the simple case of a point source at a distance x_3 above a plane reflector. See Figure 4.1.

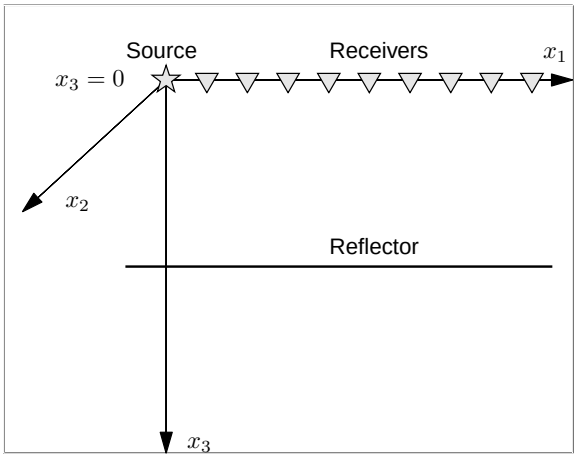

Figure 4.1: Simple geometry for imaging conditions.

The initial downgoing wavefield is

$$D_0 = D(\omega, k_1, k_2, x_3 = 0) = -\frac{2\pi S(\omega)}{\mathrm{i}\omega k_3}. \tag{4.37}$$

The inverse Fourier transform of equation 4.37 with respect to k_1 and k_2 is known as the Weyl integral (Aki and Richards, 1980). $S(\omega)$ is the Fourier transform of the effective source signature. The reflected wavefield is recorded at the same level as the source, and it is given by (suppressing the function arguments)

$$\begin{aligned} U_0 &= U(\omega, k_1, k_2, x_3 = 0) \\ &= D_0 \exp\left[\mathrm{i}k_3 x_3\right] R(p_1, p_2) \exp\left[\mathrm{i}k_3 x_3\right], \end{aligned} \tag{4.38}$$

where $R(p_1, p_2)$ is the reflection coefficient at depth x_3. It depends only on the horizontal slowness (see Appendix 4.A)

$$p = \sqrt{p_1^2 + p_2^2}. \tag{4.39}$$

With amplitude-normalized separation of the up- and downgoing wavefields, wavefield extrapolation gives, at depth x_3,

$$\begin{aligned} D &= D_0 \exp\left[\mathrm{i}k_3 x_3\right] \\ U &= U_0 \exp\left[-\mathrm{i}k_3 x_3\right]. \end{aligned} \tag{4.40}$$

Imaging, or estimation of the reflection coefficient, is performed by cross-correlation in the wavenumber domain at depth x_3. This gives for amplitude-normalized variables

$$\begin{aligned} I_A(p_1,p_2) &= \int U D^* \mathrm{d}\omega \\ &= R(p_1,p_2)\int |D_0|^2 \,\mathrm{d}\omega \\ &= R(p_1,p_2)\frac{F(\omega)}{p_3^2}, \end{aligned} \tag{4.41}$$

where

$$F(\omega) = \left|\frac{2\pi S(\omega)}{\omega}\right|^2. \tag{4.42}$$

For flux-normalized variables, $\tilde{\mathbf{w}} = \sqrt{\frac{2p_3}{\rho}}\mathbf{w}$ we obtain

$$\begin{aligned} I_F(p_1,p_2) &= \int \tilde{U}\tilde{D}^* \mathrm{d}\omega \\ &= R(p_1,p_2)\int \left|\tilde{D}_0\right|^2 \mathrm{d}\omega \\ &= R(p_1,p_2)\frac{2F(\omega)}{\rho p_3}. \end{aligned} \tag{4.43}$$

Sun and Zhang (2008) have proposed a migration scheme where the initial conditions for the downward continued wavefield is

$$\bar{D}_0 = -\frac{S(\omega)}{\mathrm{i}\omega}. \tag{4.44}$$

This gives the cross-correlation image

$$\begin{aligned} I_Z(p_1,p_2) &= \int U \bar{D}_0^* \mathrm{d}\omega \\ &= R(p_1,p_2)\int D_0 \bar{D}_0^* \mathrm{d}\omega \\ &= R(p_1,p_2)\frac{F(\omega)}{2\pi p_3}. \end{aligned} \tag{4.45}$$

Since $p_3 = \cos(\theta)/c$ it is seen that the first cross-correlation in equation 4.41 is divided by $\cos^2(\theta)$, while the two last in equations 4.43 and 4.45 only are

divided by $\cos(\theta)$. It is customary to estimate the AVA response by multiplying an AVA response obtained from a cross-correlation image condition with $\cos(\theta)$. Then only the two last cross-correlations will give correct AVA behavior. This confirms what previously has been found by Zhang et al. (2005) and Sun and Zhang (2008). Multiplying the cross-correlation AVA response with $\cos(\theta)$ gives incorrect result for the amplitude-normalized wavefields, but the one of new initial data give correct result.

We note that in this simple example, the two first methods give correct result by computing

$$\begin{aligned} R(p_1, p_2) &= \frac{\int U D^* \mathrm{d}\omega}{\int |D_0|^2 \, \mathrm{d}\omega} \\ &= \frac{\int \tilde{U} \tilde{D}^* \mathrm{d}\omega}{\int \left|\tilde{D}_0\right|^2 \mathrm{d}\omega}. \end{aligned} \tag{4.46}$$

In the last method, some care must be used since

$$R(p_1, p_2) = \frac{\int U \bar{D}^* \mathrm{d}\omega}{\int D_0 \bar{D}_0^* \mathrm{d}\omega}. \tag{4.47}$$

4.5 Heterogeneous medium

We want to use one-way wave propagators for migration in a heterogeneous medium. Based on the previous discussion we choose to use flux-normalized variables. The downgoing field from a point source is then represented in the wavenumber-frequency domain by

$$\tilde{D}_0(\omega, k_1, k_2, 0) = 2\pi \mathrm{i} \sqrt{\frac{2}{\rho \omega k_3}} S(\omega). \tag{4.48}$$

In marine seismic data we may add the effect of the free surface (the ghost) on the downgoing wavefield (Amundsen and Ursin, 1991):

$$\begin{aligned} \tilde{D}_0(\omega, k_1, k_2, 0) &= 2\pi \mathrm{i} \sqrt{\frac{2}{\rho \omega k_3}} \\ &\times \left(\exp\left[-\mathrm{i} k_3 x_3^s\right] - R_0 \exp\left[\mathrm{i} k_3 x_3^s\right]\right) S(\omega), \end{aligned} \tag{4.49}$$

where x_3^s is the source depth, and the reflection coefficient is theoretically $R_0 = 1$.

If the wavefield is acquired by a conventional streamer configuration, only pressure is recorded. The primary upgoing wavefield U can then be estimated by

a demultiple procedure (Robertsson and Kragh, 2002; Amundsen, 2001), where ghost and free-surface multiples are removed from the data. Hence, using equation 4.25 the flux-normalized upgoing wavefield can be represented by

$$\tilde{U}_0 = \sqrt{\frac{2}{Z}} U_0. \tag{4.50}$$

The pressure and the vertical displacement velocity can be measured in ocean-bottom seismic acquisition. Recent development (Tenghamn et al., 2008; Landrø and Amundsen, 2007) also allows for both these to be measured on a streamer configuration. Then the flux-normalized upgoing wavefield is given by

$$\tilde{U}_0 = \frac{1}{\sqrt{2Z}} \left[P - Z V_3 \right]. \tag{4.51}$$

The downward continuation of the wavefields is done by solving the equation

$$\frac{\partial \tilde{\mathbf{w}}}{\partial x_3} = \begin{bmatrix} -\mathrm{i}\hat{H}_1 & 0 \\ 0 & \mathrm{i}\hat{H}_1 \end{bmatrix} \tilde{\mathbf{w}} \tag{4.52}$$

for $x_3 > 0$ with $\tilde{\mathbf{w}}(0) = \left[\tilde{U}_0, \tilde{D}_0 \right]^T$ given in equation 4.49 - 4.51. Equation 4.52 is a generalization of equation 4.24 with the coupling terms neglected. The operator $\hat{H}_1$ is the square-root operator satisfying (Wapenaar, 1998)

$$\hat{H}_1 \hat{H}_1 = \left(\frac{\omega}{c} \right)^2 + \rho \frac{\partial}{\partial x_1} \left(\frac{1}{\rho} \frac{\partial}{\partial x_1} \cdot \right) + \rho \frac{\partial}{\partial x_2} \left(\frac{1}{\rho} \frac{\partial}{\partial x_2} \cdot \right). \tag{4.53}$$

By dividing the medium into thin slabs of thickness Δx_3 with negligible variations in the preferred direction x_3 of propagation within each slab, allows us to extend the propagator to a general inhomogeneous medium with small lateral medium variations using for example split-step (Stoffa et al., 1990), Fourier finite difference (Ristow and Rühl, 1994), or a phase-screen (Wu and Huang, 1992) approach depending on the size of the medium heterogeneities in the lateral direction (Zhang et al., 2009).

At thin-slab boundaries one may apply a correction term for the transmission loss (see Appendix 4.B):

$$\tilde{T}_u^{-1} = \frac{1}{2} \left[\sqrt{\frac{Z_+}{Z_-}} + \sqrt{\frac{Z_-}{Z_+}} \right]. \tag{4.54}$$

Cao and Wu (2006) have proposed a similar correction for the downward continuation of pressure.

The downward continued wavefields can be used in a standard way to create an image. One may also apply a cross-correlation and a local Fourier transform to compute common-angle gathers (de Bruin et al., 1990; Sava and Fomel, 2003; de Hoop et al., 2006; Sun and Zhang, 2008). This is termed the wave-equation angle transform, and a common-image gather for a single shot is

$$I(\mathbf{x},\mathbf{p}) = \frac{1}{2\pi}\iint U\left(\mathbf{x}+\frac{\mathbf{h}}{2},\omega\right) D^*\left(\mathbf{x}-\frac{\mathbf{h}}{2},\omega\right) \mathrm{e}^{-\mathrm{i}\omega\mathbf{p}\cdot\mathbf{h}}\mathrm{d}\mathbf{h}\mathrm{d}\omega, \qquad (4.55)$$

where $\mathbf{h} = (h_1, h_2, 0)$ is the horizontal offset coordinate and $\mathbf{p}\cdot\mathbf{h} = p_1h_1 + p_2h_2$. In Appendix 4.A it is shown that this approach produces an estimate of the plane-wave reflection coefficient multiplied by the energy of the corresponding downgoing plane wave. In order to obtain an unbiased estimate of the reflection coefficient it is necessary to divide by this factor (which we will refer to as the *source correction term*), exactly as in equation 4.46. This gives the estimate

$$R_{AT}(\mathbf{x},\mathbf{p}) = \frac{1}{2\pi}\frac{\iint U\left(\mathbf{x}+\frac{\mathbf{h}}{2},\omega\right) D^*\left(\mathbf{x}-\frac{\mathbf{h}}{2},\omega\right) \mathrm{e}^{-\mathrm{i}\omega\mathbf{p}\cdot\mathbf{h}}\mathrm{d}\mathbf{h}\mathrm{d}\omega}{\int |\hat{D}(\mathbf{x},\omega\mathbf{p},\omega)|^2\mathrm{d}\omega}. \qquad (4.56)$$

It may be necessary to apply a stabilizing procedure as discussed in Vivas et al. (2009). In order to obtain an estimate of the reflection coefficient for a range of p-values it is necessary to average the expression in equation 4.56 over many shots.

4.6 Numerical results

Throughout our numerical examples, we employ a Fourier finite-difference approach to account for lateral medium variations. Further, we consider wave-propagation in a 2D medium.

First we extract amplitude information after migration using flux-normalized wavefields in a lateral invariant medium. The input data to migration is modelled over a medium with density contrasts only; hence, the reflection coefficients are independent of angle. Next, we compare conventional pressure normalization to the flux-normalized approach on a field data example where we in a quantitative fashion compare the estimated reflectivity. For the flux-normalized approach we use equations 4.35 and 4.36 combined with equation 4.A-6 for the wave propagation. For the pressure-normalized approach, we use equations 4.32 and 4.33 and set the transmission correction to unity. Equation 4.56 is used to output AVP gathers on selected locations.

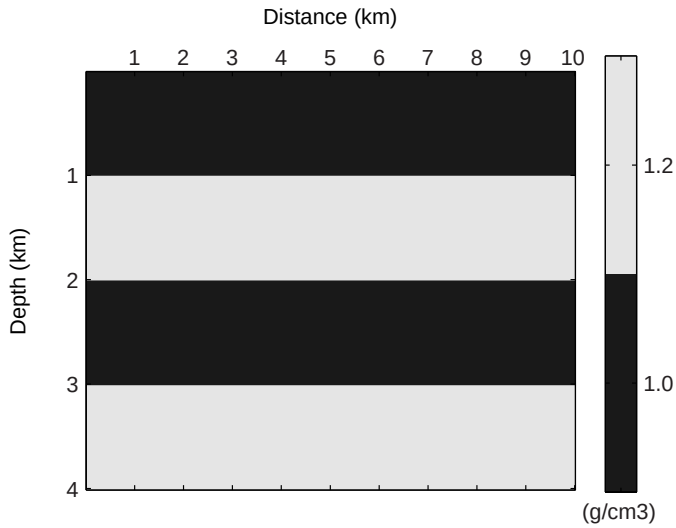

Figure 4.2: Densities used in the finite-difference modelling over the lateral invariant model example.

4.6.1 Imaging in a lateral invariant medium

In our first test, we consider a laterally invariant medium with a constant velocity of 2000 m/s and with density contrasts in depth at 1, 2, and 3 km as illustrated in Figure 4.2. We choose this model since in this particular case we will have angle independent reflection coefficients. We create a synthetic split-spread shot-gather over the laterally invariant medium using a finite-difference modelling scheme. In Figure 4.3 we show the modelled shot, and the migrated shot is shown in Figure 4.4.

To extract AVP or AVA information at a reflector position, we need information from more than one shot since each shot gives limited angle information. A schematic representation of angle information available from one shot is shown in Figure 4.5. Using information from the wave-equation angle-transform, this can further be illustrated by plotting $I(\mathbf{x}, p)$ (in gray-scale) overlaid the source correction term (in color-scale) at midpoints $x_{m,1} = -0.5$ km, $x_{m,2} = 0.0$ km, and $x_{m,3} = 0.5$ km shown in Figure 4.6.

By simulating more shots over one midpoint location x_m, we can extract angle information for larger angle coverage as shown schematically in Figure 4.7. We simulate 100 shots with a shot-distance of 10 m on both sides of x_m, in addition to one shot just above x_m. This produces the angle coverage shown in Figure 4.8,

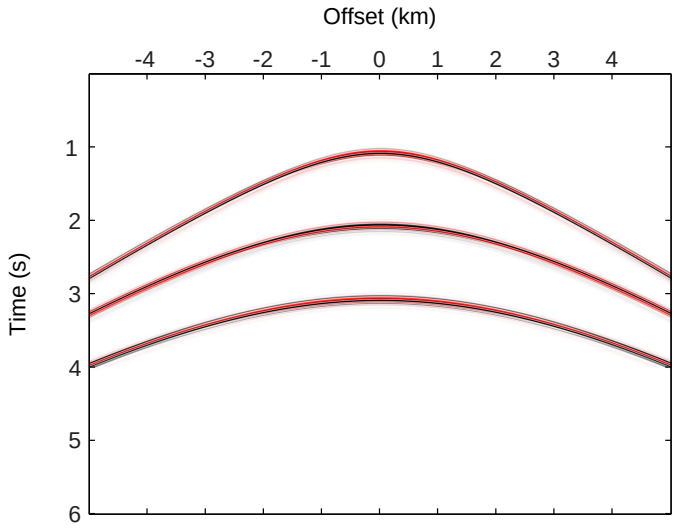

Figure 4.3: A synthetic shot-gather from a finite-difference modelling over the lateral invariant model example.

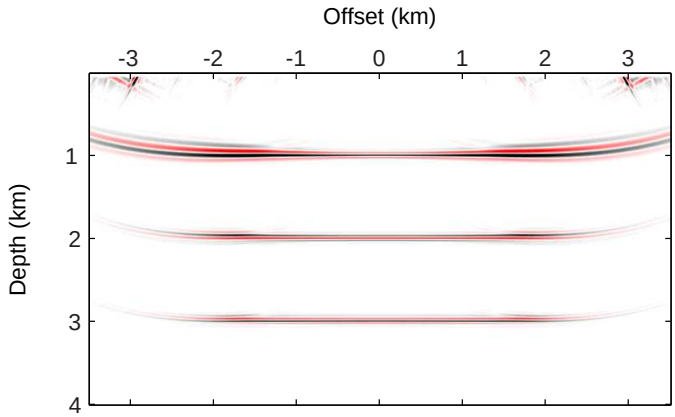

Figure 4.4: Migrated shot from the lateral invariant model with flux-normalized wavefields.

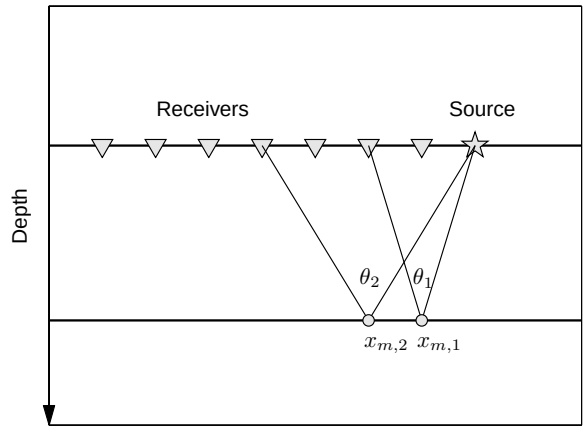

Figure 4.5: Schematic representation of angle information contained in one shot, where $x_{m,1}$ and $x_{m,2}$ are midpoint locations with information around angles θ_1 and θ_2. For each midpoint location, each shot only gives limited angle information.

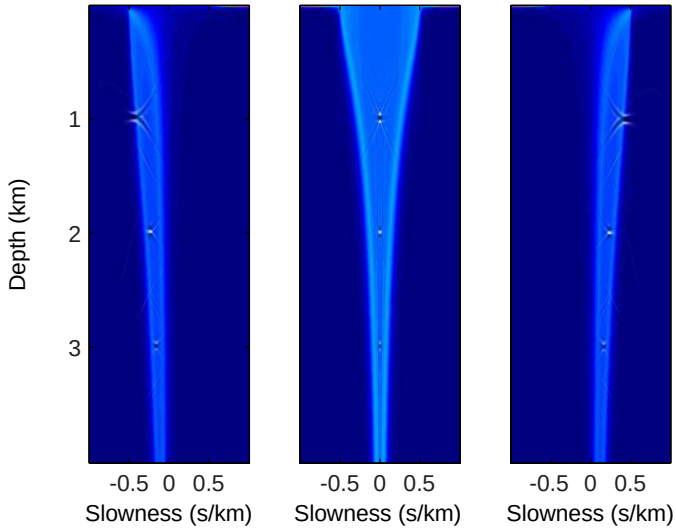

Figure 4.6: Slowness coverage $I(\mathbf{x}, p)$ from one shot (gray-scale) overlaid the corresponding source correction (color-scale) for (left) $x_{m,1} = -0.5$ km; (middle) $x_{m,2} = 0.0$ km; and (right) $x_{m,3} = 0.5$ km.

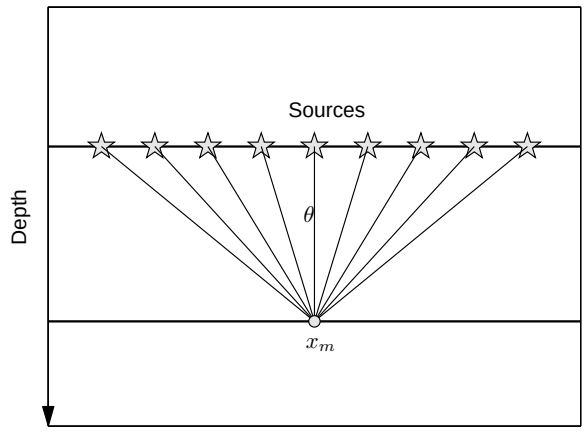

Figure 4.7: Schematic representation of angle coverage θ at one midpoint location x_m from a range of shots. To extract a larger range of angle coverage, each midpoint location requires several shots.

where we plot $I(\mathbf{x}, p)$ overlaid the corresponding source illumination for the fixed midpoint location x_m. We notice that the angle coverage for each reflector in depth is different (as expected).

At each reflector depth, we extract the peak amplitude of $R_{AT}(x_m, \theta)$ using equation 4.56. The result is depicted in Figure 4.9. We have plotted the AVA response for the reflector at 1 km up to 50 degrees (in red), the reflector at 2 km up to 35 degrees (in green) and the reflector at 3 km up to 25 degrees (in blue). In this example, we expect an angle-independent reflectivity, and from the result we see that the reflectivity is recovered relatively accurately for a wide range of angles. Due to a limited aperture, edge effects impact the results, and the largest angles on each reflector are affected.

4.6.2 Marine field seismic data example

We apply both conventional pressure-normalized and the derived flux-normalized methods to a field dataset from the Nordkapp Basin. The basin is located offshore Finnmark, in the Norwegian sector of the Barents Sea. It is an exploration area which exhibits complex geology and is challenging for seismic imaging. We have extracted a subset of a 2D survey which covers two salt dome structures partially. In Figure 4.10, the velocity model used in the migration is shown.

The dataset is composed by collecting and combining streamer data in two

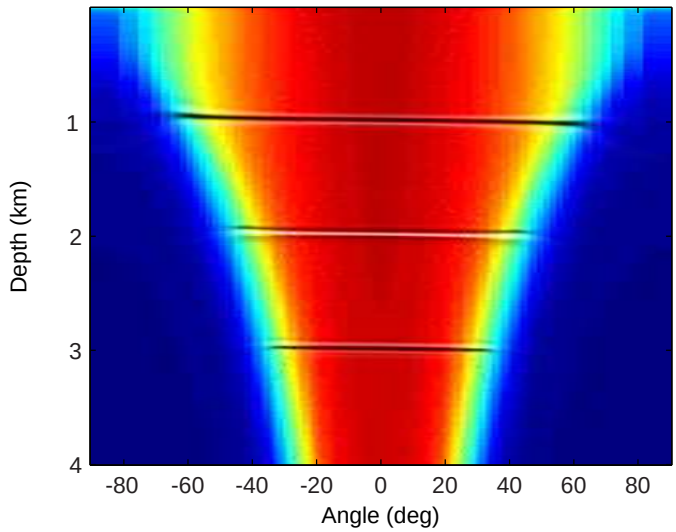

Figure 4.8: Angle coverage $I(\mathbf{x}, p)$ (gray-scale) from one spatial location x_m overlaid the corresponding source correction (color-scale) where the contribution from multiple shots are included.

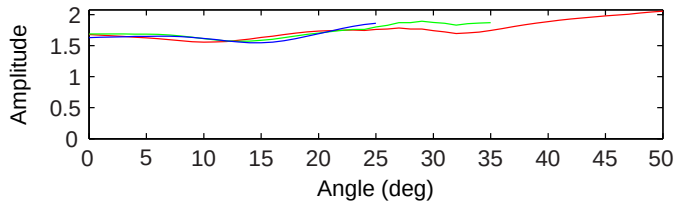

Figure 4.9: Peak amplitudes at each reflector at 1 km (red), 2 km (green), and 3 km (blue) for one spatial location x_m.

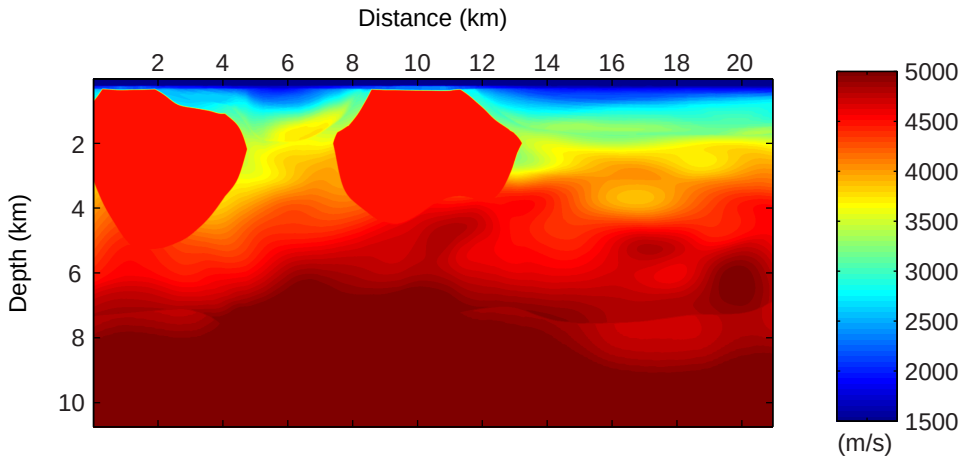

Figure 4.10: The velocity model used in the Nordkapp field data example.

directions, providing a split-spread configuration. Each shot is separated by 25.0 m, and in our example we have included a total of 775 shots. Each streamer has 1296 receivers with a hydrophone distance of 12.5 m and a total offset of about 8100 m on both sides of the source location. Notice that no demultiple is applied in the pre-processing step. In Figure 4.11 we show one extracted shot which is input to migration.

In the imaging, we have used a source signature comparable to a Ricker wavelet with a peak frequency of 17 Hz. We used 3-35 Hz of the frequency content of the data, and imaged the data down to 10 km. The total aperture of each shot was 16 km. For both the pressure-normalized and the flux-normalized wavefield decomposition, we migrate the dataset with the same downward continuation scheme and the same imaging condition. That is, we use a third-order Fourier finite-difference migration operator and an image condition which estimates the reflectivity by accounting for the source illumination. The flux-normalized migration has an approximation to the transmission loss correction applied at thin-slab boundaries using the minimum velocity at each slab given by the aperture of each migrated shot. In Figures 4.12 and 4.13 the pressure-normalized and the flux-normalized migrated sections are shown, respectively. By inspecting and comparing both sections, we see that we have an apparent similar amplitude response.

To quantify the difference between the migrated sections, we the compute difference between the absolute value of each section. The difference plot is

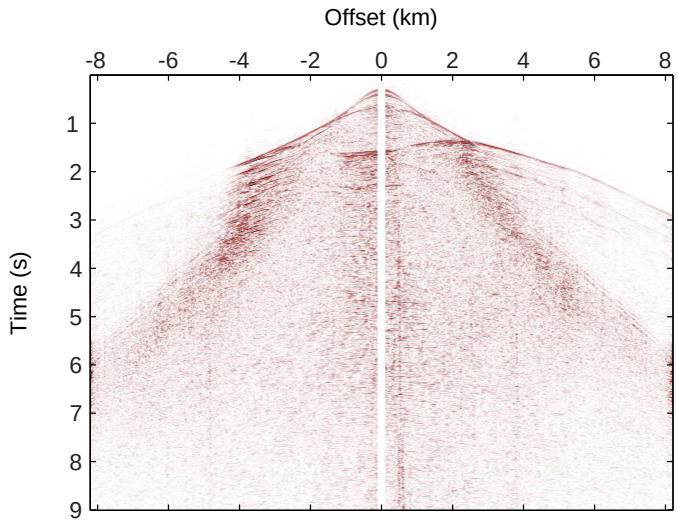

Figure 4.11: One extracted shot-gather used in the Nordkapp basin field data example.

shown in Figure 4.14. The red and black colors indicate that the flux-normalized image provides higher and lower amplitudes than the pressure-normalized image, respectively. In the shallower part of the difference image, from the surface to about 2 km, the pressure-normalized image appears to be dominating; however, these parts of the sections are also contaminated by low frequent migration noise. In the sediment basin between the two salt-domes, that is, below and around a distance of 6 km, no coherent energy appears below 2 km. Around approximately a distance of 14 km to 16 km at around depth 8 km, the flux-normalized images gives a higher amplitude response on some parts of a few subsurface reflectors. The peak amplitude difference is around one-tenth of the reflectivity image amplitudes.

Further, we extract a slowness gather from each of the migration approaches corresponding to lateral position of 14.4 km and these are shown in Figure 4.15. Figure 4.15(a) and Figure 4.15(b) shows the output from the pressure-normalized and flux-normalized approach, respectively. The gathers looks similar. Next, we extract one event at 7.8 km of depth on these gathers, as shown in Figure 4.16. For this event we extract the peak amplitudes for each of the migrated reflectors, and plot these in Figure 4.17 (top), where the red curve is the flux-normalized and the blue curve is the pressure normalized peak amplitudes. Finally, we take the difference between the normalized peak amplitudes (bottom), where the positive and negative values correspond to higher and lower peak amplitudes when using

flux-normalized variables. The plot shows differences between the results from the different approaches, and explains the difference plot in Figure 4.14.

4.7 Conclusions

By directional decomposing a wavefield using a flux-normalized eigenvalue decomposition, we have derived initial conditions for pre-stack depth migration of common-shot data. This decomposition simplifies the system of differential equations. Further, by neglecting interaction between directional components, we derive propagators for flux-normalized wavefields where we formulate a transmission loss compensation approach for flux-normalized wavefield propagation. By using the wave-equation angle transform, we formulate an unbiased estimate of the reflection coefficient. From our one-dimensional numerical example, we show that a flux-normalized directional decomposition provides accurate amplitude information in a medium where the parameters are function of depth only. Finally, we extend our approach to a laterally varying media. From a field data example, we observe some differences in the strength of the estimated reflectivity compared to a pressure-normalized approach.

4.8 Acknowledgments

The authors would like to thank Hans-Kristian Helgesen and Robert Ferguson for useful discussions, and Statoil for permission to publish data from the Nordkapp basin. This research has received financial support from the Norwegian Research Council via the ROSE project. Bjørn Ursin has also received financial support from VISTA.

4.A The wave-equation angle transforms

In terms of local Fourier transforms, the common-image gather in equation 4.55 can be expressed by

$$I(\mathbf{x},\mathbf{p}) = \left(\frac{1}{2\pi}\right)^5 \iiiint \hat{U}(\mathbf{x},\mathbf{k}^r,\omega)\hat{D}^*(\mathbf{x},\mathbf{k}^s,\omega)\mathrm{e}^{\mathrm{i}\mathbf{k}^r\cdot\mathbf{h}/2}\mathrm{e}^{\mathrm{i}\mathbf{k}^s\cdot\mathbf{h}/2}\mathrm{e}^{-\mathrm{i}\mathbf{p}\cdot\mathbf{h}}\mathrm{d}\mathbf{k}^r\mathrm{d}\mathbf{k}^s\mathrm{d}\omega \tag{4.A-1}$$

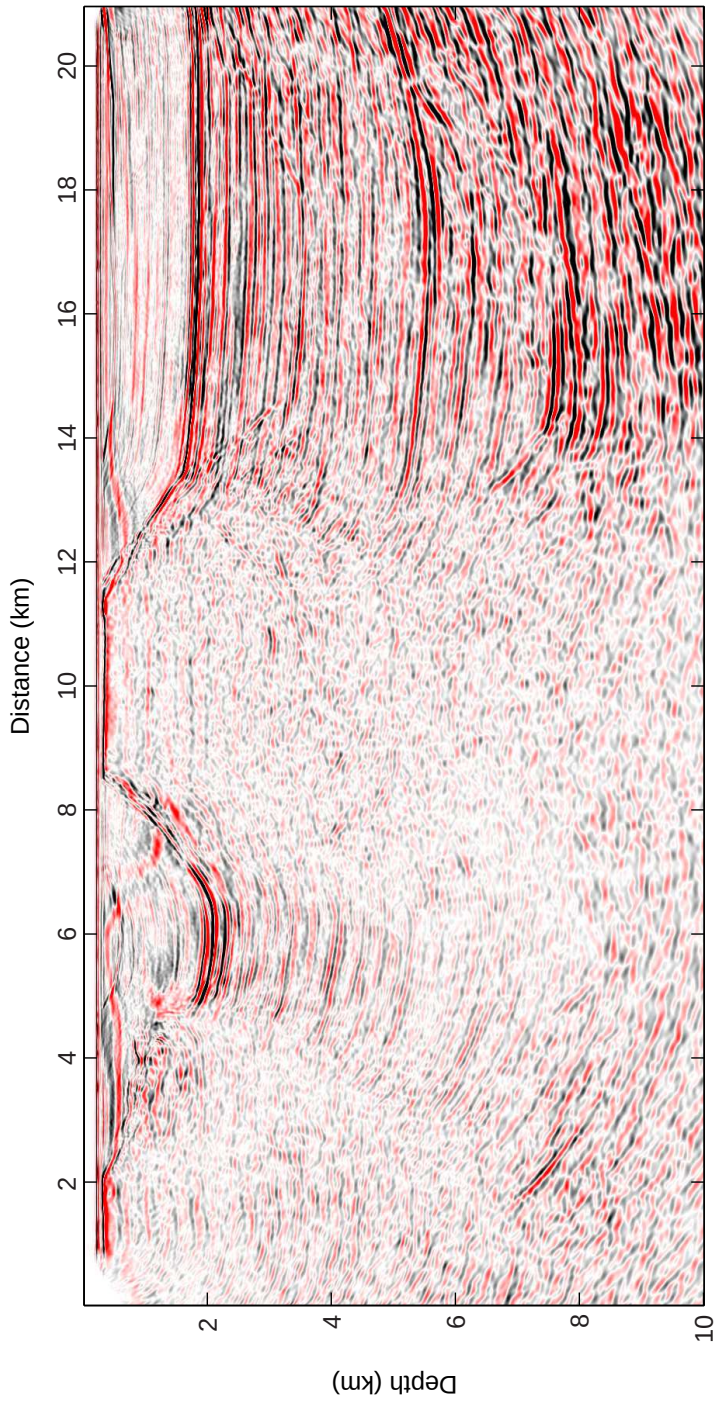

Figure 4.12: Migrated image of the Nordkapp field example with the pressure-normalized wavefield decomposition and migration approach.

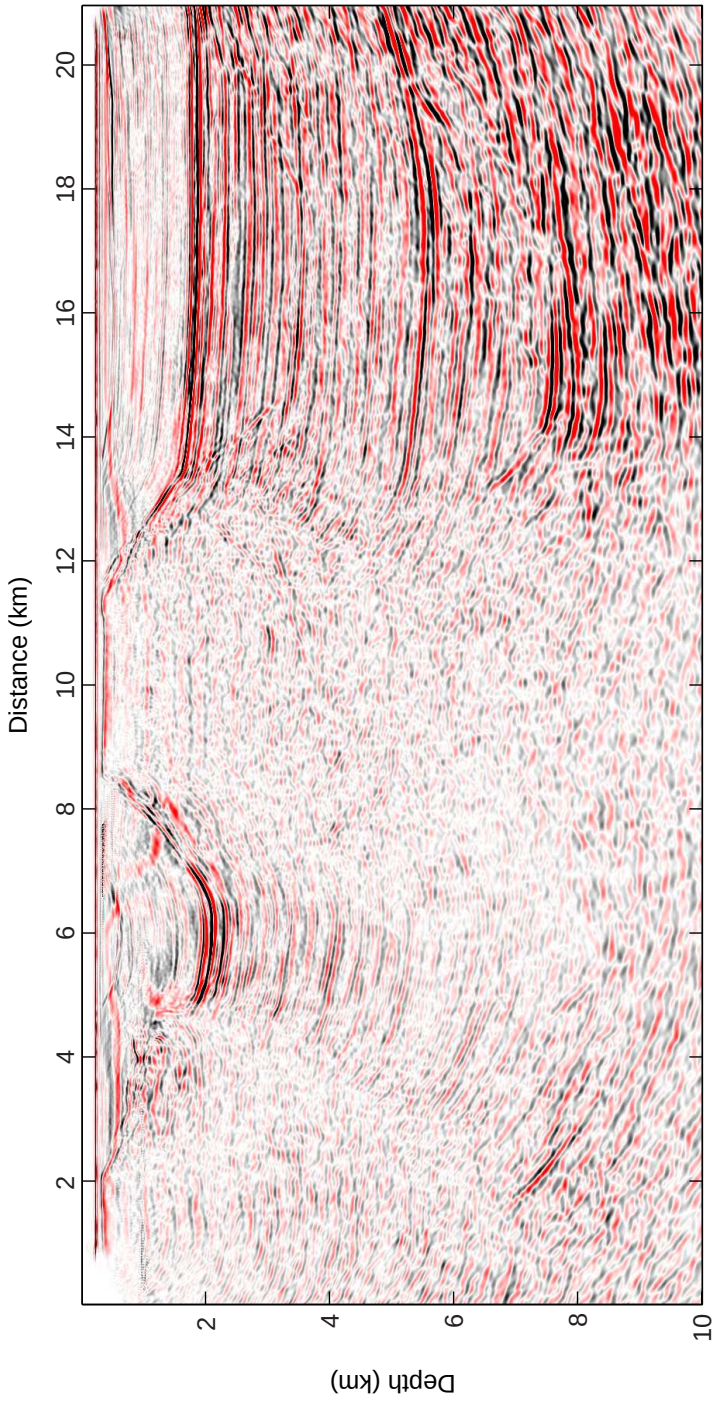

Figure 4.13: Migrated image of the Nordkapp field example with the flux-normalized wavefield decomposition and migration approach.

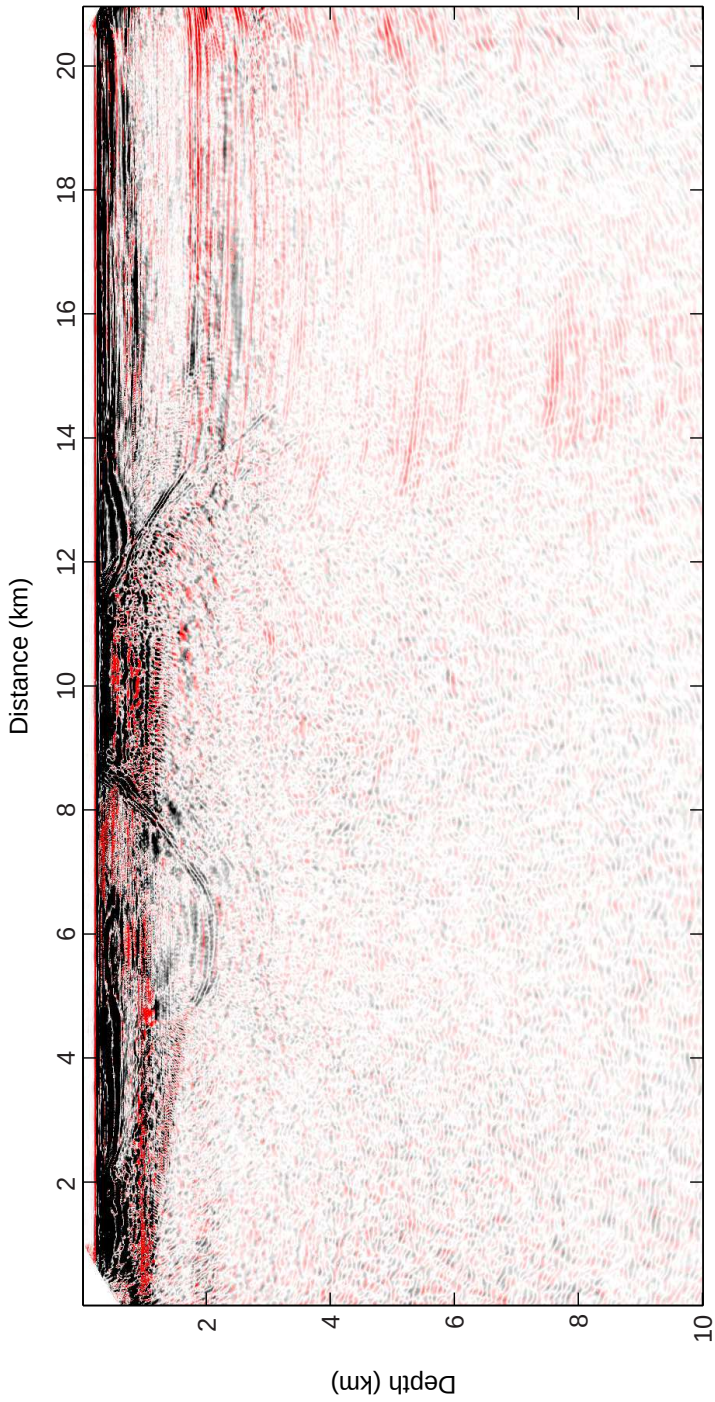

Figure 4.14: Difference of the absolute value of the migrated flux-normalized wavefield decomposition and the pressure-normalized wavefield decomposition sections of the Nordkapp field example. The red color indicates that the flux-normalized image is dominating, and black color indicates that the pressure-normalized image is dominating.

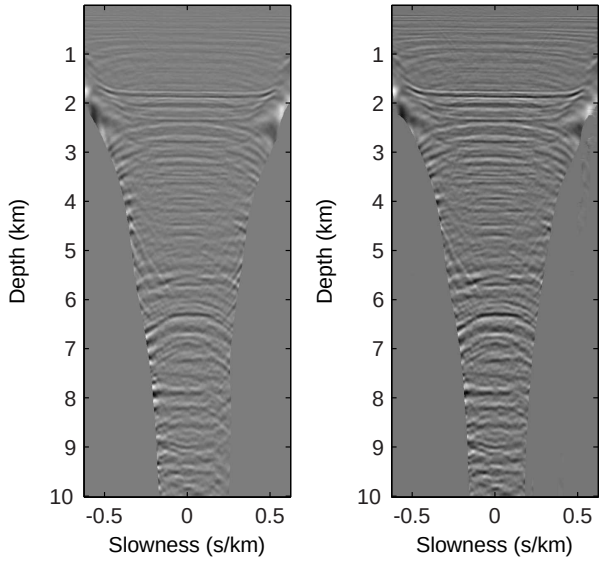

Figure 4.15: Slowness-gather at a distance of 14.4 km from the Nordkapp basin field data example. (a) with pressure-normalized and (b) flux-normalized variables.

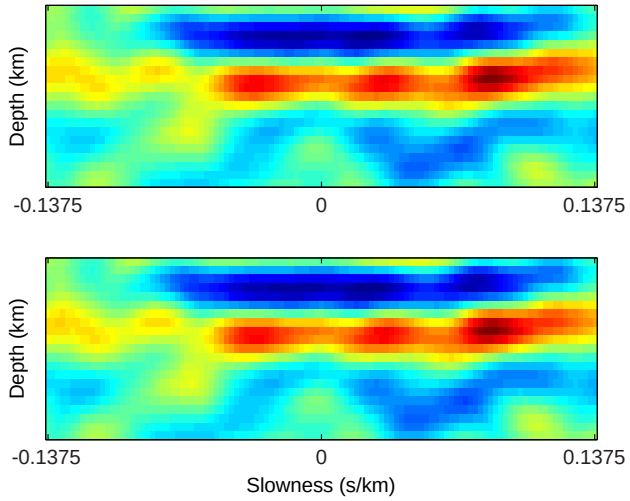

Figure 4.16: Extracted event at 7.8 km depth from the slowness-gathers in Figure 4.15 at a distance of 14.4 km for (top) flux-normalized variables and (bottom) pressure-normalized variables.

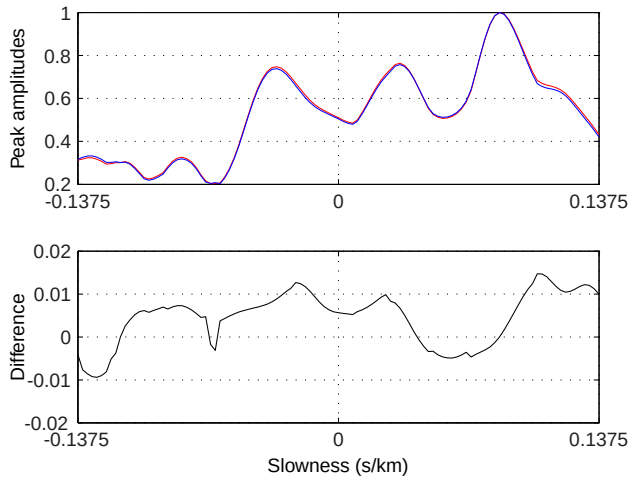

Figure 4.17: Normalized peak amplitudes along event in 4.16 (top) with flux-normalized variables (red line) and pressure-normalized variables (blue line). Difference between normalized peak amplitudes (bottom), where positive and negative values corresponds to higher and lower peak amplitudes in using flux-normalized variables.

where $\mathbf{k}^r = (k_1^r, k_2^r)$ and $\mathbf{k}^s = (k_1^s, k_2^s)$. Snell's law is

$$\hat{U}(\mathbf{x}, \mathbf{k}^r, \omega) = R(\mathbf{x}, \mathbf{q})\hat{D}^*(\mathbf{x}, \mathbf{k}^s, \omega)(2\pi)^2\delta(\mathbf{k}^r - \mathbf{k}^s). \tag{4.A-2}$$

Inserted in equation 4.A-1 this gives

$$I(\mathbf{x}, \mathbf{p}) = \left(\frac{1}{2\pi}\right)^3 \iiint R(\mathbf{x}, \mathbf{q})|\hat{D}(\mathbf{x}, \mathbf{k}, \omega)|^2 \mathrm{e}^{\mathrm{i}(\mathbf{k}-\omega\mathbf{p})\cdot\mathbf{h}} \mathrm{d}\mathbf{k}\mathrm{d}\omega \tag{4.A-3}$$

where $\mathbf{k}^r = \mathbf{k}^s = \mathbf{k} = \omega\mathbf{p}$. Further simplifications gives

$$\begin{aligned} I(\mathbf{x}, \mathbf{p}) =& \frac{1}{2\pi} \iint R(\mathbf{x}, \mathbf{q})|\hat{D}(\mathbf{x}, \mathbf{k}, \omega)|^2 \delta(\mathbf{k} - \omega\mathbf{p}) \mathrm{d}\mathbf{k}\mathrm{d}\omega \\ =& R(\mathbf{x}, \mathbf{q}) \int |\hat{D}(\mathbf{x}, \mathbf{k}, \omega)|^2 \mathrm{d}\omega \end{aligned} \tag{4.A-4}$$

The derivations above are only approximate, since finite-aperture effects have not been taken into consideration.

4.B Approximate transmission and reflection coefficients

The correction factor for downward propagation of the up- and downgoing wavefields is the transmission coefficient in equation 4.27:

$$\tilde{T}_u^{-1} = T_u^{-1}\left(\frac{Z_-}{Z_+}\right) = \frac{Z_+ + Z_-}{2\sqrt{Z_- Z_+}}. \tag{4.A-5}$$

With $Z_- = Z$ and $Z_+ = Z + \Delta$ this becomes

$$\begin{aligned}
\tilde{T}_u^{-1} &= \frac{2Z + \Delta}{2\sqrt{Z(Z+\Delta)}} \\
&= \frac{2Z + \Delta}{2Z\sqrt{1 + \frac{\Delta}{Z}}} \\
&\approx \frac{2Z + \Delta}{2Z\left(1 + \frac{\Delta}{2Z} - \frac{1}{8}\left(\frac{\Delta}{Z}\right)^2\right)}. \\
&= \frac{2Z + \Delta}{2Z + \Delta - \frac{Z\Delta}{4Z}} \\
&\approx 1 + \frac{1}{8}\left(\frac{\Delta}{Z}\right)^2
\end{aligned} \tag{4.A-6}$$

Using equation 4.12 for Z we obtain

$$\frac{\Delta}{Z} = \frac{\Delta(\rho c)}{\rho c} + \tan(\theta)\Delta\theta. \tag{4.A-7}$$

With

$$\sin(\theta) = pc \tag{4.A-8}$$

(p as in horizontal slowness in equation 4.39)

$$\Delta(\theta) = \tan(\theta)\frac{\Delta c}{c} \tag{4.A-9}$$

so that

$$\frac{\Delta}{Z} = \frac{\Delta(\rho c)}{\rho c} + \tan^2(\theta)\frac{\Delta c}{c}. \tag{4.A-10}$$

The reflection coefficient is approximated by

$$R_d = \frac{Z_+ - Z_-}{Z_+ + Z_-} \approx \frac{\Delta}{2Z}. \tag{4.A-11}$$

The correction term in equation 4.A-6 is second order in the change in impedance, and it is normally small. However, in the computation of the one-way wavefields there appears a product of such terms. This may not be small, and it should therefore be corrected for.

Chapter 5

Seismic imaging using lateral adaptive windows

Ø. Pedersen[1], S. Brandsberg-Dahl[2], B. Ursin[1]

[1] *Department of Petroleum Engineering and Applied Geophysics, NTNU*
[2] *Petroleum Geo-Service, Houston TX., USA*

One-way wavefield extrapolation methods are routinely used in 3D depth migration algorithms for seismic data. Due to their efficient computer implementations, such one-way methods have become increasingly popular and a wide variety of methods have been introduced. In salt provinces, the migration algorithms must be able to handle large velocity contrasts since the velocities in salt are generally much higher than in the surrounding sediments. This can be a challenge for one-way wavefield extrapolation methods. We present a depth migration method using one-way propagators within lateral windows for handling the large velocity contrasts associated with salt-sediment interfaces. Using adaptive windowing, we can handle large perturbations locally in a similar manner as the beamlet propagator, thus limiting the impact of the errors on the global wavefield. We demonstrate the performance of our method by applying it to synthetic data from the 2D SEG/EAGE A-A' salt model and an offshore real data example.

5.1 Introduction

Accurate imaging of seismic data in areas with strong velocity contrast is becoming increasingly important as the search for hydrocarbons enters areas with

very complex geology. There is currently high interest in salt provinces, for example the Gulf of Mexico. When salt is present, the migration algorithm must be able to handle large velocity contrasts because the velocity in salt is generally much higher than in the surrounding sediments. The salt bodies will act as acoustic lenses, spreading or concentrating energy in a "random way" (O'Brien and Gray, 1996). Proper handling of these focusing effects in the migration algorithm is crucial for obtaining a proper migrated image of the subsalt structures.

Several migration methods are routinely used in sub-salt imaging. They are normally classified as either Kirchhoff (Schneider, 1978) or wavefield extrapolation migrations depending on the underlying assumptions (Bleistein, 1987; Gazdag, 1978; Stolt, 1978). Kirchhoff methods explicitly impose a high-frequency assumption on the wave equation and typically use ray-tracing based methods to model the wave propagation in the subsurface. In areas with complex geology where multipathing occures, Kirchhoff methods may not provide reliable subsurface images (Biondi, 2006). Many wavefield methods are based on frequency domain one-way extrapolation of the wavefield because such operators are computationally cheap and robust. These methods naturally handle multi-pathing and can give better subsurface images in areas with complex geology. Different implementations can handle varying degrees of lateral velocity variation but in general the cost of these methods increases as a function of medium complexity. All one-way methods split the velocity model into a set of depth slabs and then apply the wavefield extrapolator to the wavefield, stepping it down into the model, one depth step at a time. There are three main families of frequency based one-way extrapolators; space domain; wavenumber domain; and mixed space-wavenumber domain operators, each class with its own strengths and weaknesses. Here, we will focus on the mixed space-wavenumber domain operators, which can only handle limited lateral velocity variation in a given depth slice. Ferguson and Margrave (2005) introduced the notion of planned seismic imaging, wherein each depth slab they select one propagator that is optimal from a performance objective in order to overcome some of the problems caused by this limitation.

When the lateral velocity contrast is small (or smooth), the split-step operator (Stoffa et al., 1990) is both cheap and accurate. The generalized-screen (Wu and Huang, 1992; Rousseau and de Hoop, 2001a) and the Fourier finite-difference (Ristow and Rühl, 1994) operators can handle larger velocity contrasts, but are computationally more expensive. The split-step, generalized-screen and Fourier finite-difference methods are all based on the thin-slab approximation. A laterally invariant background velocity is defined and the resulting velocity perturbations

may be large. Because these methods assume small lateral perturbations, they are no longer valid in the presence of large velocity variations usually found at salt-sediment interfaces.

Gazdag and Sguazzero (1984) introduce the phase-shift plus interpolation (PSPI) method, in which the wavefield is globally downward continued using a collection of reference velocities to accommodate lateral velocity variations and a subsequent interpolation in space-domain to reconstruct the extrapolated wavefield (see e.g. Bagaini et al. (1995) for details on how to extract a set of reference velocities). The cost of this approach is proportional to the number of reference velocities, which may be large. A generalized-screen propagator was presented by Jin and Wu (1999) and Wu and Jin (1997) using a windowed Fourier transform (WFT) approach. However, the broadly overlapping windows in the WFT limit the utility of this method (Chen et al., 2006). Ma and Margrave (2008) address the extension of phase-shift extrapolation to laterally inhomogenous media by utilizing a spatial Gabor transform involving a window construction, in which a split-step propagator is used with a local background velocity.

Recently, the beamlet propagator (Wu et al., 2000) has been introduced. This approach uses a local reference velocity and can in principle handle media with very strong lateral velocity variations. In the beamlet method, the velocity model for each slab is divided into lateral regular windows, where the local (windowed) velocity is again analyzed and separated into a background and a perturbation part. This will give a more accurate operator since the local perturbations will be smaller, except for in windows that contain, for example, a salt boundary. By decomposing the velocity model into regular windows in a standard salt-sediment setting, most neighboring windows would have small perturbations that can be handled as one larger window by a cheap propagator.

We build on these ideas and present an extrapolation operator that in lateral windows within a slab uses an optimal local extrapolator. The scheme is especially targeted for subsalt imaging with which we have to handle the large velocity contrasts associated with the salt-sediment interfaces. For each slab of the velocity model, we will first identify the "interesting" areas in the medium, i.e. we find the areas with high lateral medium perturbations. Next, we perform an adaptive windowing construction by separating the model into sediments, salt and the salt boundary. With this approach, we avoid the redundancy imposed by regular windowing. Finally, we choose an appropriate extrapolation operator for each window. We introduce a partition of unity to do the adaptive operator composition. The resulting operator handles the large lateral velocity perturbations locally such as the beamlet method (Chen et al., 2006), hence, it limits the spatial influence of

any errors this introduces in the global wavefield. We demonstrate the accuracy of the method with application to a standard synthetic data set and a field data example.

5.2 One-way wavefield extrapolation

For simplicity in the further developments, we will only consider an isotropic $2D$ medium. Let z denote the preferred direction of propagation and x the transverse direction. We will introduce an operator for one-way wave extrapolation along the z-direction of the model. To do this, it is convenient to slice the velocity model into thin slabs in this preferred direction, giving each layer a thickness of Δz. We can proceed by separating each slice of the velocity model into a background part $v_0(z)$ and a perturbation part $\delta v(x,z)$ such that

$$v(x,z) = v_0(z) + \delta v(x,z). \tag{5.1}$$

In this setting, we have a single reference-velocity profile $v_0(z)$, and a spatially varying velocity perturbation $\delta v(x,z)$. Hence, in each slab the wavefield will be propagated through the reference velocity and then corrected for the spatially varying perturbation or screen (Wu and Huang, 1992). For this approach to be valid, we have to fulfill the thin-slab approximation within each layer of the velocity model (of thickness Δz): $\partial_z v(x,z) = 0$ and $\partial_x v(x,z)$ is small. The last part is of concern for mixed space-wavenumber domain methods as are used here because the true slowness for the extrapolation is constructed as a perturbation away from a reference. If this perturbation becomes large, the quality of the slowness approximation will necessarily deteriorate or become impractical to compute.

In a source free region the scalar wave equation can be written as

$$\nabla^2 \Psi(x,z,\omega) = -k^2(x,z,\omega)\Psi(x,z,\omega), \tag{5.2}$$

where Ψ denotes the wavefield,

$$k(x,z,\omega) = \frac{\omega}{v(x,z)} \tag{5.3}$$

is the wave number, $v(x,z)$ is the scalar wave speed (velocity), and ω is the circular frequency. With the above assumptions, the wavefield $\Psi(x, z+\Delta z, \omega)$, at the next depth level $z + \Delta z$, can be approximated by the following downward continuation operator applied to the wavefield at the current depth level z:

$$\Psi(x, z+\Delta z) = \frac{1}{(2\pi)} \int \alpha(x, k_x, \Delta z) \overset{\wedge}{\Psi}(k_x, z) \mathrm{e}^{-\mathrm{i}k_x x} \mathrm{d}k_x, \tag{5.4}$$

where

$$\hat{\Psi}\ (k_x, z) = \int \Psi(x, z) \mathrm{e}^{\mathrm{i}k_x x} \mathrm{d}x. \tag{5.5}$$

The operator is applied for each single frequency and the complete wavefield is downward continued by acting on all frequency components. The symbol α is defined as the thin-slab propagator

$$\alpha(x, k_x, \Delta z) = \mathrm{e}^{\pm \mathrm{i}\Delta z k_z(x, k_x)}, \tag{5.6}$$

where the superscript sign corresponds to backward($-$) and forward($+$) propagation. The vertical wavenumber is given as

$$k_z(x, k_x) = \begin{cases} \sqrt{k(x,\omega)^2 - k_x^2} & \text{if } k(x,\omega)^2 \geq k_x^2, \\ \pm \mathrm{i}\sqrt{k_x^2 - k(x,\omega)^2} & \text{if } k(x,\omega)^2 < k_x^2. \end{cases} \tag{5.7}$$

Propagating the wavefield using equation 5.4 is expensive (Holberg, 1988). The computational cost of propagating the wavefield using equation 5.4 one depthstep Δz for each frequency ω is in 2D dominated by the number of samples M in the computational grid, and the cost is $\propto M^2$. More efficient one-way propagators can be constructed by an approximation of the thin-slab propagator in equation 5.6, in which the resulting propagator accounts for the background media in wavenumber domain and the perturbations in space domain. This allows the use of the fast Fourier transform (FFT), in which the cost is dominated by the number of samples M in the computational grid and is proportional to $M \log M$, which provides a significant cost reduction. For the split-step, generalized-screen and Fourier finite-difference methods, the background medium $v_0(z)$ is assumed constant within each thin slab Δz, (Stoffa et al., 1990; Wu and Huang, 1992; Rousseau and de Hoop, 2001a; Ristow and Rühl, 1994).

5.3 Lateral adaptive windows

In our new extrapolator, we will adapt the method described above but we will do so for individual lateral windows. In a typical slab, we will have three kinds of windows: windows that only contain sediments, windows that contain a salt-sediment interface, and windows that only contain salt. In a standard salt-sediment geology, the only windows with any challenging velocity contrast will be those that contain the boundary. Hence, we can apply a cheap operator, such as the split-step in all windows except for those with a salt-sediment boundary.

More formally, for each depth level z in the model, we find a collection of boundary points $\{x_j\}_{j=1}^{N}$, where $x_j, j = 1 \dots N$ denotes the lateral samples where we go from sediments to salt or vice versa. We define x_0 and x_{N+1} to be the first and last lateral samples in the model, respectively. Further, we choose a collection of window functions $\{\phi_j\}_{j=1}^{2N-1}$ as

$$\begin{aligned} \phi_{2j-1}(x) &= \chi_S[x_{j-1} + c : x_j - c], \quad j = 1, \dots, N+1, \\ \phi_{2j}(x) &= \chi_S[x_j - c - K : x_j + c + K], \quad j = 1, \dots, N, \end{aligned} \tag{5.8}$$

where χ_S is an appropriate window-function such that we have a partition of unity on each slab, i.e.

$$\sum_j \phi_j(x) = 1 \tag{5.9}$$

for all x, and the brackets denotes the support points of the window function. The coefficient c denotes the half number of samples on the window that is not tapered, while the coefficient K denotes the half number of samples on the tapered part of the window, as illustrated in Figure 5.1. We have defined the window functions in equation 5.8 such that neighboring windows have intersecting support by K sample points. This provides an interaction between the wavefields in neighboring windows so that energy is also exchanged between windows. Energy from a sediment or salt window is allowed to propagate into a neighboring window containing the salt-sediment interface. The choice of the parameter K depends on both the thickness Δz of the slab and the wave velocity v.

After identifying all salt-sediment interfaces within a thin slab, the total wavefield in this slab Ψ can be represented as the superposition of its windowed components

$$\begin{aligned} \Psi(x, z, \omega) &= \sum_{j=1}^{2N-1} \phi_j(x) \Psi(x, z, \omega) \\ &= \sum_{j=1}^{2N-1} \Psi_j(x, z, \omega), \end{aligned} \tag{5.10}$$

where $\{\phi_j\}_{j=1}^{2N}$ is the partition of unity.

For each window j, we assign a suitable extrapolation operator P_j thus the wavefield on the next depth is given by

$$\Psi(x, z + \Delta, \omega) = \sum_{j=1}^{2N-1} P_j(\Psi_j(x, z, \omega)), \tag{5.11}$$

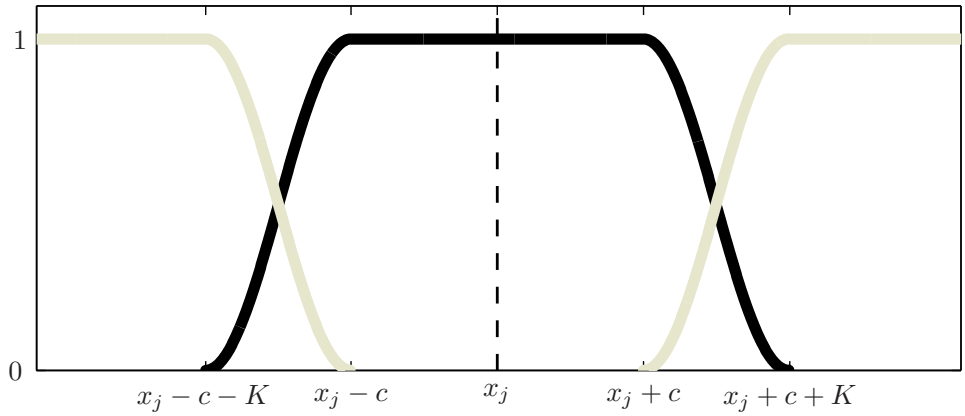

Figure 5.1: Partition of unity. The dashed line is the salt-sediment interface; the black line is the window containing the salt-sediment interface; the gray lines are the windows containing the surrounding regions.

where Ψ_j is defined in equation 5.10. The overlapping windowed wavefield components Ψ_j are propagated within each window and the superposition of all windows produce the wavefield at the next depth level. We choose each P_j in a "planned" fashion according to the local velocity contrast in the window. For windows with small contrast, we can use a simple operator such as the split-step, while we can use a more accurate operator in the windows containing the salt-sediment interface.

5.3.1 Velocity treatment

In this section we describe and compare the velocity treatment in the method described above with the generalized screen, Fourier finite-difference, and beamlet methods. Because the velocity decomposition in the generalized screen and Fourier finite-difference approaches are the same as for the split-step method, we will refer to these as split-step decomposition.

To illustrate the velocity model decomposition in the split-step and the beamlet methods, we will use the 2D SEG/EAGE A-A' salt model (see Figure 5.2 Aminzadeh et al. (1997)).

In Figure 5.3, we see the decomposition of the velocity model for the split-step in and for the beamlet method. From Figure 5.3 (b) we see that in the split-step case, the medium-perturbations are large in the presence of salt. For the beamlet method, we have decomposed the model using windows of 16 samples each. In

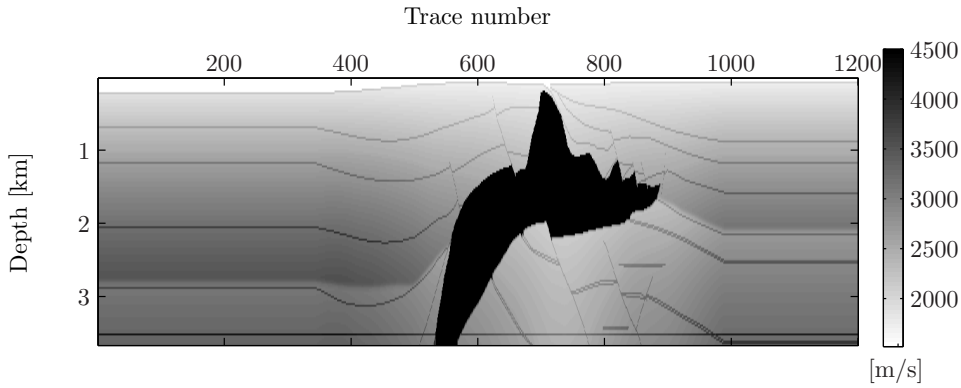

Figure 5.2: Section of the 2D EAGE/SEG A-A' saltmodel used in Figures 5.3 and 5.4.

Figure 5.3 (d), we see that the medium perturbations in the beamlet case are large only in windows where the salt boundary is present. In both methods, we have used the background velocity $v_0(z) = \min_x v(x, z)$.

To illustrate the velocity-model decomposition of the lateral adaptive windowing method, we use the same section of the 2D SEG/EAGE A-A' salt model as for the model decomposition in the beamlet and split-step methods.

We choose $c = 8$ and $K = 4$. Figure 5.4 shows the decomposition of the velocity model for the lateral adaptive windowing scheme described above. For the purpose of this illustration, we display only the non-overlapping velocities. The decomposition only differs from the split-step decomposition in the presence of salt within any depth slab. Within the depth slabs containing salt velocities, the size of the perturbations are similar to those of the beamlet method. The adaptive lateral windowing decomposition use $\sim$ 1-12 windows in each of the slabs, compared to the beamlet method that used ~ 75 windows in all slabs.

5.4 Numerical results

5.4.1 Model of vertical interface

To compare the accuracy between the lateral adaptive windowed extrapolation method and alternative methods, we first produce a snapshot in a vertical model of an impulse response with alternative one-way methods. We define a vertical model

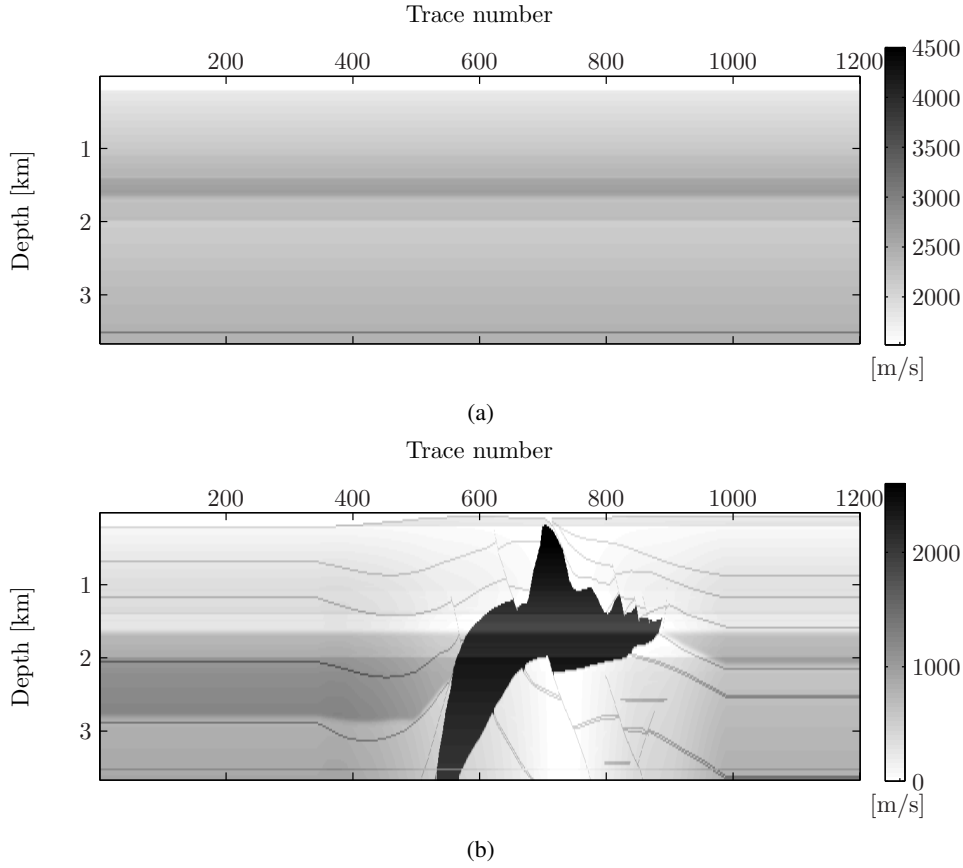

Figure 5.3: Comparison of the velocity-model decomposition for the split-step and the beamlet method. (a) Background velocity v_0 and (b) velocity perturbation δv for the split-step velocity-model decomposition.

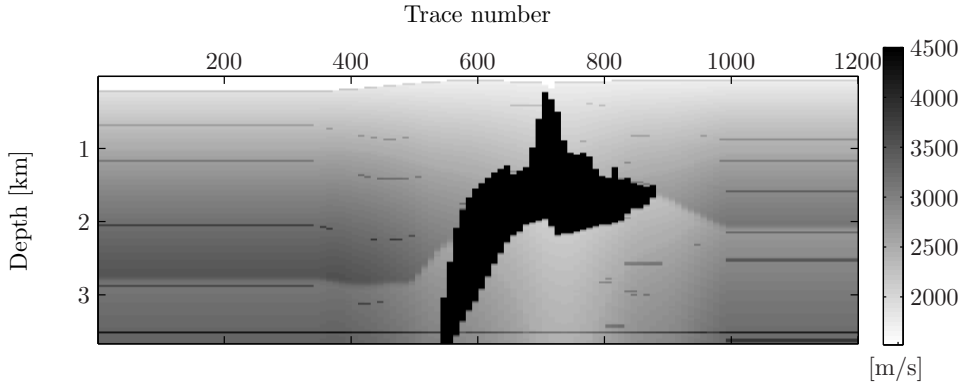

(c)

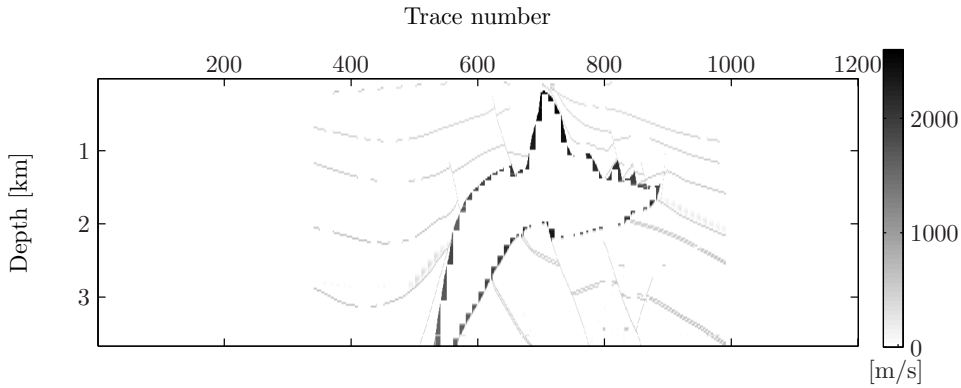

(d)

Figure 5.3: Comparison of the velocity-model decomposition for the split-step and the beamlet method. (c) Background velocity v_0 and (d) velocity perturbation δv for the beamlet velocity-model decomposition.

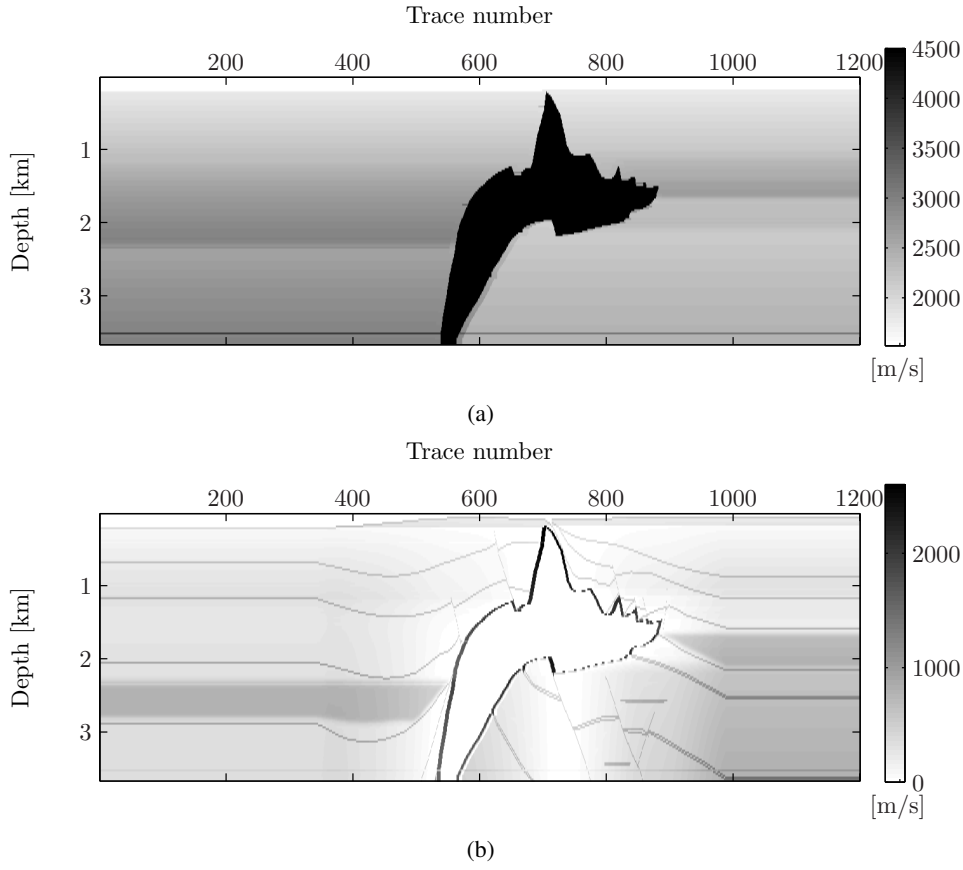

Figure 5.4: Velocity-model decomposition for the lateral adaptive window method with (a) the background velocity v_0 and (b) the velocity perturbations δv. The decomposition only differ from the split-step decomposition (Figure 5.3 (a-b)) in the presence of salt

by

$$v(z,x) = \begin{cases} 3000 \text{ m/s}, x \leq x_s, \\ 4500 \text{ m/s}, x > x_s, \end{cases} \tag{5.12}$$

where x_s denotes the lateral location of the impulse. The high-velocity area is assumed to be salt, while the low-velocity area is assumed to be the surrounding sediments. We place the source at the top of the model with lateral position $x_s = 5$ km and record the wavefield in the model at time $t = 1.0$ s. The theoretical wavefront is shown with a dashed line. Figure 5.5 (a) illustrates the impulse response using the split-step method interleaved with the velocity model. Here the background velocity is taken to be the minimum velocity in each slab; hence, the wavefront in the slower part of the model is accurate. In the faster part of the model, the perturbations are large; hence the wavefront is not correctly placed for larger angles. The placement of the wavefront can be improved for larger angles by using the more accurate second order Fourier finite-difference operator, described by Ristow and Rühl (1994), as shown in Figure 5.5 (b). The snapshot of the wavefront for the lateral adaptive windowed extrapolator is shown in Figure 5.5 (c) where we have used the split-step operator as P_j in all windows. We chose $K = 4$ and $c = 8$ in equation 5.8. With this method, the wavefront is more correctly positioned. We notice a minor ringing in the snapshot produced by the lateral adaptive windowed extrapolator.

5.4.2 Imaging the 2D SEG/EAGE A-A' salt model

Our first test of migration using lateral adaptive windows is on the 2D SEG/EAGE A-A' salt model. This model contains sediments surrounding a salt body, giving large lateral medium perturbations in addition to having a complex structure. We compare the migrated images with and without the lateral adaptive windowing. The model has 150 samples in depth z and 1200 samples in the lateral direction x, with $dx = dz = 24.38$ m (see Figure 5.2). A common-shot section was produced with 325 shots with each shot having 176 receivers with 626 samples per trace, and a sampling interval dt=8 ms. The first shot is located on trace 336 in the velocity model and the shot spacing is 2 samples. Figure 5.6 shows a subsection of the common-shot prestack depth migrated images with and without the lateral adaptive windowing scheme. Figure 5.6(a) shows the image migrated with the split-step operator. In Figure 5.6(b), the lateral window operator is used, where we used the split-step operator in the sediments, the phase-shift operator in the salt, and an extended split-step operator (Kessinger, 1992) in the salt-sediment interfaces. We chose $K = 4$ and $c = 8$ in equation 5.8.

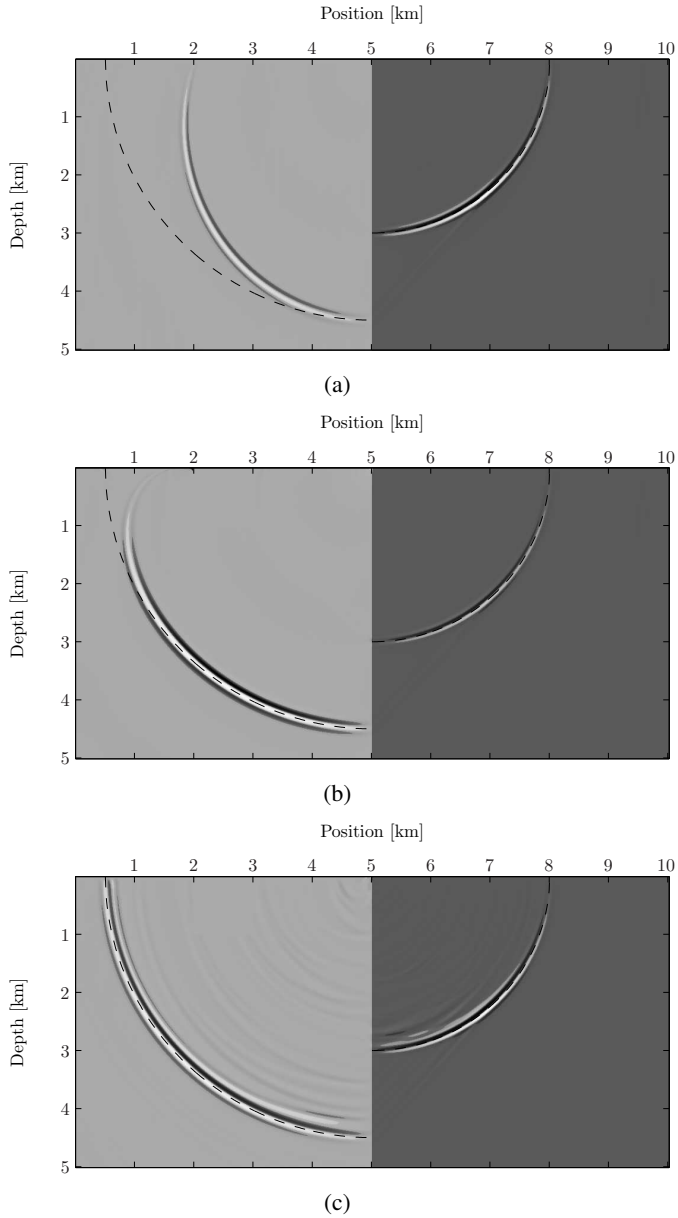

Figure 5.5: Snapshots of the wavefield produced by a point source at the surface at time $t = 1.0$ s interleaved with the velocity model using (a) the split-step extrapolator, (b) the second-order Fourier finite-difference extrapolator and (c) the lateral adaptive extrapolator. The dashed line superimposed onto the snapshots represents the theoretical wavefront. The split-step extrapolator (a) misposition the wavefront in the high-velocity area except for small angles, while the Fourier finite-difference extrapolator (b) corrects for higher angles. The lateral adaptive extrapolator (c) correctly positions the wavefront.

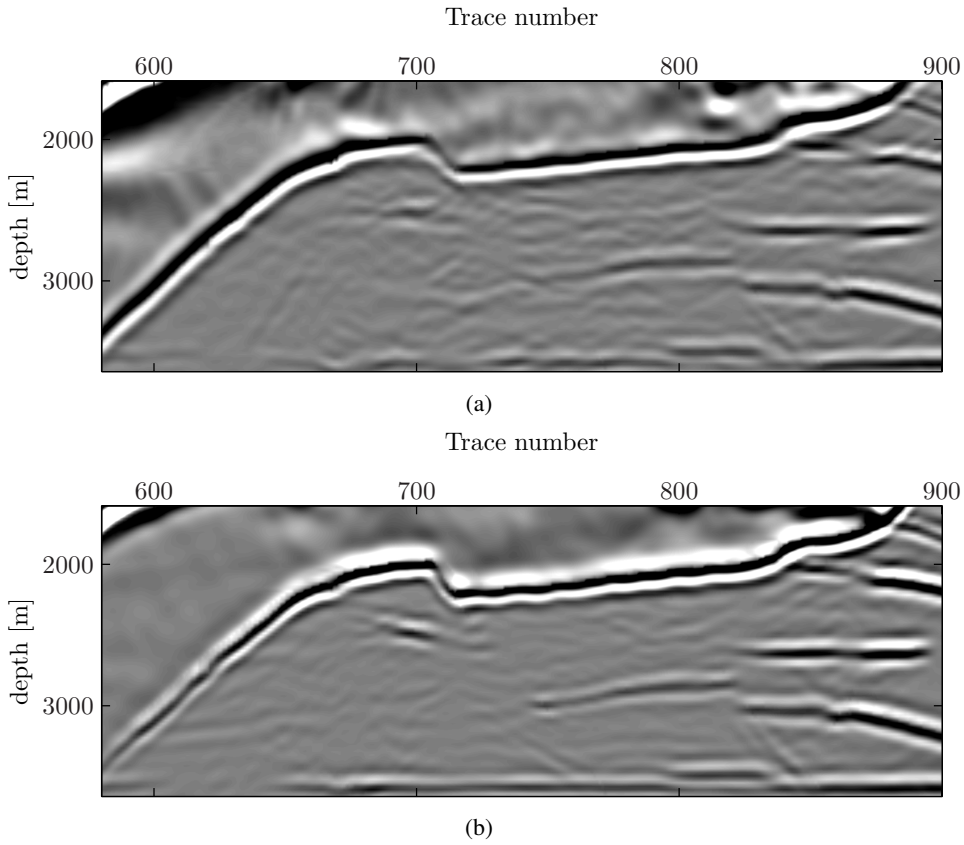

Figure 5.6: Comparison of the prestack depth-migration results of data obtained from Figure 5.2 with (a) the split-step operator and with (b) the lateral adaptive windowed split-step operator. Using the lateral adaptive scheme improves the focusing of energy.

Compared to the split-step method, the lateral windowing method focuses the energy better below the salt, in addition to image the base of salt better.

5.4.3 Field data example

To further test the lateral adaptive wave-extrapolation method, we consider a field dataset. The dataset is aquired in the south Atlantic, and the subsurface contains strong lateral velocity variations assosiated with salt-sediment interfaces. The dataset is migrated using a split-step propagator, a second order Fourier finite-

difference propagator and the lateral adaptive scheme. In the lateral adaptive method, we used a split-step operator in the sediment velocities, a phase-shift in the salt velocities and a second order Fourier finite-difference operator in the salt-sediment velocity interfaces. Further, we set $c = K = 8$ in determining the adaptive window sizes as described in equation 5.8. In Figure 5.7 we see the result after migration using the lateral adaptive scheme; in Figure 5.8 we see the result after migration using the split-step propagator; and in Figure 5.7 we see the result after migration using the second order Fourier finite-difference propagator. Notice that (z_1, x_1) is some reference point in the subsurface. We have circled in on an area of interest in the presens of salt velocities for which our results are compared with migration using the split-step and an second order Fourier finite-difference scheme. The comparisons are illustrated in Figure 5.10. In Figure 5.10 a) we show the result using our lateral adaptive scheme. Notice that (z_0, x_0) is some reference point in the subsurface. In Figure 5.10 b) and c) we show the results from the split-step and the Fourier finite-difference migration, respectively.

From the results, the proposed method gives better focusing in some places. It also do a better job in imaging some dipping events. We also notice that with our method we see more coherent energy in the deeper part of the image.

5.5 Discussion

The examples show that the application of lateral adaptive windows in the construction one-way operators has the potential of increasing subsalt resolution. There are two main steps in our method: the lateral adaptive construction of the windows and the choice of operator. The window construction is fast and it is easy to implement in 2D. An extension to three dimensions would require an identification of the salt boudaries as for the 2D case. Furthermore, it would require a window construction of salt, sediment and salt-sediment interface windows, but where the windows now consists of a 2D partition of unity for each depth slice of the velocity model. In the case of very complex salt geometries, the number of windows could become large. In this case, an extension of the size of the windows would limit the total number of windows. The cheap operator performs well in the sediments and inside the salt. However, in the windows containing the salt-sediment interfaces, the lateral velocity contrasts are large, and a more expensive operator could be used. As seen in Figure 5.5, some minor artifacts (ringing) may occure with the proposed scheme which are not present in the other methods. Similar artifacts are found in the example with the vertical model when using a second order Fourier finite-difference operator in the windows containing

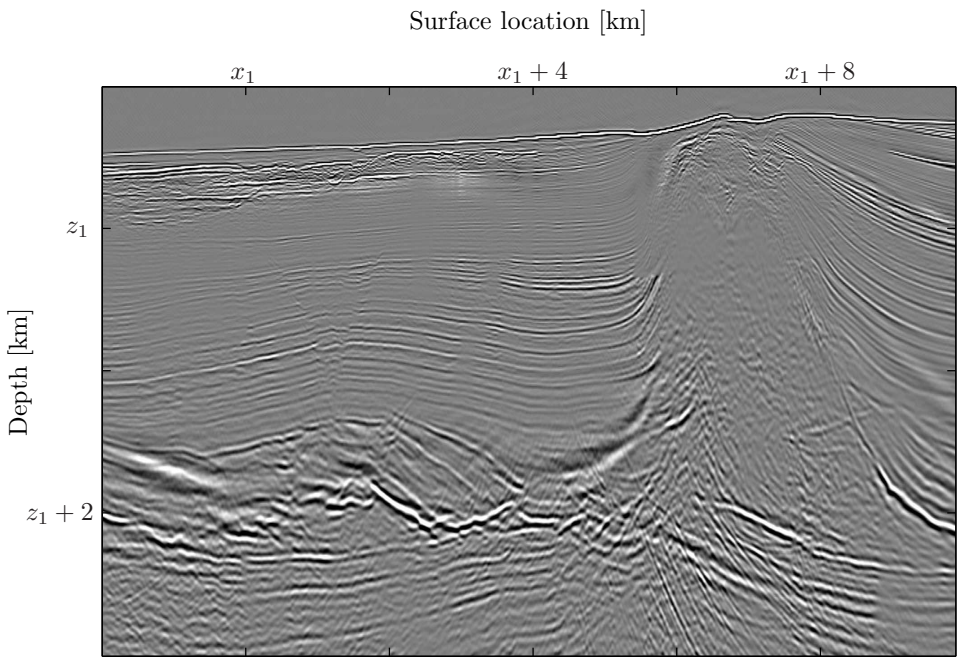

Figure 5.7: The prestack depth-migration result obtained using the lateral adaptive windowed operator.

the salt-sediment interfaces. The artifacts are likely related to the accuracy of the propagators used in the windows containing the salt-sediment interfaces. These artifacts are not apparent in the field data example.

The computational cost of propagating the wavefield one depthstep Δz with the proposed scheme can be described relative to the cost of an FFT. For example, if we let n_j denote the number of samples in the j-th computational window, the cost is proportional to C, where

$$C = l \sum_{j=1}^{N} n_j \log n_j + k \sum_{k=1}^{N} n_k \log n_k, \tag{5.13}$$

and where l and k are the relative cost of the operators used in the windows with and without challenging velocity contrasts, respectively. If we use a second order Fourier finite-difference operator in the salt-sediment windows and a split-step operator in the remaining windows, we have $l \approx 2$ and $k \approx 1$.

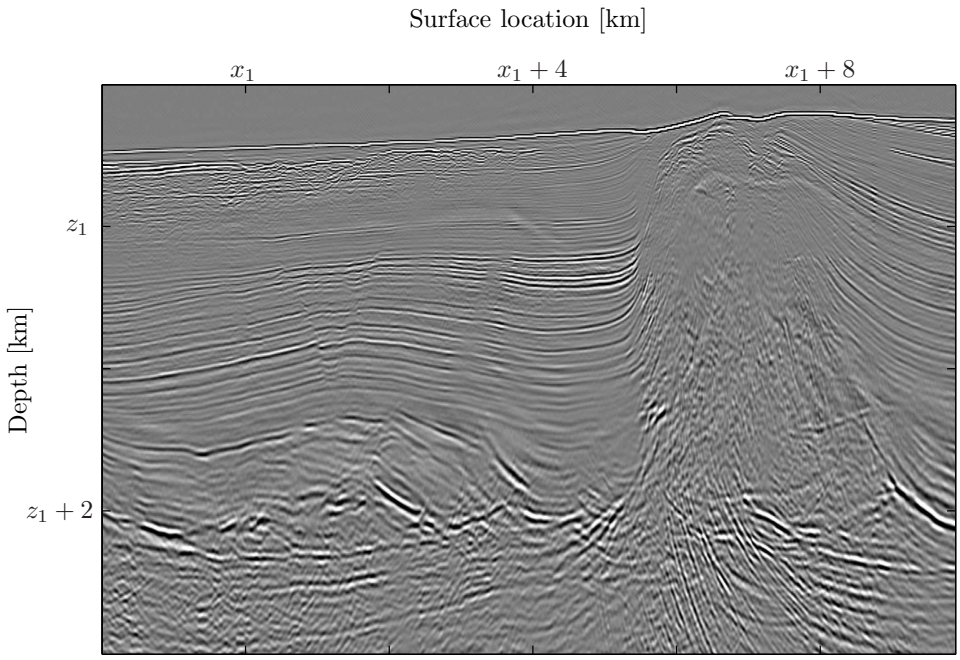

Figure 5.8: The prestack depth-migration result obtained using the split-step operator.

5.6 Conclusions

In this paper, we have developed a new method for subsalt imaging by introducing laterally adaptive windows and one-way extrapolation operators. This method allows for one-way extrapolation in media with large lateral velocity variations. We have given examples by using cheap propagators, and improved the subsalt resolution. The choice of operator on the lateral windows with large perturbations should be one which handles lateral variations well, while a cheap operator can be used on areas with small perturbations.

5.7 Acknowledgments

We would like to thank GXT for premission to show field data from the south Atlantic. We are grateful to the associate editor, Ru Shan-Wu and the other anonymous reviewers from *Geophysics* for constructive remarks and suggestions that helped improve this paper. This research was partly developed during a BP

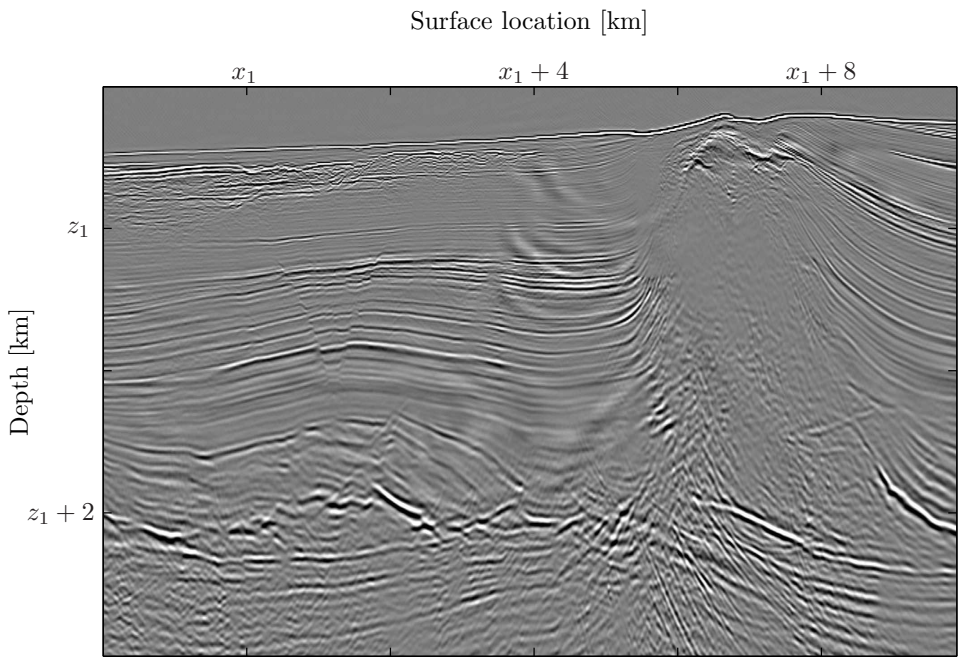

Figure 5.9: The prestack depth-migration result obtained using the Fourier finite-difference operator.

internship, and was partly supported by the Norwegian Research Council via the ROSE project. We would like to thank BP for allowing us to publish this work. Bjørn Ursin has received financial support from StatoilHydro ASA through the VISTA project and from the Norwegian Research Council through the ROSE project.

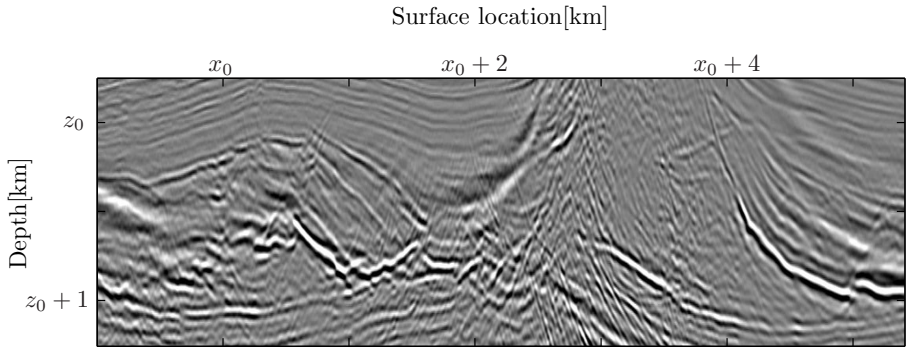

(a) Lateral adaptive windows

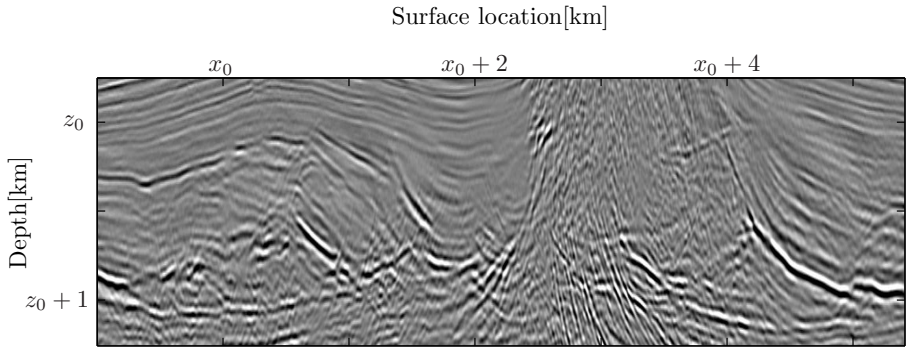

(b) Split-step Fourier

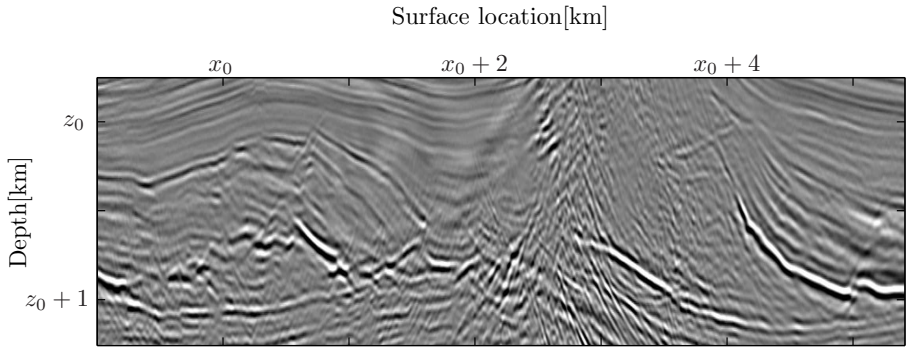

(c) Fourier finite-difference

Figure 5.10: Comparison of the prestack depth-migration results using (a) the lateral adaptive windowed operator (b) the split-step operator and with (c) the second order Fourier finite-difference operator. The Fourier finite-difference operator (c) provides better focusing than the split-step operator (b) as expected. The lateral adaptive operator provides similar results as the Fourier finite-difference operator, while some areas are better focused compared to the Fourier finite-difference approach.

References

Abma, R., N. Kabir, K. H. Matson, S. Michell, S. A. Shaw, and B. McLain, 2005, Comparisons of adaptive subtraction methods for multiple attenuation: The Leading Edge, **24**, 277–280.

Aki, K. and P. G. Richards, 1980, Quantitative seismology, theory and methods: Volume 1: W. H. Freeman and Company.

Alkhalifah, T., 1998, Acoustic approximations for processing in transversely isotropic media: Geophysics, **63**, 623–631.

———, 2000a, An acoustic wave equation for anisotropic media: Geophysics, **65**, 1239–1250.

———, 2000b, Prestack phase-shift migration of separate offsets: Geophysics, **65**, 1179–1194.

Alkhalifah, T. and K. Larner, 1994, Migration error in transversely isotropic media: Geophysics, **59**, 1405–1418.

Aminzadeh, F., J. Brac, and T. Kunz, 1997, 3-D salt and overthrust models: SEG/EAGE 3D Modeling Series No. 1.

Amundsen, L., 2001, Elimination of free-surface related multiples without need of the source wavelet: Geophysics, **66**, 327–341.

Amundsen, L. and A. Reitan, 1995, Decomposition of multicomponent sea-floor data into upgoing and downgoing P- and S-waves: Geophysics, **60**, 563–572.

Amundsen, L. and B. Ursin, 1991, Frequency-wavenumber inversion of acoustic data: Geophysics, **56**, 1027–1039.

Audebert, F., V. Dirks, and A. Pettenati, 2006, TTI anisotropic depth migration: What tilt estimate should we use?: 76th Annual International Meeting, SEG, Expanded Abstracts, 2382–2386.

Bagaini, C., E. Bonomi, and E. Pieroni, 1995, Data parallel implementation of 3D PSPI: 65th Annual International Meeting, SEG, Expanded Abstracts, 188–191.

Barkved, O., B. Bartman, B. Compani, J. Gaiser, R. VanDok, T. Johns, P. Kristiansen, T. Probert, and M. Thompson, 2004, The many facets of multicomponent seismic data: Oilfield Review, 42–56.

Berryman, J. G., 1979, Long-wave elastic anisotropy in transversely isotropic media: Geophysics, **44**, 896–917.

Betti, E., 2007, Theory of the Elasticity of the Professor Enrico Betti, *in* Classics of Elastic Wave Theory: SEG, Geophysics Reprints Series No. 24, 223–242.

Beylkin, G., 1985, Imaging of discontinuities in the inverse scattering problem by inversion of a causal generalized radon transform: Journal of Mathematical Physics, **26**, 99–108.

Biondi, B., 2006, 3D seismic imaging: SEG, Investigations in Geophysics Series No. 14.

Bishop, T. N., K. P. Bube, R. T. Cutler, R. T. Langan, P. L. Love, J. R. Resnick, R. T. Shuey, D. A. Spindler, and H. W. Wyld, 1985, Tomographic determination of velocity and depth in laterally varying media: Geophysics, **50**, 903–923.

Bleistein, N., 1987, On the imaging of reflectors in the Earth: Geophysics, **52**, 931–942.

Bremmer, H., 1951, The W.K.B. approximation as the first term of a geometric-optical series: Communications on Pure and Applied Mathematics, **4**, 105–115.

Cao, J. and R.-S. Wu, 2006, Study of the influence of propagator amplitude correction on image amplitude using beamlet propagator with local WKBJ approximation: 76th Annual International Meeting, SEG, Expanded Abstracts, 2499–2503.

———, 2008, Amplitude compensation for one-way wave propagators in homogeneous media and its application to seismic imaging: Communications in Computational Physics, **3**, 203–221.

Červenỳ, V., 2001, Seismic ray theory: Cambridge University Press.

Chen, L., R.-S. Wu, and Y. Chen, 2006, Target-oriented beamlet migration based on Gabor-Daubechies frame decomposition: Geophysics, **71**, S37–S52.

Claerbout, J. F., 1970, Coarse grid calculations of waves in inhomogeneous media with application to delineation of complicated seismic structure: Geophysics, **35**, 407–418.

———, 1971, Toward a unified theory of reflector mapping: Geophysics, **36**, 467–481.

———, 1976, Fundamentals of geophysical data processing: McGraw-Hill New York.

———, 1985, Imaging the Earth's interior: Blackwell Scientific Publications.

Clayton, R. W. and R. H. Stolt, 1981, A Born-WKBJ inversion method for acoustic reflection data: Geophysics, **46**, 1559–1567.

de Bruin, C. G. M., C. P. A. Wapenaar, and A. J. Berkhout, 1990, Angle-dependent reflectivity by means of prestack migration: Geophysics, **55**, 1223–1234.

de Hoop, M., R. van der Hilst, and P. Shen, 2006, Wave-equation reflection tomography: annihilators and sensitivity kernels: Geophysical Journal International, **167**, 1332–1352.

Dellinger, J., F. Muir, and M. Karrenbach, 1993, Anelliptic approximations for TI media: Journal of Seismic Exploration, **2**, 23–40.

Ellingsrud, S., T. Eidesmo, S. Johansen, M. Sinha, L. MacGregor, and S. Constable, 2002, Remote sensing of hydrocarbon layers by seabed logging (SBL) Results from a cruise offshore Angola: The Leading Edge, **21**, 972–982.

Etgen, J., S. H. Gray, and Y. Zhang, 2009, An overview of depth imaging in exploration geophysics: Geophysics, **74**, WCA5–WCA17.

Farra, V., 2001, High-order perturbations of the phase velocity and polarization of qP and qS waves in anisotropic media: Geophysical Journal International, **147**, 93–104.

Ferguson, R. J. and G. F. Margrave, 2005, Planned seismic imaging using explicit one-way operators: Geophysics, **70**, S101–S109.

Foss, S.-K., M. Rhodes, B. Dalstrøm, C. Gram, and A. Welbon, 2008, Geologically constrained seismic imaging — workflow: Geophysics, **73**, VE313–VE319.

Fowler, P. J., 2003, Practical VTI approximations: a systematic anatomy: Journal of Applied Geophysics, **54**, 347–367.

Gazdag, J., 1978, Wave equation migration with the phase-shift method: Geophysics, **43**, 1342–1351.

Gazdag, J. and P. Sguazzero, 1984, Migration of seismic data by phase shift plus interpolation: Geophysics, **49**, 124–131.

Granli, J., B. Arntsen, A. Sollid, and E. Hilde, 1999, Imaging through gas-filled sediments using marine shear-wave data: Geophysics, **64**, 668–677.

Hale, D., N. R. Hill, and J. Stefani, 1992, Imaging salt with turning seismic waves: Geophysics, **57**, 1453–1462.

Han, Q. and R.-S. Wu, 2005, A one-way dual-domain propagator for scalar qP-waves in VTI media: Geophysics, **70**, D9–D17.

Harlan, W., 1995, Flexible seismic traveltime tomography applied to diving waves: Stanford Exploration Project Report, **89**, 145–164.

Hill, R., 2001, Prestack Gaussian-beam depth migration: Geophysics, **66**, 1240–1250.

Hokstad, K., 2000, Multicomponent Kirchhoff migration: Geophysics, **65**, 861–873.

Holberg, O., 1988, Towards optimum one-way wave propagation: Geophysical Prospecting, **36**, 99–114.

Ikelle, L. and L. Amundsen, 2005, Introduction to petroleum seismology: SEG, Investigations in Geophysics Series No. 12.

Jin, S. and R.-S. Wu, 1999, Depth migration with a windowed screen propagator: Journal of Seismic Exploration, **8**, 27–38.

Johnson, E. A. E., 1998, Gravity and magnetic analyses can address various petroleum issues: The Leading Edge, **17**, 98–98.

Jones, I. F., 2010, An Introduction to Velocity Model Building: EAGE Publications BV.

Jones, L. E. A. and H. F. Wang, 1981, Ultrasonic velocities in Cretaceous shales from the Williston basin: Geophysics, **46**, 288–297.

Kessinger, W., 1992, Extended split-step fourier migration: 62nd Annual International Meeting, SEG, Expanded Abstracts, **11**, 917–920.

Kiyashchenko, D., R.-E. Plessix, B. Kashtan, and V. Troyan, 2005, Improved amplitude multi-one-way modeling method: Wave Motion, **43**, 99–115.

Lambaré, G., 2008, Stereotomography: Geophysics, **73**, VE25–VE34.

Landrø, M. and L. Amundsen, 2007, Fighting the ghost: Geo ExPro, 78–80.

Larner, K. L. and J. K. Cohen, 1993, Migration error in transversely isotropic media with linear velocity variation in depth: Geophysics, **58**, 1454–1467.

Larner, K. L., L. Hatton, B. S. Gibson, and I.-C. Hsu, 1981, Depth migration of imaged time sections: Geophysics, **46**, 734–750.

Levin, S. A., 1984, Principle of reverse-time migration: Geophysics, **49**, 581–583.

Li, L., 2008, Comment on"Wide-angle phase-slowness approximations in VTI media"(Ø. Pedersen, B. Ursin, and A. Stovas, 2007, Geophysics, 72, no. 4, S177–S185): Geophysics, **73**, X1–X1.

Long, A., 2010, An overview of seismic azimuth for towed streamers: The Leading Edge, **29**, 512–523.

Ma, Y. and G. Margrave, 2008, Seismic depth imaging with the Gabor transform: Geophysics, **73**, S91–S97.

MacLeod, M., R. Hanson, M. Hadley, K. Reynolds, D. Lumley, S. McHugo, and T. Probert, 1999, The Alba field OBC seismic survey: 61st Conference and Technical Exhibition, EAGE, Extended Abstracts.

Musgrave, M. J. P., 1970, Crystal acoustics: Holden-Day, San Fransisco.

Nolte, B., 2005, Converted-wave migration for VTI media using Fourier finite-difference depth extrapolation: 67th Conference and Technical Exhibition, EAGE, Expanded Abstracts.

O'Brien, M. J. and S. H. Gray, 1996, Can we image beneath salt?: The Leading Edge, **15**, 17–22.

Operto, M. S., S. Xu, and G. Lambaré, 2000, Can we quantitatively image complex structures with rays?: Geophysics, **65**, 1223–1238.

Osen, A., L. Storelvmo, L. Amundsen, and A. Reitan, 1996, Decomposition of particle velocity fields into up- and downgoing P- and S-waves: 66th Annual International Meeting, SEG, Expanded Abstracts, 743–746.

Pedersen, Ø., 2008, Reply to the discussion: Geophysics, **73**, X1–X2.

Pedersen, Ø., S. Brandsberg-Dahl, and B. Ursin, 2010, Seismic imaging using lateral adaptive windows: Geophysics, **75**, S73–S79.

Pedersen, Ø., B. Ursin, and A. Stovas, 2007, Wide-angle phase-slowness approximations in VTI media: Geophysics, **72**, S177–S185.

Pierce, A. D., 1981, Acoustics: An introduction to its physical principles and applications: McGraw-Hill.

Pratt, R. G., 1999, Seismic waveform inversion in the frequency domain, part 1: Theory and verification in a physical scale model: Geophysics, **64**, 888–901.

Press, W. H., B. P. Flannery, S. A. Teukolsky, and W. T. Vetterling, 1992, Numerical recipes in fortran, 2nd edition: Cambridge University Press.

Ristow, D. and T. Rühl, 1994, Fourier finite-difference migration: Geophysics, **59**, 1882–1893.

Robertsson, J. O. A. and E. Kragh, 2002, Rough-sea deghosting using a single streamer and a pressure gradient approximation: Geophysics, **67**, 2005–2011.

Rousseau, J. H. L. and M. V. de Hoop, 2001a, Modeling and imaging with the scalar generalized-screen algorithms in isotropic media: Geophysics, **66**, 1551–1568.

———, 2001b, Scalar generalized-screen algorithms in transversely isotropic media with a vertical symmetry axis: Geophysics, **66**, 1538–1550.

Sava, P. and B. Biondi, 2004, Wave-equation migration velocity analysis. i. theory: Geophysical Prospecting, **52**, 593–606.

Sava, P. and S. Fomel, 2003, Angle-domain common-image gathers by wavefield continuation methods: Geophysics, **68**, 1065–1074.

Schneider, W., 1978, Integral formulation for migration in two and three dimensions: Geophysics, **43**, 49–76.

Schoenberg, M. A. and M. V. de Hoop, 2000, Approximate dispersion relations for qP-qSV-waves in transversely isotropic media: Geophysics, **65**, 919–933.

Shan, G. and B. Biondi, 2008, Plane-wave migration in tilted coordinates: Geophysics, **73**, S185–S194.

Shen, P. and W. W. Symes, 2008, Automatic velocity analysis via shot profile migration: Geophysics, **73**, VE49–VE59.

Sheriff, R., 2002, Encyclopedic dictionary of applied geophysics: SEG, Geophysical References Series No. 13.

Sollid, A. and B. Ursin, 2003, Scattering-angle migration of ocean-bottom seismic data in weakly anisotropic media: Geophysics, **68**, 641–655.

Stoffa, P. L., J. T. Fokkema, R. M. de Luna Freire, and W. P. Kessinger, 1990, Split-step Fourier migration: Geophysics, **55**, 410–421.

Stolt, R. H., 1978, Migration by Fourier transform: Geophysics, **43**, 23–48.

Stopin, A., 2000, Comparison of v(θ) equations in TI media. In I. Ikelle and A. Gaugi, (eds.), Anisotropy 2000: Fractures, converted waves, and case studies: SEG, Tulsa.

Stovas, A. and B. Ursin, 2003, Reflection and transmission responses of layered transversely isotropic viscoelastic media: Geophysical Prospecting, **51**, 447–477.

Sun, J. and Y. Zhang, 2008, Practical issues of reverse time migration: true amplitude gathers, noise removal and harmonic-source encoding: 70th Conference and Technical Exhibition, EAGE, Extended Abstracts.

Sun, Y., F. Qin, S. Checkles, and J. P. Leveille, 2000, 3-D prestack Kirchhoff beam migration for depth imaging: Geophysics, **65**, 1592–1603.

Szydlik, T., P. Smith, S. Way, L. Aamodt, and C. Friedrich, 2007, 3D PP/PS prestack depth migration on the Volve field: First Break, **25**, 43–47.

Tenghamn, R., S. Vaage, and C. Borresen, 2008, GeoStreamer, a dual-sensor towed marine streamer: 70th Conference and Technical Exhibition, EAGE, Extended Abstracts.

Thomsen, L., 1986, Weak elastic anisotropy: Geophysics, **51**, 1954–1966.

Thomsen, L. and J. Dellinger, 2003, On shear-wave triplication in transversely isotropic media: Journal of Applied Geophysics, **54**, 289–296.

Tsvankin, I. and L. Thomsen, 1994, Nonhyperbolic reflection moveout in anisotropic media: Geophysics, **59**, 1290–1304.

Tygel, M., B. Ursin, and A. Stovas, 2007, Convergence of traveltime power series for a layered VTI medium: Geophysics, **72**, D21–D28.

Ursin, B., 1983, Review of elastic and electromagnetic wave propagation in horizontally layered media: Geophysics, **48**, 1063–1081.

———, 1984, Seismic migration using the WKB approximation: Geophysical Journal of the Royal Astronomical Society, **79**, 339–352.

———, 1987, The plane-wave reflection and transmission response of a vertically inhomogeneous acoustic medium: In Bernabini, M., Carrion, P., Jacovitti, G., Rocca, F., Treitel, S., and Worthington, M., eds.: Deconvolution and Inversion. Blackwell Sc. Publ., Oxford, 189–207.

Ursin, B. and A. Stovas, 2006, Traveltime approximations for a layered transversely isotropic medium: Geophysics, **71**, D23–D33.

Ursin, B. and M. Tygel, 1997, Reciprocal volume and surface scattering integrals for anisotropic elastic media: Wave Motion, **26**, 31–42.

van Stralen, M. J. N., M. V. de Hoop, and H. Blok, 1998, Generalized Bremmer series with rational approximation for the scattering of waves in inhomogeneous media: The Journal of the Acoustical Society of America, **104**, 1943–1963.

Vestrum, R. W., D. C. Lawton, and R. Schmid, 1999, Imaging structures below dipping TI media: Geophysics, **64**, 1239–1246.

Vivas, F. A., R. C. Pestana, and B. Ursin, 2009, A new stabilized least-squares imaging condition: Journal of Geophysics and Engineering, **6**, 264–268.

Wapenaar, C. P. A. and A. J. Berkhout, 1989, Elastic wave field extrapolation: Redatuming of single- and multi-component seismic data: Elsevier.

Wapenaar, K., 1998, Reciprocity properties of one-way propagators: Geophysics, **63**, 1795–1798.

Ward, S. H., 1980, Electrical, electromagnetic, and magnetotelluric methods: Geophysics, **45**, 1659–1666.

Whitmore, N. D., 1983, Iterative depth migration by backward time propagation: 53rd Annual International Meeting, SEG, Expanded Abstracts, 382–385.

Whitmore, N. D., S. H. Gray, and A. Gersztenkorn, 1987, A survey of depth migration methods: 57th Annual International Meeting, SEG, Expanded Abstracts, 365–365.

Wu, R., Y. Wang, and J. Gao, 2000, Beamlet migration based on local perturbation theory: 70th Annual International Meeting, SEG, Expanded Abstracts, 1008–1011.

Wu, R.-S. and L.-J. Huang, 1992, Scattered field calculation in heterogeneous media using a phase-screen propagator: 62nd Annual International Meeting, SEG, Expanded Abstracts, 1289–1292.

Wu, R.-S. and S. Jin, 1997, Windowed GSP (generalized screen propagators) migration applied to SEG-EAEG salt model data: 67th Annual International Meeting, SEG, Expanded Abstracts, 1746–1749.

Xie, X.-B. and R.-S. Wu, 2005, Multicomponent prestack depth migration using the elastic screen method: Geophysics, **70**, S30–S37.

Zhang, J., W. Wang, and Z. Yao, 2009, Comparison between the Fourier finite-difference method and the generalized-screen method: Geophysical Prospecting, **57**, 355–365.

Zhang, Y., S. Xu, N. Bleistein, and G. Zhang, 2007, True-amplitude, angle-domain, common-image gathers from one-way wave-equation migrations: Geophysics, **72**, S49–S58.

Zhang, Y., G. Zhang, and N. Bleistein, 2003, True amplitude wave equation migration arising from true amplitude one-way wave equations: Inverse Problems, **19**, 1113–1138.

———, 2005, Theory of true-amplitude one-way wave-equations and true-amplitude common-shot migration: Geophysics, **72**, E1–10.

Appendix A

Improved wide-angle phase-slowness approximations

In this appendix a discussion of implementation aspects of the direct approximations of the squared phase-slowness which was developed in chapter 2 (Pedersen, 2008) is provided. In Li (2008), an approach for improving the accuracy some of our wide-angle phase-slowness approximations is suggested. A description of this method and a description on how it can be used follows. Finally, an example is included.

A.1 Improved approximations

Li suggests utilizing both the exact slowness expression q^2_{exact} and the approximated slowness expression q^2_{approx} for each combination of anisotropy parameters to pre-calculate a scale coefficient k, which in turn is used to improve the slowness approximation. His approach is based upon creating a lookup-table depending on all the parameters involved in the exact expression, that is, ε, δ, β_0 and α_0. Li illustrates that this method may have a potential for increased accuracy of the approximation at the cost of creating and accessing a lookup-table.

If all anisotropy parameters are known, one could pre-calculate the exact slowness expression for each wave-mode qP and qSV and store it in a table depending on $\varepsilon, \delta, \alpha_0$ and β_0. This would produce an excessively large table, and is not a very practical approach. By providing a direct approximation q^2_{approx}, e.g. our equation 2.24, this expression can be used as an initial estimate in an optimization procedure to produce a new expression which is closer in some sense to q^2_{exact}. Rewriting our equation 2.24 truncated at b_2 by introducing Li's scaling coefficient

k yields

$$q_\alpha^2 = \frac{1}{\alpha_0^2}\left(1 - \left(\frac{\alpha_h}{\alpha_0}\right)^2 (p\alpha_0)^2\right) \times \left(1 - b_0\,(p\alpha_0)^2 - b_1\,(p\alpha_0)^4 - k(\varepsilon,\delta,\alpha_0,\beta_0)b_2\,(p\alpha_0)^6\right), \tag{A-1}$$

where

$$k(\varepsilon,\delta,\alpha_0,\beta_0) \equiv 1 \tag{A-2}$$

for a truncated Taylor series. By e.g. minimizing

$$\max|\Delta q_\alpha| \tag{A-3}$$

over k as suggested by Li, one produces an updated lookup table $k(\varepsilon,\delta,\alpha_0,\beta_0)$. This would obviously improve the truncated wide-angle Taylor approximation in the sense of the criterion used to update k, as illustrated in Li's example.

The method suggested by Li is not applicable for our simplified expressions where not all medium parameters need to be known. For qP wave slowness, the approximation in our equation 2.19 does not involve β_0. For qSV wave slowness, the approximation in equation 2.23 only involves two parameters. However, for $qP - qSV$ converted waves, we need all four anisotropy parameters in our approximations. To construct Li's improved approximations one need two tables, k_α and k_β, one for each wave-mode.

A.2 Numerical example

As an example we use the medium given in Table A.1. In Figure A.1 we show a comparison of the difference between the exact and the approximated qP slowness curves. The maximum error of the original approximation is 0.011 ms/m. We regard a qP-wave with maximum frequency $f = 60$ Hz propagating a distance of 2000 m in Model 1. If one require that $\Delta q < 1/(8\,f\Delta z)$, this gives a maximum error of 10^{-3} ms/m. Thus, the approximation in equation A-1 with $k = 1$ introduce an error of 1.10^{-3}, and cannot be used without too large errors induced by the approximation.

By applying the method of Li, one find $k = 0.536$, and $\max|\Delta q| = 8.1 \times 10^{-4}$, which is below the prescribed acceptable error Δq induced by the slowness approximation.

Parameters	α_0[km/s]	β_0[km/s]	ε	δ	σ
Model 1	2.0	1.0	0.10	-0.10	-0.08

Table A.1: The parameters of the model used for computation of phase-slowness approximations.

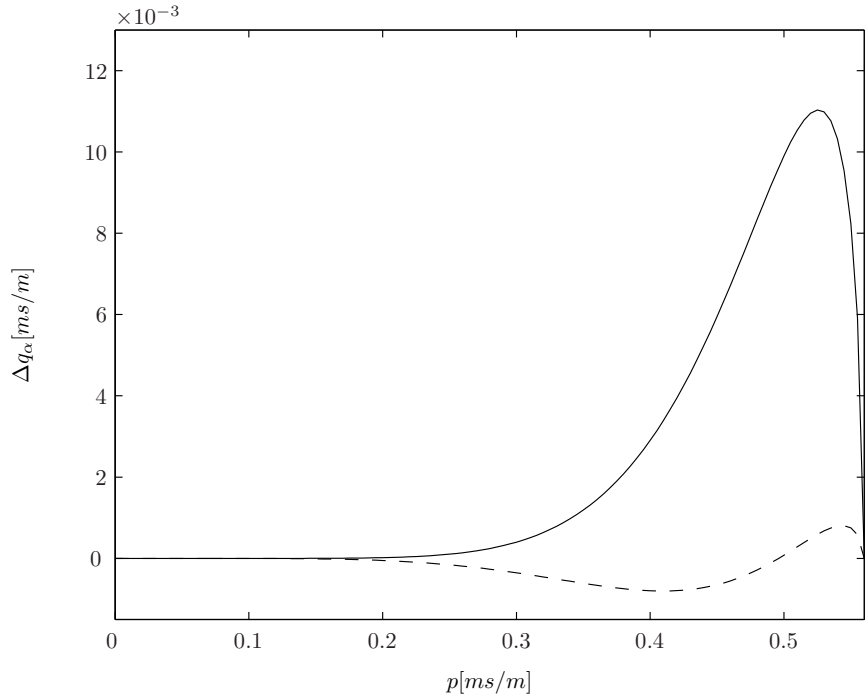

Figure A.1: Comparison of the difference Δq_α between the exact qP and approximated qP slowness curves: the wide-angle Taylor approximation with solid line and the improved wide-angle Taylor approximation with dashed line.